Program:

FP7-ICT-FET-OPEN

Project:

Blue Femtosecond Laser Implemented with Group-III Nitrides

FEMTOBLUE

Contract:

EC Contract
INFSO-ICT-238556 FEMTOBLUE

Title:

Deliverable D7.3
Phase 2 Scientific Report

Issue 1/ 28.10.2011

Dissemination Level:

PU (Public)

	Name	Date	Signature
Preparation	Dmitri L. Boiko, (CSEM) Arno Hoogerwerf (CSEM) Sylvain Grossmann (CSEM) Jörg Pierer (CSEM) Thomas Stadelmann (CSEM) Xi Zeng (CSEM) Nicolas Grandjean, (EPFL) Julien Dorsaz, (EPFL) Luca Sulmoni (EPFL) Ulrich Schwarz (FRAUNHOFER) Wolfgang Scheibenzuber (FRAUNHOFER) Adrian Wonfor (UCAM) Vojtech Olle (UCAM) Peter Vasil'ev (LPI) Igor Smetanin (LPI) Michael Kneissl (TUB) Simon Ploch (TUB) Martin Frentrup (TUB) Tim Wernicke (TUB)	28.10.11	

Verification	Dmitri L. Boiko	28.10.11	
Approval	Dmitri L. Boiko	28.10.11	

Distribution list

University/Research Institute	Name	Nr copies
EC INFSO-ICT	Commission of the European Communities Information Society and Media Directorate-General	
CSEM	D. L. Boiko, A. Hoogerwerf, C. Bosshard	
EPFL	N. Grandjean	
FRAUNHOFER	U. Schwarz	
UCAM	I. H. White, R. Penty	
LPI	P. Vasil'ev	
TUB	M. Kneissl	

TABLE OF CONTENT

1. General

1.1 Scope

This document is written in the framework of the project Blue Femtosecond Laser Implemented with Group-III Nitrides (FEMTOBLUE) supported by the EC Grant INFSO-ICT-238556.

This document is the contractual derivable D7.3 (report) as per Annexe II (DoW) of the Grant Agreement [AD-1]:

"**Deliverable D7.3 – Phase 2 Scientific Report** "

The dissemination level of the report D7.3 is public (PU).

This document has the **Confidential Annexe** [RD-13], submitted as a separate document, as per MoMs of the Project Negotiation Meeting [AD-2].

This document reports the achievement and scientific results obtained by FEMTOBLUE consortium during the second period 01.09.2010-31.08.2011.

More specifically, this document reports on

1. Growth of blue and violet wavelength SCH QWs (WP1)
2. Optical characterization of heterostructures (WP2)
3. Final design of GaN-based ultrafast MS-LDs, modelling of gain and absorption in InGaN/GaN QWs and dynamics of MS-LD(WP3)
4. Fabrication of multisection InGaN/GaN lasers (WP4)
5. Dynamical tests of preliminary multisection InGaN/GaN lasers (WP5)
6. Dissemination and use (WP6)

1.2 Documentation

1.2.1 Applicable Documents

ID	Title	Reference	Issue/Date
[AD-1]	Grant Agreement 238556 „Blue Femtosecond Laser Implemented with Group-III Nitrides"	Grant Agreement 238556 FEMTOBLUE	02.07.2009
[AD-2]	Minutes of negotiation meeting of 09/04/2009 in Brussels	File MoMs_NegMeeting_090429.pdf	03.05.2009

1.2.2 References documents

ID	Title	Reference	Issue/Date
[RD-1]	Milestone confirmation "Milestone M1.1: Preliminary violet wavelength heterostructures are grown"	File FEMTOBLUE_GA238556_-M1.1_Issue1_100329_Violet_ Laser_Diode_Heterostructure.pdf	29.03.2010
[RD-2]	Milestone confirmation "Milestone M1.2: Preliminary blue wavelength heterostructures are grown"	File FEMTOBLUE(GA238556)-M1.2_Issue1_100329_Bue_Laser_ Diode_Heterostructure.pdf	29.03.2010
[RD-3]	Test plan and procedures for optical characterization of heterostructures and gain measurements	Deliverable D2.1	18.12.2009
[RD-4]	Final report on heterostructure growth and optical gain characterisation	Draft 1 of deliverable D1.1 Confidential	10.09.2010
[RD-5]	Phase 1 Scientific Report	Deliverable D7.1	27.10.2010
[RD-5-CA]	Confidential Annexe to Phase 1 Scientific Report	Confidential annexe to deliverable D7.1	27.10.2010
[RD-6]	Phase 1 Periodic Report	Deliverable D7.2	Issue 2 21.01.2011
[RD-7]	Milestone M3.1 report	Deliverable D3.1	29.10.2010
[RD-8]	Test plan and procedures for multisection fs GaN lasers	Deliverable D5.1	15.12.2010
[RD-9]	Milestone M4.1 report	Deliverable D4.1	20.04.2011
[RD-10]	Milestone M2.2. report	Deliverable D2.2	13.10.2011
[RD-11]	Final report on heterostructure growth and optical gain characterisation	Draft 2 of deliverable D1.1 Confidential	13.10.2011
[RD-12]	Final report on multisection laser structures	Draft 1 of deliverable D5.2 Confidential	26.09.2011
[RD-13]	Confidential Annexe to Phase 2 Scientific Report	Confidential annexe to deliverable D7.3	28.10.11
[Meyer-07]	Der Einfluss der optischen Verstärkung auf das zeitliche und spektrale Verhalten von InGaN-Laserdioden	Tobias Meyer, Diploma Thesis, Regensburg (2007)	2007
[Andreev-93]-4	Cooperative Effects in Optics: Superradiance and Phase Transitions	Andreev A V, Yemel'yanov V I and Il'inskii Yu A (Bristol: Institute of Physics Publishing,1993)	1993
[Bastard-91]	Wave mechanics applied to heterostructures	G. Bastard (Wiley-Interscience, 1991)	1991

[Boiko-08]	Towards r-space Bose-Einstein condensation of photonic crystal exciton polaritons	D. L. Boiko, PIERS online **4**, 831-837 (2008)	2008
[Boiko-11]	Femtosecond superradiance in multiple-section InGaN/GaN quantum well laser structures	D. L. Boiko, P. P. Vasil'ev, Preprint arXiv:1103:5507	2011
[Braun-09]	Multidimensionale Charakterisierung der Modendynamik von (Al,In)GaN Laserioden	H. Braun, PhD Thesis (University of Regensburg, 2009)	2009
[Braun-09a]	Impact of filamentation on the far-field of high power broad ridge (Al,In)GaN laser diodes	H. Braun, S. Rogowsky, U.T. Schwarz, S. Brünninghoff, A. Lell and U. Strauß, proc. SPIE 7230, 72300F (2009)	2009
[Chemla-85]	Two-dimensional semiconductors: recent development	D.S. Chemla, J. Luminescence **30**, 502 (1985)	1985
[Chow-98]	Semiconductor-Laser Fundamentals	W.W. Chow and S.W. Koch, (Springer, Berlin, 1998).	1998
[Chow-99]	Quantum-well width dependence of threshold current density in InGaN lasers	W.W. Chow, H. Amano, T. Takeuchi, and J. Han, Appl. Phys. Lett. **75**, 224 (1999).	1999
[Christopoulos-07]	Room-Temperature Polariton Lasing in Semiconductor Microcavities	S. Christopoulos, G. Baldassarri Höger von Högersthal, A. J. D. Grundy, P. G. Lagoudakis, A.V. Kavokin, J. J. Baumberg, G. Christmann, R. Butté, E. Feltin, J.-F. Carlin, and N. Grandjean, , Phys. Rev. Lett. **98**, 126405 (2007).	2007
[Dicke-54]	Coherence in Spontaneous Radiation Processes	R. H. Dicke, *Phys. Rev.* **93** 99 (1954)	1954
[Dixon-79]	Generalized expressions for the turn-on delay in semiconductor lasers	R.W.Dixon and W.B.Joyce, J.Applied Physics, **50** (7), 4591 (1979)	1979
[Gourley-89]	Lasing threshold in quantum well Surface emitting lasers: Many body effects and temperature dependence,	P. L. Gourley, S. K. Lyo, T. M. Brennan, and So E. Hammons, C. F. Schaus and S. Sun, Appl. Phys. Lett. 55, 2698 (1989).	1989
[Gross-82]		Gross M and Haroche S *Phys. Rep.* **93** 301 (1982)	1982
[Hakki-75]	Gain spectra in GaAs double-heterostructure injection lasers	B. Hakki and T. Paoli, J. Appl. Phys. 46, 1299 (1975).	1975
[Hönninger99]	Q-switching stability limits of continuous-wave passive mode locking	C. Hönninger, R. Paschotta, F. Morier-Genoud, M. Moser, and U. Keller, JOSA B 16, 46-56 (1999)	1999

[Kyhm-01]	Analysis of gain saturation in $In_{0:02}Ga_{0:98}N/In_{0:16}Ga_{0:84}N$ multiple quantum wells	K. Kyhm, R. Taylor, J. Ryan, T. Someya and Y. Arakawa, Appl. Phys. Lett. 79, 3434 (2001).	2001
[Koumans-96]		R.G.M.P. Koumans, R. van Roijen, IEEE J. QE**. 32**, 478 (1996)	1996
[Leegwater-96]		J. Leegwater IEEE J. QE**. 32**, 1782 (1996)	1996
[Men'shikov-99]-6		L .I. Men'shikov, *Phys. Usp.* **42** 107 (1999)	1999
[Meyer-08]	Spectral dynamics of 405 nm (Al,In)GaN laser diodes grown on GaN and SiC substrate	T. Meyer, H. Braun, U.T. Schwarz, S. Tautz, M. Schillgalies, S. Lutgen, and U. Strauß, Optics Express **16**, 6833 (2008)	2008
[Miy-09]	Picosecond optical pulse generation from self-pulsating bisectional GaN-based blue-violet laser diodes	T. Miyajima, H. Watanabe, M. Ikeda, and H. Yokoyama, Applied Physics Letters 94, 161103 (2009)	2009
[MIY11]	Saturable absorbing dynamics of GaInN multiquantum well structures	T. Miyajima, S. Kono, H. Watanabe, T. Oki, R. Koda, M. Kuramoto, M. Ikeda, and H. Yokoyama, Applied Physics Letters, vol. 98, pp. 1719041 - 1719043, 2011.	2011
[Mir-99]	Selfpulsating semiconductor lasers: theory and experiment	C. Mirasso, G. Van Tartwijk, E. Hernandez-Garcia, D. Lenstra, S. Lynch, P. Landais, P. Phelan, J. O'Gorman, M. San Miguel, and W. Elsasser, IEEE Journal of Quantum Electronics 35(5), 764 - 770 (1999).	1999
[Nak-97]	InGaN/GaN/AlGaN-based laser diodes with modulation-doped strained-layer superlattices	S. Nakamura, M. Senoh, S.-I. Nagahama, N. Iwasa, T. Yamada, T. Matsushita, H. Kiyoku, Y. Sugimoto, T. Kozaki, H. Umemoto, M. Sano, and K. Chocho, Japanese Journal of Applied Physics 36(12A), 1568-1571 (1997).	1997
[Piprek-03]	Semiconductor optoelctronic devices: Introduction to physics and simulation	J. Piprek (Academic Press, London, 2003)	2003
[Piprek-07]	Nitride semiconductor devices: principles and simulations	ed. J. Piprek, (Wiley VCH, New York, 2007).	2007
[Renner-02]	Quantitative analysis of the polarization fields and absorption changes in InGaN/GaN quantum wells with electroabsorption spectroscopy	F. Renner, P. Kiesel, G. Döhler, M. Kneissl, C. G. Van de Walle and N. M. Johnson, Appl. Phys. Lett. 81, 490 (2002)	2002
[Scheibenzuber-09]	Optical Gain in (Al,In)GaN Laser Diodes	Wolfgang Scheibenzuber, Diplom Thesis, Regensburg (2009)	2009

[Scholz-08]	Measurement and simulation of filamentation in 405 nm (Al,In)GaN laser diodes	D. Scholz, H. Braun, U.T. Schwarz, D. Queren, S. Brüninghoff, A. Lell, and U. Strauß, Optics Express 16, 6846 (2008)	2008
[Scheibenzuber-09a]	Calculation of optical eigenmodes and gain in semipolar and nonpolar InGaN/GaN laser diodes	W. G. Scheibenzuber, U. T. Schwarz, R. G. Veprek, B. Witzigmann, and A. Hangleiter, Phys. Rev. B 80, 115320 (2009)	2009
[Scheibenzuber-10]	Antiguiding factor of GaN-based laser diodes from UV to green	W. G. Scheibenzuber, U. T. Schwarz, T. Lermer, S. Lutgen, and U. Strauss	2010
[Scheibenzuber-10a]	Bias-dependent Absorption Coeffcient of the Absorber Section in GaN-based Multi-Section Laser Diodes	W. G. Scheibenzuber, U. T. Schwarz, L. Sulmoni, and N. Grandjean, Appl. Phys. Lett., submitted	2010
[Scheibenzuber-10b]	Measurement of the tuneable absorption in GaN-based multi-section laser diodes	W. G. Scheibenzuber, U. T. Schwarz, L. Sulmoni, J.-F. Carlin, A. Castiglia, and N. Grandjean, phys. Status solidi, submitted	2010
[Scheibenzuber-11]	Recombination coefficients of GaN-based laser diodes	W. G. Scheibenzuber, U. T. Schwarz, L. Sulmoni, J. Dorsaz, J.-F. Carlin, and N. Grandjean, J. Appl. Phys. **109**, 093106 (2011)	2011
[Scheibenzuber-11]	GaN-based laser diodes: towards longer wavelengths and short pulses	W. G. Scheibenzuber, PhD thesis, Springer, ISBN 978-3-642-24537-4	2011
[Schwarz-03]	Optical gain, carrier-induced phase shift, and linewidth enhancement factor in InGaN quantum well lasers	U. Schwarz, E. Sturm, W. Wegscheider, V. Kümmler, A. Lell and V. Härle, Appl. Phys. Lett. 83, 4095 (2003)	2003
[Schuurmans-81]		M. F. H. Schuurmans, Q. H. F. Vrehen and Polder D *Adv. At.Mol. Phys.* **17** 167 (1981)	1981
[Sergent-98]	Thermal management handbook for Electronic Assemblies	Jerry E. Sergent, Al Krum (McGraw-Hill, 1998)	1998
[Skribanowitz-73]		N. Skribanowitz, I. P. Herman, J. C. MacGillivray and M. S. Feld, *Phys. Rev. Lett.* **30** 309 (1973)	1973
[Tan-98]	Frequency control of self-sustained pulsating laser diodes by uniform impurity doping into multiple-quantum-well structures	T. Tanaka and T. Kajimura, IEEE Photonics Technology Letters 10(1), 48-50 (1998).	1998
[Vasil'ev-95]	Ultrafast Diode lasers : Fundamentals and Applications	P.Vasil'ev (Artech House, Norwood, 1995)	1995
[Vasil'ev-99]		Vasil'ev P P *Quantum Electron.* **29** 842 (1999)	1999

[Vasil'ev-01]	Experimental evidence of condensation of electron-hole pairs at room temperature during femtosecond cooperative emission	P.P. Vasil'ev, H. Kan, H. Ohta and T. Hiruma, Phys. Rev. B **64**, 195209 (2001).	2001
[Vasil'ev-04]		Vasil'ev P P *Phys. Status Solidi* B **241** 1251 (2004)	2004
[Vasil'ev-09]	Femtosecond superradiant emission in inorganic semiconductors	P.P.Vasil'ev *Rep. Prog. Phys.* **72** 076501 (2009)	2009
[Vurgaftman-07]	Nitride semiconductor devices: principles and simulations	I. Vurgaftman and J. R. Meyer, J. Piprek, Ed. (Wiley VCH, New York, 2007).	2007
[Wat-10]	10-W peak-power picosecond optical pulse generation from a triple section blue-violet self-pulsating laser diode	H. Watanabe, T. Miyajima, M. Kuramoto, M. Ikeda, and H. Yokoyama, Applied Physics Express 3(5), 052701(2010)	2011

1.2.3 List of acronyms

Accr.	Description
AD	Applicable Document
AR	Anti-reflection
COD	Catastrophic Optical Damage
CSEM	Centre Suisse d'Electronique et de Microtechnique
DFB	Distributed Feedback
DSR	Dicke superradiance
EL	Electroluminescence
EPFL	Ecole Polytechnique Fédérale de Lausanne
FRAUNHOFER	Fraunhofer Institute for Applied Solid State Physics
GVD	Group velocity dispersion
IAF	Fraunhofer Institute for Applied Solid State Physics
LBIC	Laser beam induced current
LD	Laser Diode
LPI	P.N. Lebedev Physical Institute
µEL	Micro-electroluminescence
MLD	Multisection Laser Diode
MoMs	Minutes of the meeting
MS-LD	Multisection Laser diodes
µPL	Micro- photoluminescence
N.A.	Numerical aperture
PL	Photoluminescence
QCSE	Quantum confined Stark effect
QW	Quantum well
RD	Reference document
SCH	Separate confinement heterostructure
SHG	Second harmonic generation
SPAD	Single photon avalanche detector
SR	Superradiance
TBC	To be confirmed
TBD	To be defined
TCSPC	Time correlated single photon counting
TE	Transverse electric
TM	Transverse magnetic
TUB	Technische Universität Berlin
UCAM	University of Cambridge
WP	Work package
FWHM	Full width at half maximum
BEC	Bose-Einstein condensation

BCS	Bardeen, Cooper, and Schrieffer

2. Heterostructure Growth (WP1)

Violet and blue lasers have been demonstrated (by members of the consortium amongst others) and industrialized. Lasers capable of continuous-wave (cw) operation, as demonstrated by the consortium partners EPFL and TUB, are the starting point for the development of short pulse lasers. Within the work package not only the delivery of cw laser wafers but also the incorporation and testing of design proposals by the consortium partners into the heterostructure are intended as well as a gradual improvement of all device parameters. The consortium partner EPFL is responsible for growth of violet emitting lasers (Milestones M1.1, M1.3). The consortium partner TUB is responsible for growth of blue emitting lasers (Milestones M1.2, M1.4).

The tasks WP1.2 Trade off Analysis of laser heterostructure composition and growth for violet and blue wavelength range have been finished by the project consortium yielding definition for preliminary composition for separate confinement heterostructures to be used in multisection laser structures capable of producing ultrafast optical pulses. There were no systematic data available in the literature on the use of GaN QW heterostructure as a tunable absorber in the laser cavity. Therefore, a heterostructure design optimized for the optical gain and confinement was chosen as a baseline. The laser structures grown with this preliminary composition for separate confinement heterostructures were then used to measure the properties of the absorber section and multisection laser devices. Thus the milestones M1.1 and M1.2, i.e. growth of 2 inch epiwafers with low In content for operation in the 400-425 nm wavelength range and with high In content for operation in the 425-450 nm wavelength range, respectively, have been accomplished by the consortium partners in month 7 of the project [RD-1, RD-2].

For the second period of the project, a dedicated growth plan has been established [RD-6]. Based on the results of the first blue and violet heterostructures obtained in the first period, optimized structures were grown and characterized. A structure with an active region containing a double QW with 4.5 nm wide wells is described in section 2.1 Growth of violet wavelength SCH LDs. This laser design resulted in threshold currents as low as 40 mA for a 800 x 2 µm² LD at a high slope efficiency of 0.6 W/A.

For the growth of blue wavelength SCH laser diodes p-doping was identified as critical issue. The high growth temperatures during epitaxy of the p-cladding degraded the blue light emitting InGaN QWs. The epitaxial growth conditions had to be adapted to reduce the degradation of the active region while still resulting in a high conductivity of the p-side epitaxial layers. Several test structures were grown to solve the problem of p-doping and find an optimized structure. This was first tested for a violet LD, as described in section 2.2. These laser diodes were also processed as ridge waveguide LDs. Gain spectra (see section 3.3.2) demonstrate low internal losses and high injection efficiency for this SCH laser structure.

The lasers grown in the second period of the project were analyzed in work package WP2.3 on gain uniformity assessment, optical gain measurements (See section 3 of this document) as well as WP5 on test and evaluation of multisection laser structures (section 6 of this document) delivering feedback for the heterostructure design as described in the conclusion (section 2.3).

2.1 Growth of violet wavelength SCH QWs

In the first period of the project, a first laser epistructure was grown on a free-standing GaN substrate (Fig.2.1). It contains 2 InGaN quantum wells (QWs) in the active region and the claddings (p- and n- types) consist in AlGaN alloy with about 8% Al composition (nominal) and 500 nm nominal thickness. The QW thickness and composition were 3.5 nm and 12 %, respectively. The epiwafer was uncracked. The growth was performed following the preliminary design. Successful growth of violet wavelength SCH QWs was confirmed with milestone M1.1 [RD-1].

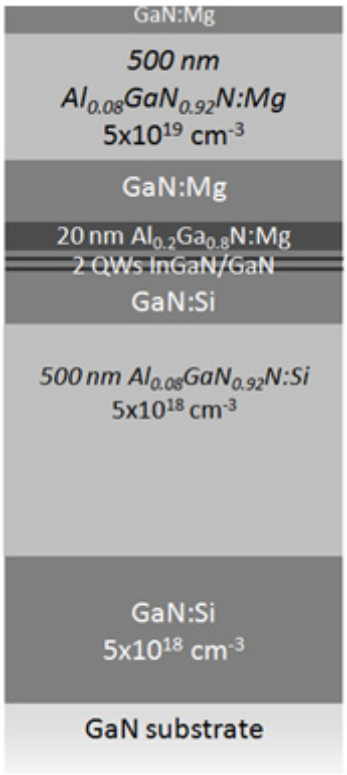

GaN:Mg	10 nm
AlGaN :Mg	500 nm
GaN :Mg + AlGaN :Mg	150 nm
2x InGaN/InGaN QW	3 nm (13-15%)/ 12 nm (3-5%)
GaN :Si	150 nm
AlGaN :Si	800 nm
GaN :Si	2 µm
GaN substrate	300-350 µm

Fig. 2.1. Description of the layered structure of the A1902 wafer grown sheet

In the second period of the project, an optimized laser epistructure was grown on a free-standing GaN substrate (Fig 2.2). As the previous growth, it contains 2 InGaN QWs in the active region and the claddings (p- and n- types) consist in AlGaN alloy with about 8% Al composition (nominal) and 500 nm nominal thickness. The QW thickness and composition were 4.5 nm and 12 %, respectively. The epiwafer was uncracked.

Below we summarize preliminary results regarding I-P and I-V curves obtained with this sample.

Laser bars were then processed from this epiwafer with the same multi-section mask of the previous process. Laser action under cw at room-temperature was obtained on different structures with various length (from 600 microns to 1.5 mm) and ridge width (from 2 microns to 10 microns).

Typical *L-I-V* curves of a MS-LD for different V_{SA} are shown in Fig. 6.

GaN:Mg	20 nm
AlGaN :Mg	500 nm
GaN :Mg + AlGaN :Mg	150 nm
2x InGaN/InGaN QW	4.5 nm (12%)/ 12 nm (1%)
GaN :Si	100 nm
AlGaN :Si	1 µm
GaN :Si	2 µm
GaN substrate	300-350 µm

Fig. 2.2. Description of the layered structure of the wafer grown sheet

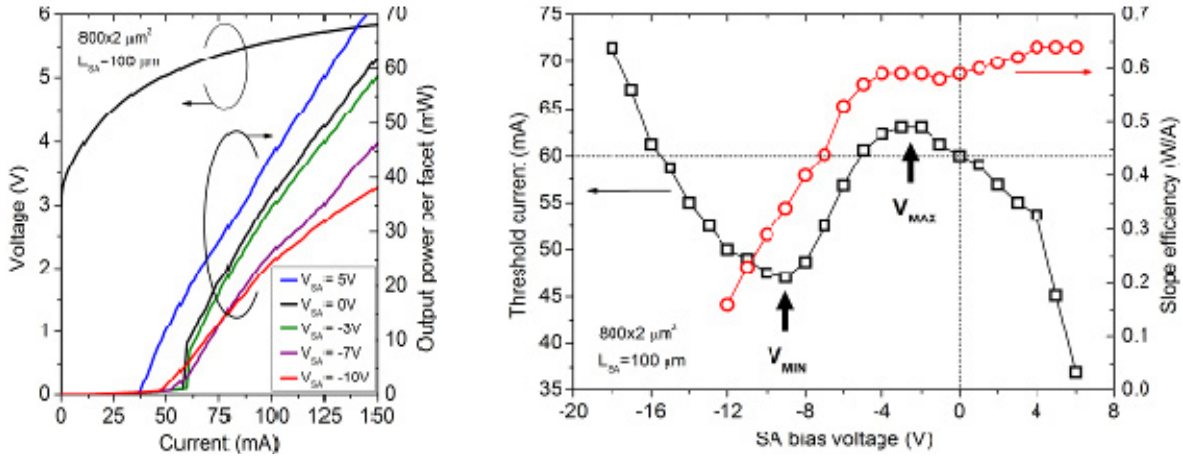

Fig. 2.3. (a) *L-I-V* curves of a MS-LD for different V_{SA} (b) Threshold current and slope efficiency as a function of the applied bias to the SA.

The operating voltage is around 5-6 V drop at 100 mA and the best values for threshold current (I_{th}) and slope efficiency per facet are 40 mA and 0.6 W/A, respectively, for a 800 x 2 µm^2 single-section standard device. A drastic influence of V_{SA} on the *L-I* characteristics has been noticed on the multi-section devices (Fig.2.3a). When the SA is first forward-biased, I_{th}

decreases from 60 mA down to 37 mA since the device starts to act as a single-section LD. Conversely, for a reverse-biased SA, an increase of I_{th} is first observed reaching a maximum for a bias voltage around -2.5 V (called V_{MAX}). A further increase in the SA reverse bias voltage causes I_{th} to decrease and a minimum I_{th} is obtained for V_{SA}=-9 V (called V_{MIN}). For very large negative bias voltages, I_{th} starts to increase again. Consequently, when applying a fixed current to the GS (for example 60 mA), it is possible to turn on and off the lasing regime by simply changing V_{SA} (Fig. 2.3b).

2.2 Growth of blue wavelength SCH QWs

Growth of blue InGaN MQW laser diodes was optimised in several steps accompanied by characterisation and device modelling. First the separate confinement heterostructure (waveguide, cladding, active region) was optimised by simulation and growth of optically pumped lasers, followed by the optimisation of the MQW active region. Finally current-injection laser diodes were grown and BA lasers were fabricated and tested.

In the second period of the project, analysis of such laser diodes revealed that the GaN:Mg overgrowth temperature was too high for blue $In_{0.2}Ga_{0.8}N$ quantum wells, which degraded during p-layer overgrowth. Subsequently growth parameters were optimized for lower overgrowth temperatures by varying precursor flows, pressure, and V/III-ratio. Quantum wells overgrown with improved (Al)GaN:Mg overgrowth process showed no degradation of the luminescence properties. In order to compare and test the improved growth parameters with the previous results, 405 nm laser diodes were grown and BA lasers fabricated. The devices yielded laser threshold of 3.9 kA/cm² and a DQE of 0.3 W/A per facet.

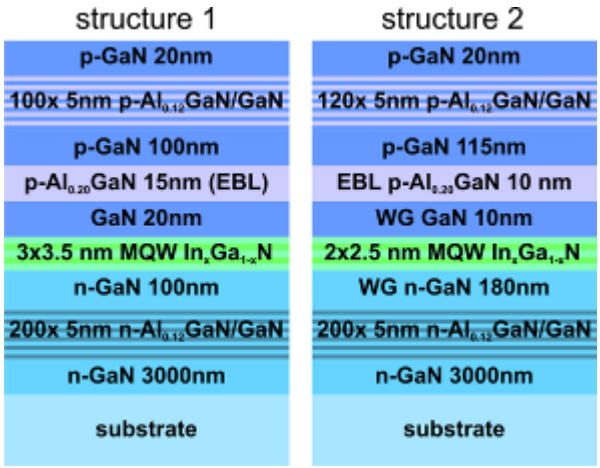

Fig. 2.4. Violet and blue laser heterostructures that are compared within the report.

The initial (structure 1) and the optimized (structure 2) laser heterostructures are depicted in Fig. 2.4. In this iteration the cladding layer thickness, the waveguide thickness, and the active region were optimised for low threshold laser operation.

In comparison to violet laser diodes, blue laser diodes suffer from a reduced refractive index contrast at the GaN/AlGaN interfaces resulting in a reduced confinement factor and reduced modal gain. This causes increased lasing thresholds and the occurrence of substrate modes.

Therefore the confinement factor and modal gain were modelled for different 450 nm separate confinement heterostructures (Fig. 2.5a). Hereby waveguide and cladding thickness and composition were varied. Best results were achieved for 200 nm $In_{0.02}Ga_{0.98}N$ waveguides with $Al_{0.1}Ga_{0.9}N$ claddings >0.4 µm thickness, whereas slight reduction in the modal gain was observed for lower cladding Al contents. 200 nm thick GaN waveguides yielded also good results but require a much larger AlGaN cladding thickness of >0.7 µm. The 100 nm GaN waveguide from the initial structure definition shows reduced modal gain even for very large cladding thickness of >1.2 µm. The predictions of the simulations were verified by investigation of the threshold power densities and far-field pattern measurements of optically pumped lasers. Lasers with InGaN waveguides had very high lasing thresholds most probably due to problems with the surface morphology of the InGaN layers. As shown in Fig. 2.5b, the lasing threshold decreases from 900 to 200 kW/cm² with increasing waveguide thickness. This complies well with an increase of the optical confinement and the modal gain.

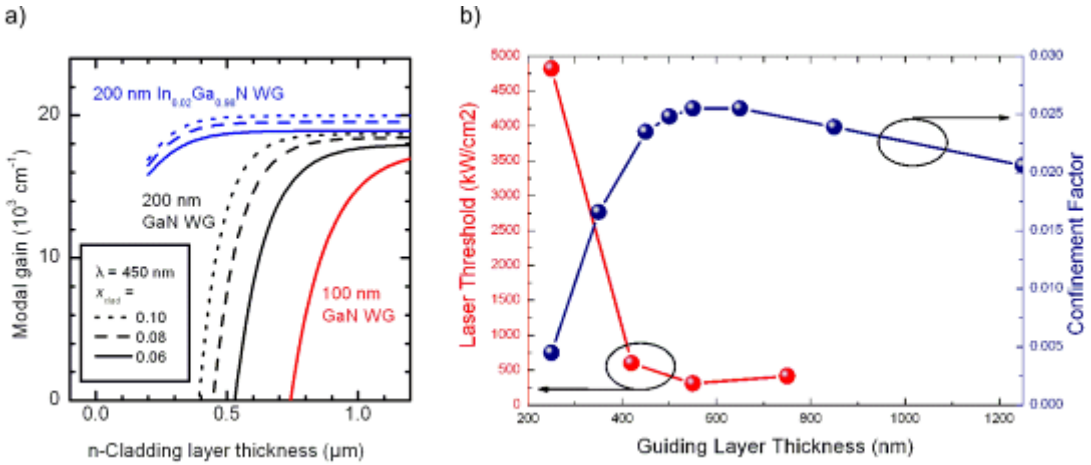

Fig. 2.5. a) Simulation of the modal gain in 450 nm SCH laser heterostructures. b) Comparison of calculated confinement factor and threshold measurements for 450 nm lasers

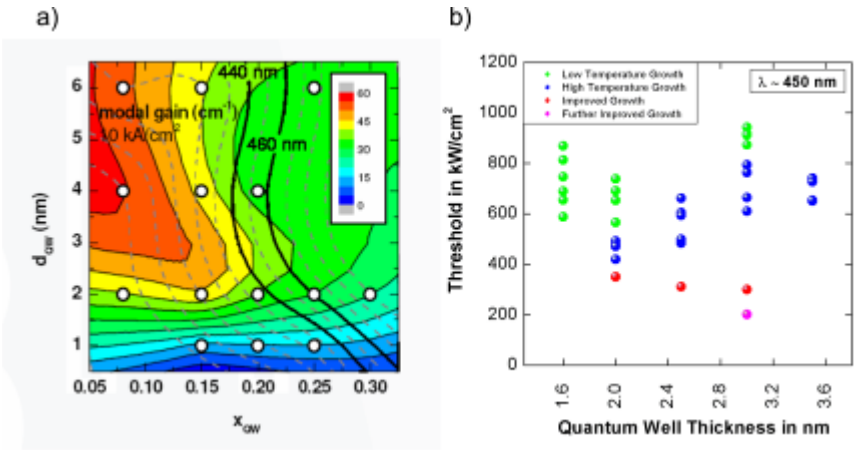

Fig. 2.6. a) Modal gain of optically pumped laser structures with different quantum well widths and indium contents. Regions of one wavelength follow the solid line. b) Threshold power densities of optically pumped laser structures with different quantum well widths emitting around 450 nm.

In order to optimise the MQW active region device modelling was used to find improved design parameters. Simulation results based on Schrödinger-Poisson and drift-diffusion model revealed that only two quantum wells are efficiently pumped by the injected carriers. Therefore further research was conducted with DQW structures. Also the effect of active region design on the optical confinement was taken into account, as shown in Fig. 2.6a. Here the optical confinement and lasing wavelength are plotted vs. the quantum well width and indium content of the quantum well. With increasing width at constant In-content, the wavelength decreases due to smaller quantum confinement. For increasing indium content also the wavelength decreases due to a smaller band gap of the gain material. The band for blue emission is highlighted by bold lines. Within this band a local maximum of the modal gain can be found for QW width ranging from 2 nm to 4 nm. This guideline was used for growth of quantum well structures as tested in optically pumped laser diodes. Here the lowest lasing threshold of 200 kW/cm² was achieved in this region with a well width of 3 nm.

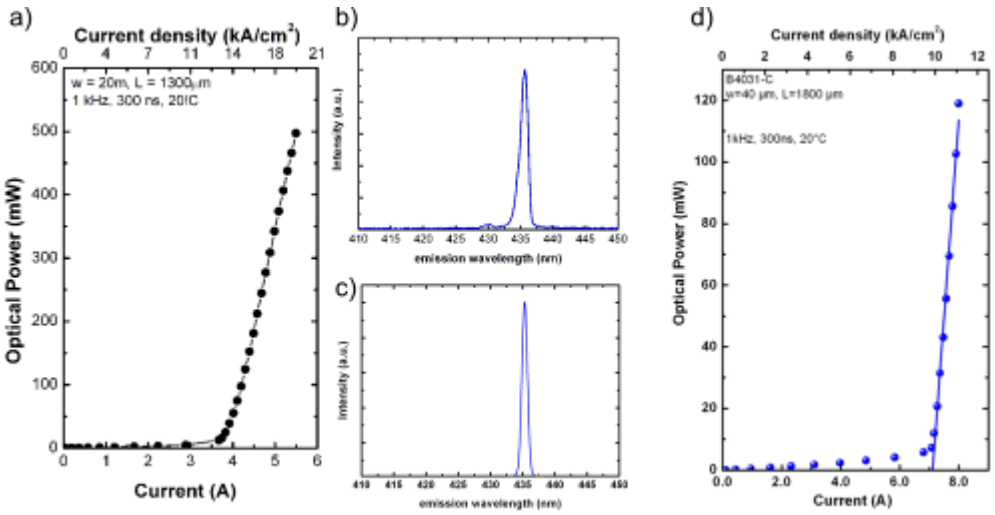

Fig. 2.7. L-I characteristics and emission spectra of BA laser diodes with a), b) structure 1 and c), d) structure 2, respectively.

Blue laser diodes were grown, fabricated and tested according to the optimized structure 2 as given in Fig. 2.4. For comparison also an unoptimized structure according to structure 1 (Fig. 2.4) was grown and fabricated as BA lasers as well. The LI curves are shown in Fig. 2.7. The improved structure exhibits a threshold current density of 10 kA/cm², a differential quantum efficiency of 0.14 W/A at a lasing wavelength of 435 nm. The sample with structure 1 exhibited a threshold of 14 kA/cm², a differential quantum efficiency of 0.31 W/A at a lasing wavelength of 435 nm. Here the lower threshold of the improved structure enables the fabrication of cw lasers although the threshold is still rather high.

In comparison to violet lasers, the blue lasers had not only a reduced slope efficiency but also a reduced yield. CL inspection revealed a degradation of the MQW active region as shown in Fig. 2.8a. Samples with the same active region but without p-side showed no degradation. Therefore the active region degraded during overgrowth, most possibly due to too high overgrowth temperatures. Consecutively new growth conditions for the magnesium doping of GaN and

AlGaN needed to be found. Laser structures overgrown with lower temperature showed a strong reduction of dark regions from 28% of the surface area to 1.9% of the area (Fig. 2.8b). The optimisation of GaN:Mg focused on a low resistivity at sufficiently low growth temperatures that still allow the growth of smooth GaN and AlGaN. Also a high portion of Mg atoms that are active as acceptors is needed in order to keep the total Mg concentration low and reduce optical losses by absorption at Mg in the waveguide.

The p-GaN optimisation had following results. In Fig. 2.9a the Mg-concentration, activated net acceptor densities N_A-N_D and carrier densities in dependence of the II/III ratio is shown. In Fig. 2.9b all the electrical properties, i.e. carrier concentration, mobility and specific resistance are shown. The magnesium incorporation shown in black depends linearly on the ratio of group II and group III element precursors. It is independent from different growth rates as well as different reactor pressures. Also activated acceptors measured by ECV and carrier densities are largely independent of growth parameters except II/III ratio. With Mg concentration >6x10^{19} cm^{-3} N_A-N_D does not increase anymore but decreases with increasing Mg concentration. In this region the layer is overdoped. Mg atoms form complexes or clusters and do not contribute to doping. Maximum acceptor concentration is reached for II/III ratio between 0.015 and 0.022. At lower II/III ratio the majority carrier type changes from p-type to n-type.

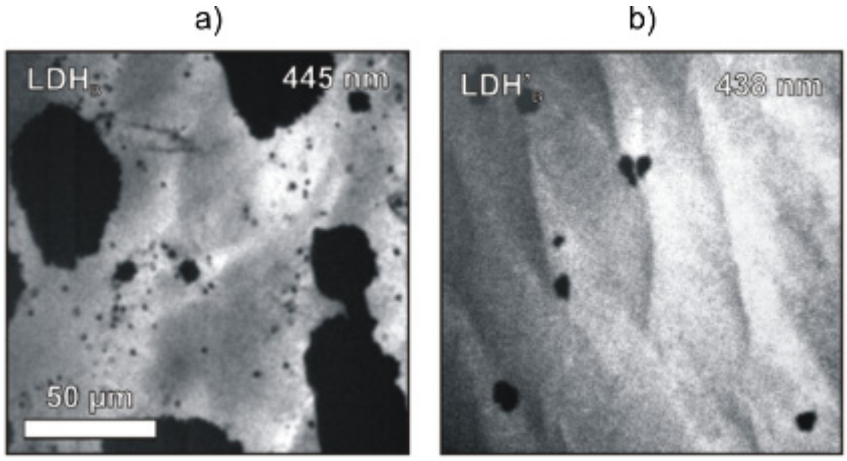

Fig. 2.8. Monochromotic CL micrographs recorded at the QW emission wavelength of laser diodes overgrown with p-(Al)GaN at a) high b) low temperature.

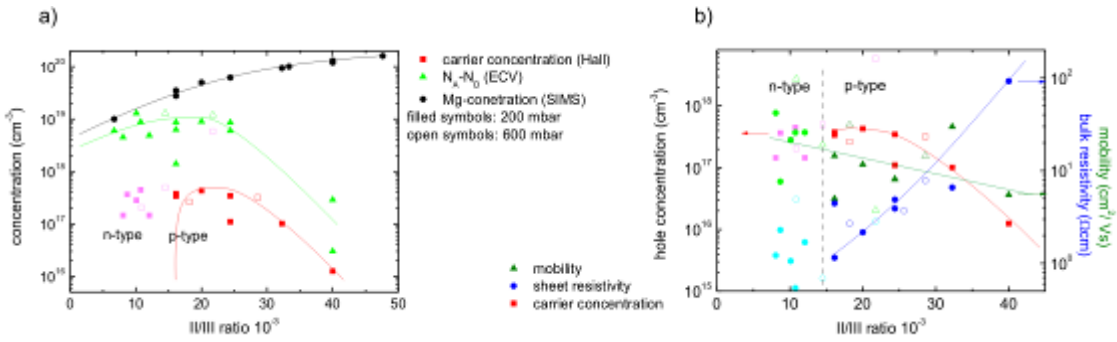

Fig. 2.9. a) Mg concentration, acceptor concentration and carrier concentration in dependence of II/III ratio for different growth conditions. b) Carrier concentration, mobility and resistivity in dependence of II/III ratio.

Below a II/III ratio 0.015, all samples were n-type. Possibly insufficient activation or another impurity caused n-type conduction. In the optimum region p-type layers with specific resistance of 1-2 Ωcm, 4-7x10^{17} cm^{-3} carriers and a mobility of 5-15 cm^2/Vs were achieved. LEDs with optimised and unoptimised p-layers were grown and the LI characteristics of indium dot quick tests were compared. As shown in Fig. 2.10a, the output power was strongly increased, especially at higher currents.

In order to compare optimized p-(Al)GaN growth conditions to the previous results 405 nm laser diodes were grown and fabricated as BA lasers. The characteristics are shown in Fig. 2.10. A threshold current density of 3.9 kA/cm^2 at a threshold voltage of 7.8 V was reached. The differential quantum efficiency was 0.3 W/A per facet. This is an improvement compared to previously grown laser structures. This shows that the new growth conditions for p-(Al)GaN do not only allow overgrowth of blue emitting active regions but lead to an overall improvement of the devices. The next step is therefore to apply the new conditions to laser structures emitting in the blue wavelength region.

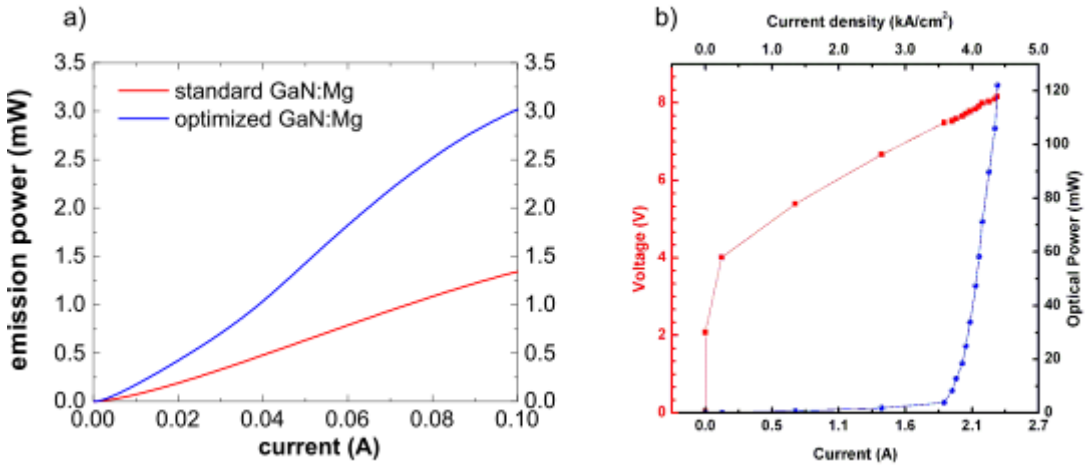

Fig. 2.10. a) LED characteristics of 405 nm LEDs with standard and improved conditions. b) Laser characteristics of 405 nm BA laser diode with optimized p-side.

2.3 Conclusion with respect to project objectives of WP1 in phase 2

According to the project objectives, laser heterostructures have been grown in the violet (410-430 nm) and blue (440 nm+) wavelength range by EPFL and TUB teams.

Violet laser parameters have been greatly improved in the second phase of the project. Threshold currents have been reduced to 40 mA, and slope efficiency was increased to 0.6 W/A (800x2 µm contact) with a reduced operation voltage of 6-7 V at 100 mA. In the growth of blue laser heterostructures p-doping was identified as a major issue, whereas the active region was degraded by too high p-GaN overgrowth temperature. New parameters for p-doped (Al)GaN have been found yielding better device parameters as it was tested in violet InGaN SCH lasers and blue laser diodes have been demonstrated.

Feedback to the hetero structure design from the analyzed multisection lasers as described in work package WP2.3 (section 3 of this document) as well as WP5 (section 6 of this document) lead to modification of the preliminary heterostructure design guideline that targeted the optimization of cw laser threshold and slope efficiency. The analyzes revealed that the most important parameters that affect the dynamics of multisection laser are the differential gain, ratio of the differential loss *da/dn* of the absorber to the differential gain *dg/dn* of the amplifier section, and the ratio of the carrier lifetime in the absorber to the carrier lifetime of the gain. Measurements showed that the differential gain can be increased by a reduction of the quantum well width due to a increased overlap of the electron and hole wave function that are separated by the Quantum Confined Stark Effect (QCSE). The associated increase of threshold current density by a reduction of spontaneous recombination time has less impact on the short pulse production capability. Differential absorption and lifetime in the absorber can be tuned by the absorber voltage. Very high negative bias (beyond the flat band voltage) can increase absorption and reduce the lifetime in the absorber. Here thinner quantum wells can improve the properties of the absorber, since the flat band voltage, the shift of the absorption edge with negative bias and the life time in the absorber are reduced. On the contrary the confinement factor is reduced reducing also the differential absorption. Here a proper trade off needs to be found experimentally. Another possibility are very thick quantum wells (> 8 nm). Since no experience exists with very thick quantum wells, thin quantum wells as used in previously grown lasers will be incorporated in the improved laser structures.

From GaAs based lasers it is known that strong Si doping of the barriers can reduce lifetime in the absorber. Since the carrier life time in the absorber is a critical parameter, new growth experiments studying the effect of this are planned, extending the growth plan into month 32 of the project as outlined in report D7.4.

3. Optical characterization of heterostructures (WP2)

In the second period of the project, the work was focused on optimization of heterostructure composition. For this several new wafers were grown in WP1 and characterized in WP2. Characterization included routine measurements of photoluminescence (PL) over the wafer, processing of some of the wafer into ridge waveguide devices and measurements of the optical gain and absorption. In this way the specification of optimized laser heterostructures, namely their differential optical gain, absorption, material loss etc., has been defined and the Milestone M2.2 has been reached [RD-5].

Below we spot some typical measurements.

3.1 Photoluminescence (PL) characterization of (AlGaIn)N laser epi wafers

In addition to the PL, µPL and µEL measurements of small epiwafer areas with high spatial resolution, the activities of the work packages WP2 includes optical characterization on a wafer scale. The purpose of these full wafer scans is to provide feedback to WP1 on the consistency of the growth runs over the entire wafer. An improvement of the homogeneity of the epitaxy on the wafer scale is mandatory to achieve high yield of the processed devices.

Photoluminscence mapping was performed before device processing. Typical results for a LD structure grown on a 2" wafer at EPFL are shown in Fig. 3.1. Peak wavelength, linewidth, and intensity of the photoluminescence signal are plotted on a full wafer map. A strong variation of the PL peak is observed, likely due to temperature inhomogeneities induced by the GaN substrate. The wavelength typically ranges between 393 and 400 nm. Wavelength and linewidth (full width at half maximum, FWHM) correlate nearly perfectly.

In the second period of the project, focused on optimization, LD structures have been growth with a different number of QWs and different width of QWs by keeping constant the active region length: 5 QWs of 2 nm (Fig. 3.1) and 3 QWs of 3.3 nm (Fig. 3.2).

For these particular wafers, the strongest PL emissions were found for longer wavelengths. For this wafer the correlation is counterintuitive: short wavelength regions show lower PL intensity while having smaller linewidth. Concerning the linewidth, mappings show a FWHM of 11 nm for the 5x2nm structure and slightly higher, 14, for the 3x3.3nm structure.

After processing, in electroluminescence, the FWHM for both structures seems to be higher than in photoluminescence measurements (Fig.3.3). This might be ascribed to a different injection process compared to optical pumping. Besides, the emission wavelength seems to redshift when increasing the pump current due to heating effect. Unfortunately the current flowing in the junction causes the degradation of the device probably due to higher p-type resistivity. We have been facing recurrent problem with p-type doping in our MOVPE reactor the past year. Meanwhile EPFL received a new system which already provided the consortium with novel laser structures.

These wafers will be used to fabricate devices in the third period of the project.

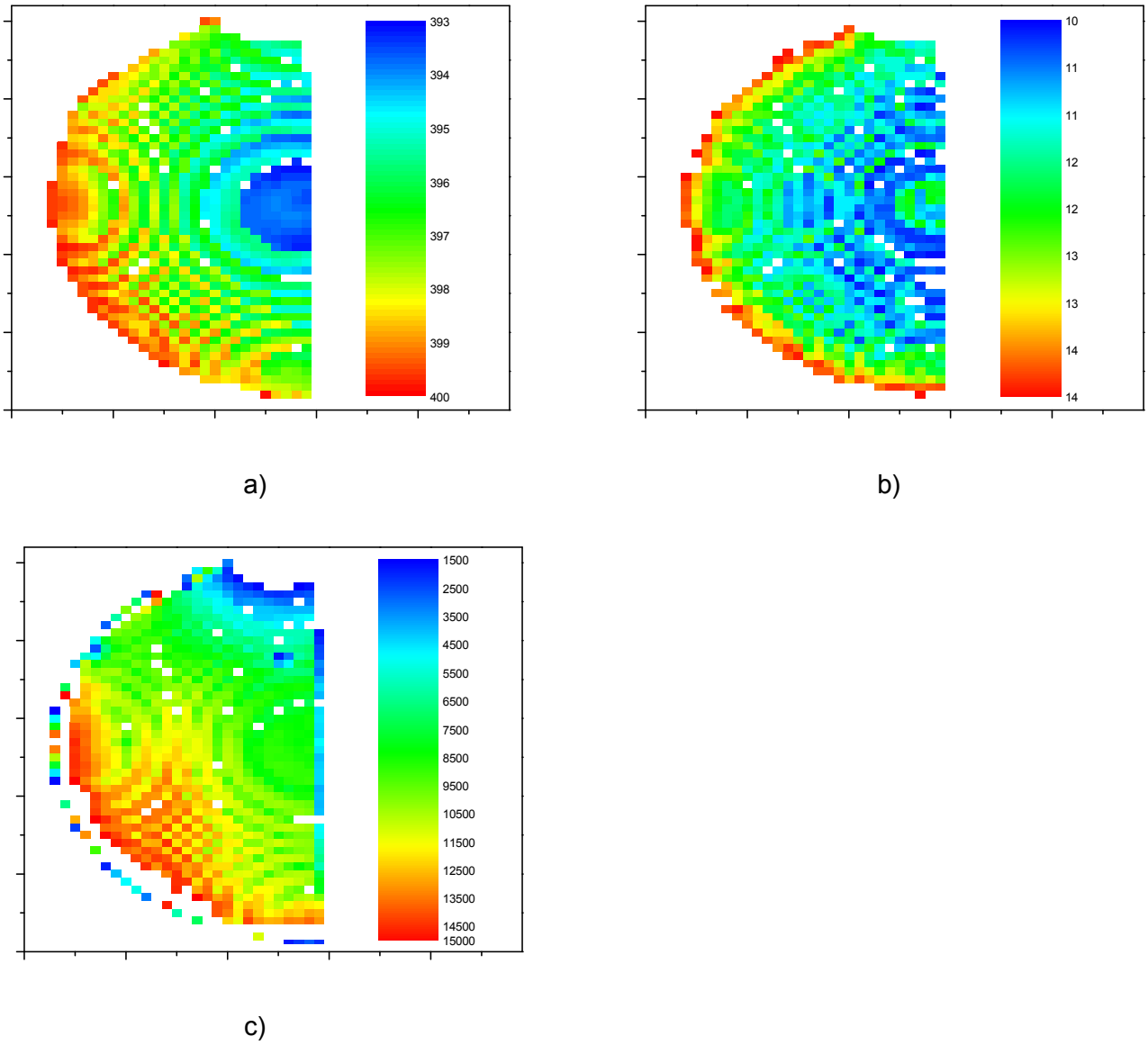

Fig. 3.1. 300 K PL mapping of the 5 QWs of 2nm structure. The individual maps show the distribution of (a) peak wavelength, (b) linedwidth and (c) peak intensity of the photoluminescence across the half wafer (sample A2191).

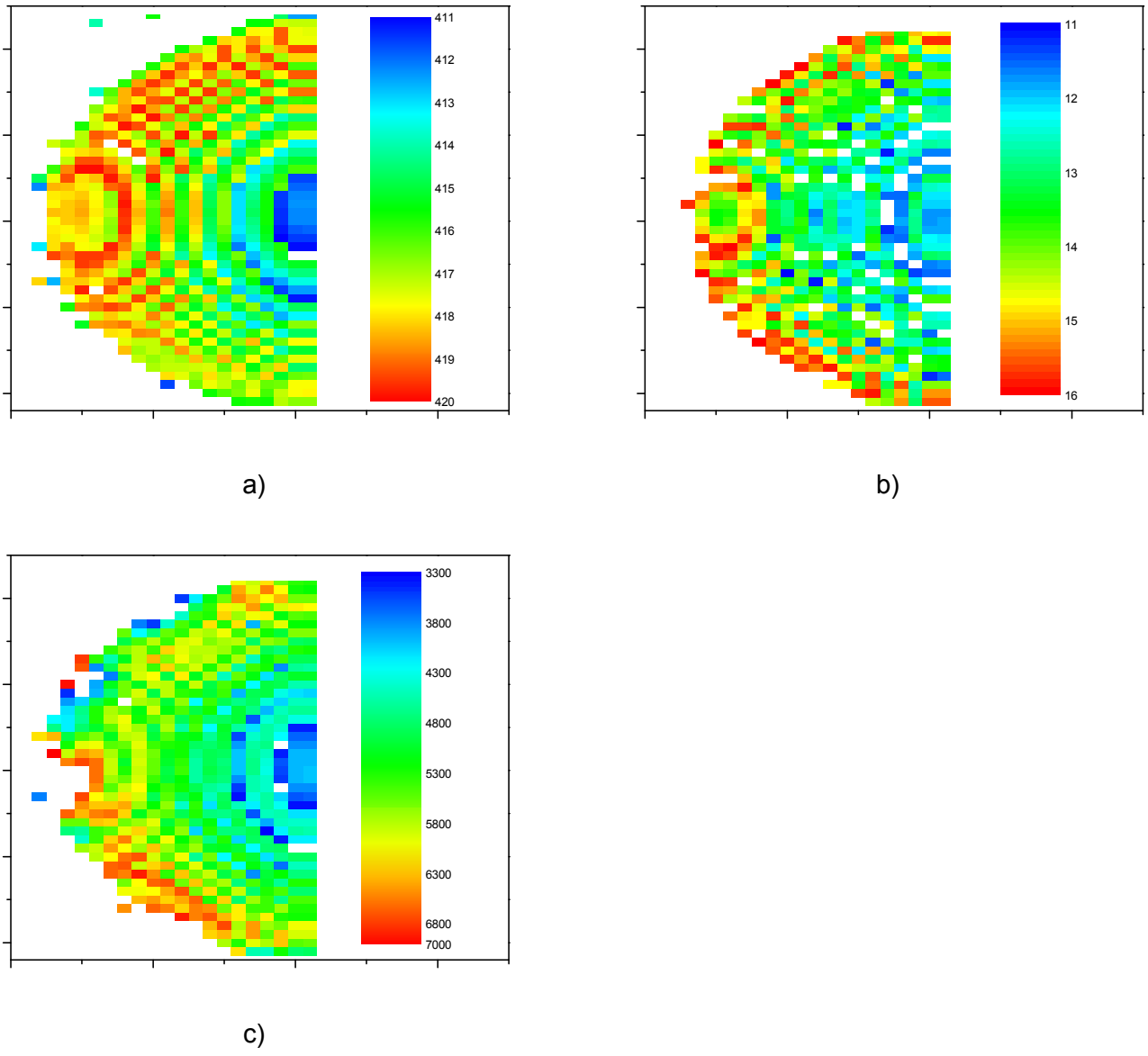

Fig. 3.2. 300 K PL mapping of the 3 QWs of 3.3nm structure. The individual maps show the distribution of (a) peak wavelength, (b) linedwidth and (c) peak intensity of the photoluminescence across the half wafer (sample A2227).

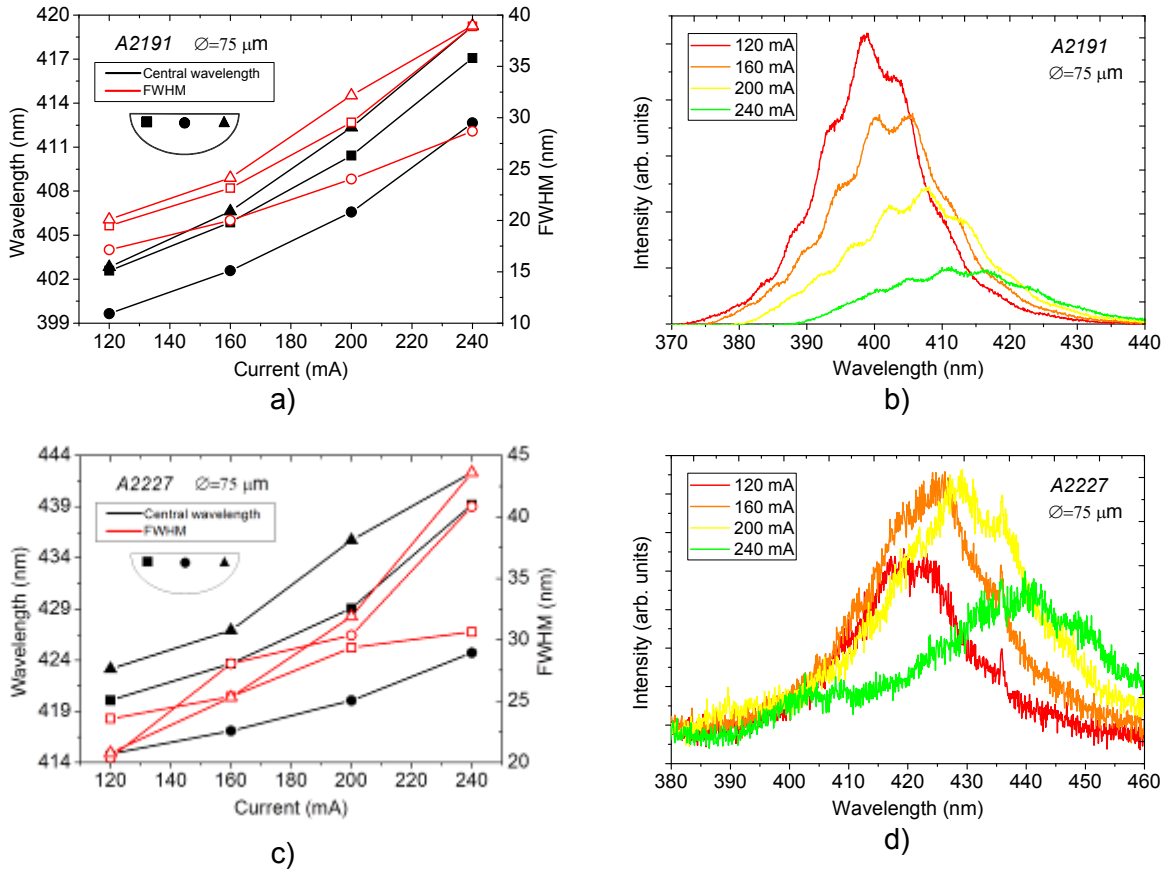

Fig. 3.3. Central wavelength and FWHM of the electroluminescence spectra as a function of the injected current for the the 5 QWs of 2nm structure (Fig. 19a and 19b) and for the 3 QWs of 3.3nm structure (Fig. 19c and 19d).

3.2 Hakki-Paoli optical gain spectroscopy

Measurement of the optical gain spectra is part of activities of the work package WP2. The employed Hakki-Paoli [Hakki-74] method allows gain measurements in fully processed devices. All gain spectra were measured in cw operation of the LD.

On one hand, the gain spectra provide important feedback to WP1 on the quality of the grown multiple QW separate confinement heterostructures. On the other hand, they provide the experimental data which are necessary as input for the refinement of the model parameters and in the design of multisection laser cavities, both within WP3.

The Hakki-Paoli method has been described in the report of deliverable D2.1 [RD-3] and in the diploma thesis and PhD thesis of Wolfgang Scheibenzuber [Scheibenzuber-09,Scheibenzuber-11a].

Table 3.1 lists laser diodes processed by EPFL samples A1902 (grown in first period), A2109 and TBU Berlin samples B2725 (grown in second period) for which gain and absorption spectra have been measured. The first two letters and following two digits identify the individual laser diode on the wafer. The next three numbers are ridge length (600 µm, 800 µm, or 1000 µm), ridge width (2 µm or 4 µm) and absorber length (0 for no absorber, 25 µm, 50 µm, and 75 µm).

For LDs with absorber, the ridge length is the combined length of gain and absorber sections. For the absorption measurements LDs with absorber on one end of the ridge waveguide have been used. This geometry is shown in Fig. 3.4.

For the purpose of comparison, we also provide reference to LD processed from A1902 wafer grown in the first period of the project. Some of its optical characteristics have been measured in [RD-5]. In the second period we evaluated its carrier recombination and optical gain compression coefficients.

Laser diodes for gain measurements	Laser diodes for absorption measurements
EPFL A1902	
DE41_600x2x0	DE43_600x2x50
CE45_600x4x0	CE44_600x2x75
CB51_800x2x0 DF31_800x2x0	DF32_800x2x25 DF33_800x2x50
DF35_800x4x0	CB54_800x2x75
CB55_800x4x0	DA43_1000x2x50
EA31_1000x2x0	DA44_1000x2x75
EPFL A2109	
C1_D1_600x2x0	B1_D11_600x2x50
C1_D5_600x3x0	C2_D3_600x2x50
C2_D1_600x2x0	C2_D6_600x3x50
C2_D5_600x3x0	D1_D6_600x3x50
D1_D1_600x2x0	F3_D2_800x2x50, 800x3x50
F3_D1_600x2x0	D3_D6_800x3x50
F3_D5_600x3x0	F4_D6_800x3x50, 800x3x150
F4_D5_800x3x0	
TU Berlin B2725	
B1D20_600x3.0x0	
B1D22_600x2.0x0	
B2D19x600x2.5x0	
B2D23x600x2.5x0	

Table 3.1. Laser diodes from EPFL and TU Berlin used for gain- and absorption spectroscopy.

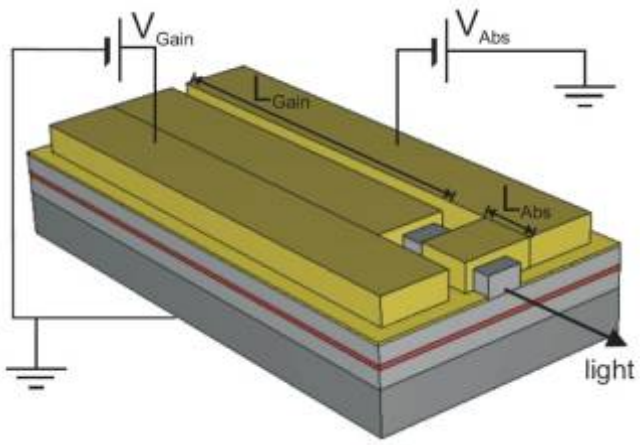

Fig. 3.4. Laser diode with gain and absorber section in the configuration used for Hakki-Paoli gain and absorption spectroscopy.

3.2.1 Results on gain measurements in EPFL SCH laser diodes

Gain spectra as function of forward current are plotted in Fig. 3.5 for LDs with different ridge geometries. The internal losses are given by the modal gain in the limit of long wavelengths, i.e. in an energy region where the absorption by the QWs is negligible. For the LD from growth run A2109 the internal losses were as low as 20 cm^{-1} to 30 cm^{-1}. This demonstrates the improvement achieved when compared to LDs presented in previous report [RD-5], where internal losses were in the range between 35 cm^{-1} and 45 cm^{-1}. The new value of only 20 cm^{-1} is only a factor two larger than that of commercial LDs, where values of $\alpha_i \sim 10$ cm^{-1} have been demonstrated. Probable sources for the relatively high internal losses are a large overlap of the waveguide mode with the magnesium doped p-waveguide layers or substrate modes. An optimization of the vertical laser structure should lead to a reduction of the internal losses by at least a factor of two.

The differential gain can be read directly from the gain spectra. For the spectra of Fig. 3.5 the differential gain is 2.2 cm^{-1}/mA, 0.9 cm^{-1}/mA, for laser diodes of growth run A2109 c1x600x2x0. This is a significant improvement compared to LDs measured earlier [RD-5] with a differential gain of 0.60 cm^{-1}/mA, 0.68 cm^{-1}/mA, and 0.55 cm^{-1}/mA for the LDs with 600 µm, 800 µm, and 1000 µm ridge length, respectively. To calculate the (differential) material gain, one needs the confinement factor Γ, which can be calculated for a given vertical structure. It can also be approximately calculated from the measured far field distribution. To get the differential gain as function of carrier density, the relation between carrier density and current density has to be determined. This can be done by a measurement of the carrier lifetime as function of current density.

From internal losses measured by Hakki-Paoli method and slope efficiency, the injection efficiency can be calculated. The corresponding values are η_{inj} = 45% for epitaxy A1902 and η_{inj} = 80% for A2109, calculated from slope efficiencies of dP/dI = 0.27 W/A and dP/dI = 0.73 W/A, respectively. As differential peak gain dg/dI depends not only on QWs, but also on device geometry and injection efficiency, one has to compare the differential gain with respect to current density to draw conclusions on the quality of the quantum wells. The corresponding values are dg/dI_{inj} = 0,033 $cm^{-1}/(Acm^{-2})$ and dg/dI_{inj} = 0,034 $cm^{-1}/(Acm^{-2})$ for A1902 and A2109, respectively. This demonstrates that the QW quality is comparable, while improvements are due to reduction of internal losses and increase in injection efficiency.

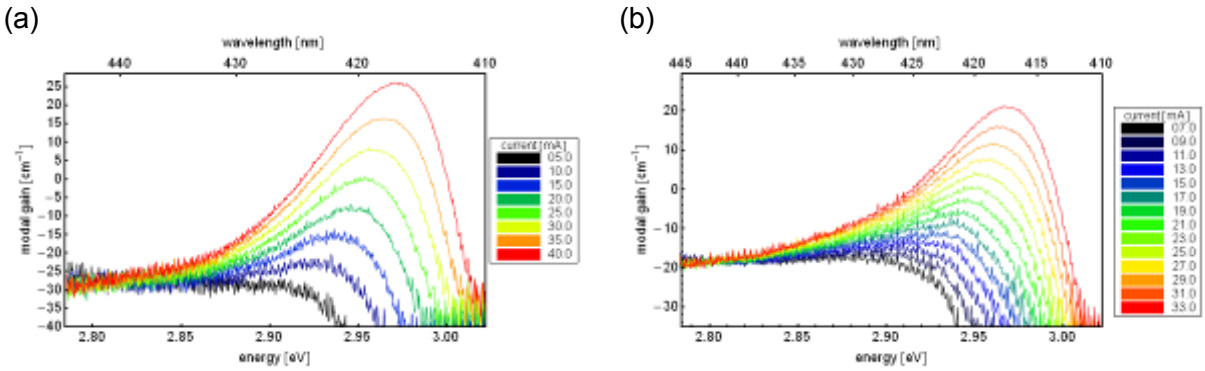

Fig. 3.5. Gain spectra for LDs of two different growth runs with 600 µm ridge length and (a) 2µm and (b) 3 µm ridge width as function of current. Samples: A2109 c1x600x2x0, A2109 c2x600x3x0.

As more laser diodes have been measured, we have a better statistics of device characteristics (see Table 3.2). The results of these measurements are used in section 3.5 to refine the dynamic model parameters.

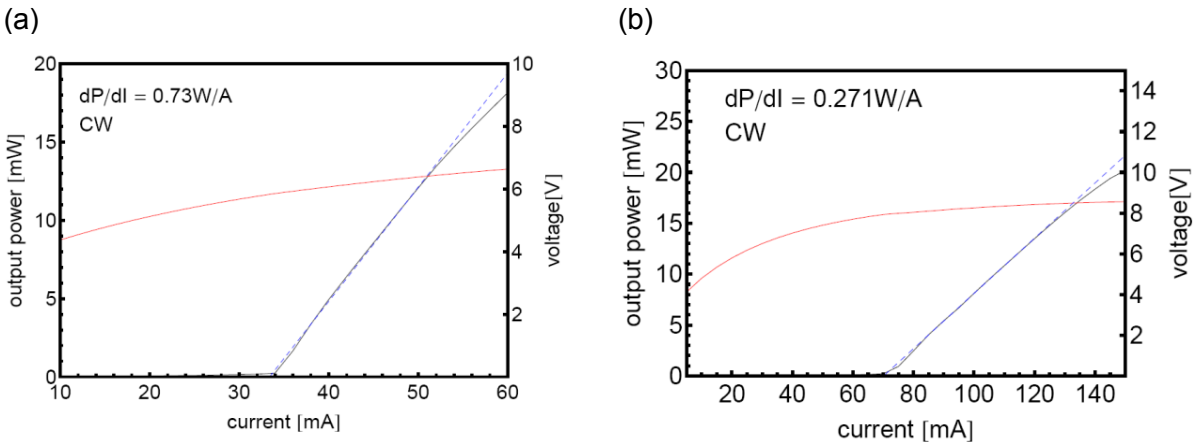

Fig. 3.6. Corresponding IP curves for the same LDs as shown in Fig. 22 for epitaxy (a) A2109 c1x600x2x0 and (b) A1902 DF3x800x2x0.

3.2.2 Results on gain measurements in TUB SCH laser diode

Optical gain spectra were also measured for a series of violet laser diodes from TU Berlin. The Hakki-Paoli gain spectra for four LDs are shown in Fig. 3.7. The internal losses derived from these gain spectra are about 35 cm^{-1}. The variation of the internal losses from LD to LD is relatively low. At least one laser diode showed a strong dependency of the internal loss on injection current (Fig. 3.7(c), LD number B2D19x600x2.5x0).

The spectra of a 600 µm long LD shown in Fig. 3.7(c) shows a dip at 2.95 eV. This dip is not a feature of the real gain spectra, but a measurement artifact caused by the superposition of the gain spectra of different lateral modes. As lateral modes have different effective refractive indices, the produce longitudinal mode combs of different mode spacing, which run in and out of phase as function of wavelength. This causes an apparent modulation of the gain spectra. This behavior is typically seen in broader area LDs.

From one of the LD (B1D22_600x2.0x0) optical output power and forward voltage were measured as function of injection current (IP and IV curves, see Fig.3.8). The injection efficiency derived from the combination of Hakki-Paoli spectra and IP curve for this LD is 70%.

Epitaxy	A1902	A2109	B2725
Devices measured	5	10	4
internal losses	30 – 40 cm^{-1}	20 – 30 cm^{-1}	30 – 40 cm^{-1}
inj. Efficiency	40 - 50%	60 - 90 %	~70 %
dg/dj_{inj}	0,020 – 0,035 $cm^{-1}/(Acm^{-2})$	0,030 – 0,040 $cm^{-1}/(Acm^{-2})$	0.0047 – 0.0059 $cm^{-1}/(Acm^{-2})$

Table 3.2. Statistics of devices characteristics for 15 devices from three growth runs (EPFL and TU Berlin)

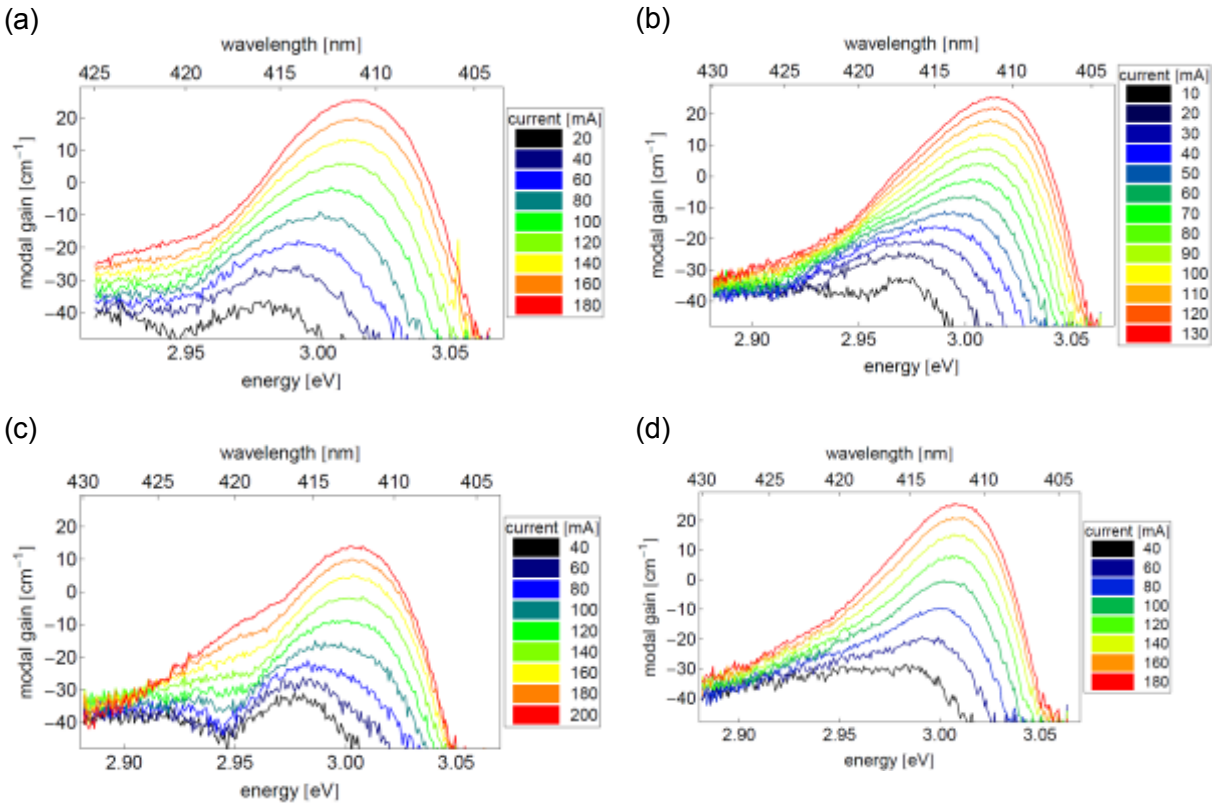

Fig. 3.7. Gain measurements from violet LD (TU Berlin) from LDs (a) B1D20_600x3.0x0, (b) B1D22_600x2.0x0, (c) B2D19x600x2.5x0, and (d) B2D23x600x2.5x0.

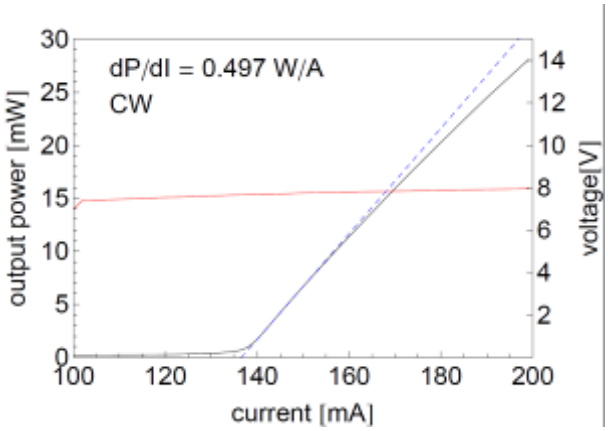

Fig. 3.8. IP curve of violet LD (TU Berlin) B1D22_600x2.0x0.

internal losses ai	20 – 30 cm^{-1}
inj.efficiency η_{inj}	60 - 90 %
dg/dj_{inj}	0,030 – 0,040 $cm^{-1}/(Acm^{-2})$
absorption α_{abs}	20 cm^{-1} (min), 220 (max)
Lifetime in absorber τ_{abs}	400 ps (min), 3 ns (max)
SRH-coeff. A	$4.2x10^{7}$ s^{-1}
sp. em.-coff. B	$2.1x10^{-6}$ cm^{2} s^{-1}
Auger-coeff. C	$2.3x10^{-18}$ cm^{4} s^{-1}
transp. carrier density n_{tr2D}	$9.6x10^{12}$ cm^{-2}

Table 3.3. Parameter set for laser diodes of growth run A2109.

3.2.3 Determination of Recombination coefficients of GaN-based laser diodes from growth run A2109

We measure the charge carrier recombination coefficients of InGaN quantum wells by analyzing the dynamical properties of (Al,In)GaN laser diodes emitting in the violet spectral range [Scheibenzuber-11]. Relaxation oscillations and turn-on delays are fitted to a rate equation model including a charge carrier density dependent recombination rate. Using optical gain spectroscopy we can directly determine the injection efficiency of the devices and thereby separate the effect of charge carrier leakage from that of carrier recombination. We find a third-order recombination coefficient of (4.5+/-0.9) x 10^{-13} cm^{6} s^{-1} which is in agreement with theoretical predictions for phonon- and alloy-disorder-assisted Auger scattering.

These values together with the other parameters derived from Hakki-Paoli gain spectroscopy and IP curve provide a rather complete parameter set for a laser diodes of the series A2109 (see Table 3.3). Of course one has to keep in mind that these values scatter, as described in Table 3.2.

3.2.4 Group velocity and group velocity dispersion (GVD)

The Hakki-Paoli method allows also measuring the mode spacing from which group velocity and group velocity dispersion (GVD) can be derived. The technique to measure the group velocity and group velocity dispersion has been reported in [RD-5]. The data for samples tested in second period are shown in Table 3.6.

3.2.5 Measurement of absorption in two-section laser diodes

Section 3.2.1 (above) reports on the modal gain measurements previewed by the work plan [AD-1]. In the project, we go further and we find out a possibility to measure the modal absorption in the absorber section of a multi-section LD. Here we briefly reproduce description of this technique [RD-5] and provide results of new measurements in Table 3.4.

The possibility to tailor absorption is crucial for reaching the short pulse operation of multi-section LDs. We used the Hakki-Paoli method in combination with the multi-section LD cavity design to measure the modal absorption as function of the bias voltage of the absorber section in LDs with different ridge and absorber length. The measurements gave consistent results for the absorption per length as a function of bias voltage. These numbers can now be used in the simulation and design of the short pulse LDs.

In order to obtain bias voltage-dependent absorption spectra of the InGaN quantum wells in the absorber section, we compare optical gain spectra taken at negative absorber bias and forward bias [Scheibenzuber-10a, Scheibenzuber-10b]. The measured gain from a multisection laser diode is an average of the gain and absorption in the two sections, weighted with the lengths of the sections. The absorption coefficient is then calculated from the measurements in the following way:

$$\alpha_V(\hbar\omega) = \frac{L_{gain}}{L_{abs}} g_{\mathrm{FW}}(\hbar\omega) - \frac{L_{gain} + L_{abs}}{L_{abs}} g_V(\hbar\omega)$$

where L_{gain}, L_{abs} are the lengths of the gain and absorber section, respectively. V is the absorber bias voltage, g_{FW} is the gain spectrum for both sections at equal forward voltage and g_V is the gain spectrum at the absorber bias voltage V.

The measured absorption for a LD with 50 µm absorber length is shown in Fig. 3.9 for a laser diode with 435 nm peak wavelength. In contrast to the behavior known from LDs of other III-V material combinations, the absorption decreases with increasing reverse bias. This surprising dependency of absorption on bias voltage can be understood if the quantum confined Stark effect (QCSE) is taken into account. For a large reverse bias, the band edge in the absorber section is blue-shifted, resulting in a decrease of the overlap of the absorption spectrum with the laser wavelength, which is given by the gain section under forward bias.

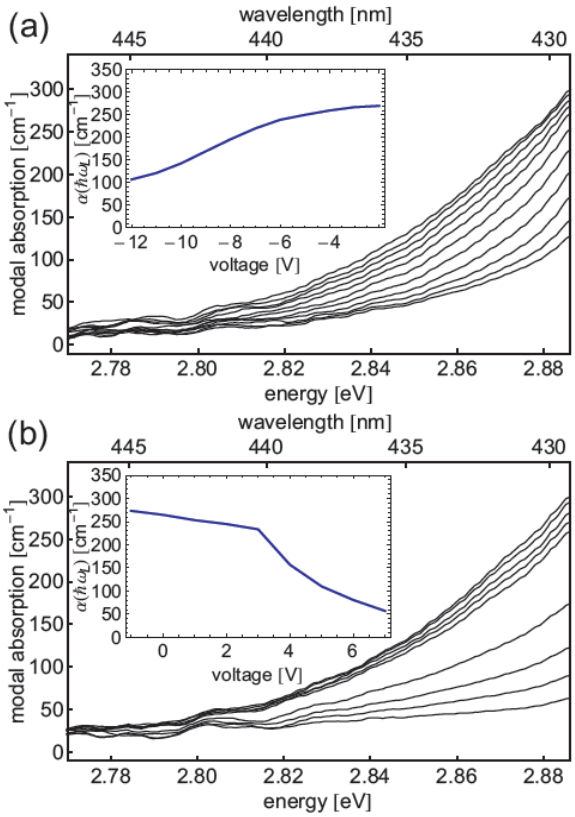

Fig. 3.9. Absorption spectra of a 50 µm absorber section in a 810 µm cavity at absorber bias voltages from -12 to -2V (a, bottom to top curve) and -1 to 7V (b, top to bottom curve). The insets show the absorption at the laser wavelength as a function of absorber voltage [Scheibenzuber-10a].

Our measurement technique gives the modal absorption coefficient which is given by the product of the material absorption coefficient of the InGaN quantum wells, and the overlap of the photon mode in the laser waveguide with the QWs which is given by the confinement factor Γ For our samples, Γ = 0.0195 is calculated using a 2D-waveguide simulation. Dividing our results by the confinement factor gives a maximum value of about 1.3x10^4 cm^{-1} for the absorption at the laser wavelength 413 nm. A comparison of this value to Ref. [Renner-02], which reports a plateau of the quantum well absorption at about 7 x10^4 cm^{-1}, reveals that the spectral range examined in our measurements lies at the low energy tail of the step-like absorption spectrum.

The interpretation of the unusual behavior of the absorption as function of bias voltage by the QCSE is confirmed by absorption curves measured for a near UV laser diode at 413 nm (see Fig. 3.10). Due to the lower indium content in the quantum wells, the flat band condition is now reached at a reverse bias of -9 V. The corresponding internal field at low forward bias is 1 MV/cm. For reverse bias larger than -9 V, the absorption increases again, as the quantum confined Stark effect reverses its sign, and the gain spectra are red shifted, again. The relation between internal fields and external voltage depends strongly on the design of the active region, particularly the width of the surrounding undoped layers and the indium content of the quantum wells.

The experimental fact that the absorption exhibits a maximum at about 0 V bias voltage has important consequences for the pulsed operation. Q-switching may still be possible in the range of high backward voltages, but with reversed sign of the voltage pulse needed for Q-swichting.

For mode-locking operation the inverted sign of the slope has a consequence for the phase shift between HF modulation and pulse sequence, although this may be hard to measure. Of general importance is the saturation of the absorption at a much lower value when compared with a material system which does not exhibit the QCSE. This has to be implemented in the simulations of the LD dynamics and design of the laser. This may affect both the epitaxial layer structure, in order to modify the impact of the QCSE on the gain and absorption spectra, as well as the ridge geometry, in particular the relative length and position of the absorber section(s).

The results of these measurements are used in section 3.5 to refine the dynamic model parameters.

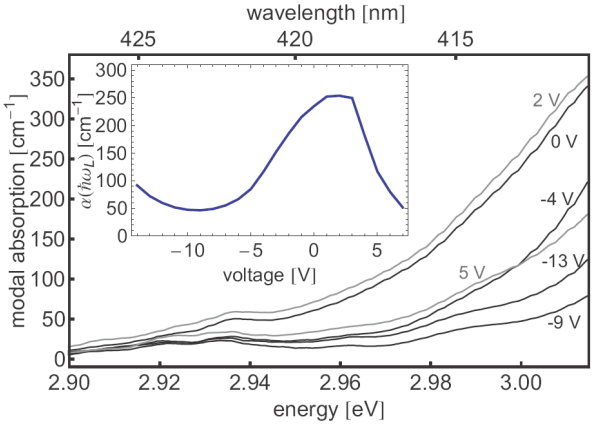

Fig. 3.10. Absorption spectra for a 413 nm laser with 50 µm absorber at bias voltages from -13V to 5V (for reasons of clarity, the curves that correspond to voltages > 0 are drawn in gray). The inset shows the absorption at the laser wavelength of 413nm as a function of absorber voltage. [Scheibenzuber-10b].

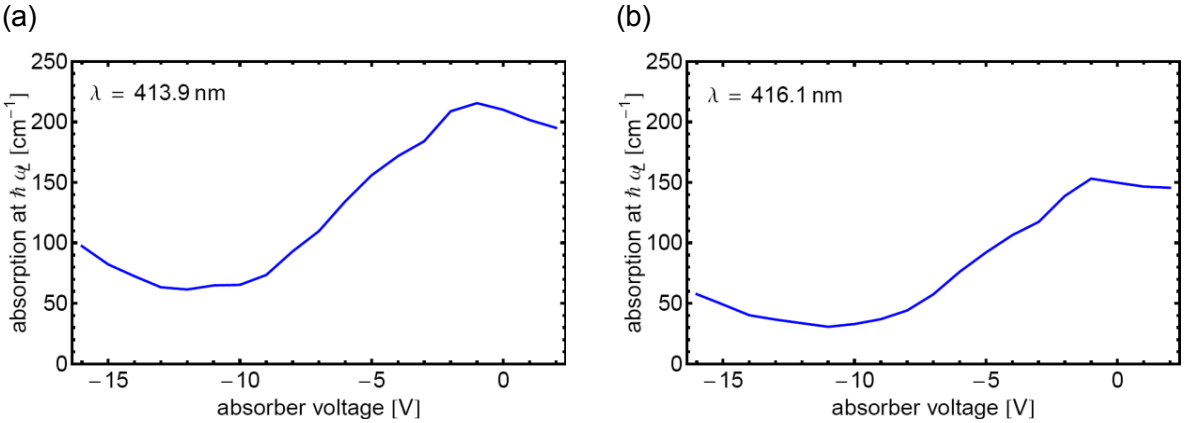

Fig. 3.11. Absorption as function of absorber voltage for LDs (a) A2109 f3x800x2x50 (800 µm total ridge length, 2 µm ridge width, 50 µm absorber length) and (b) A2109 f3x800x3x50 (800 µm total ridge length, 3 µm ridge width, 50 µm absorber length)

Absorption measurements were also performed for LDs from the new growth run A2109. Representative absorption spectra are shown in Fig. 3.11, the range of measured minimum and maximum absorption is collected in Tab. 4. The absorption in A2109 was reduced when compared to A1902. This is because of the thicker QWs in the new LD series.

	A1902 (7 devices measured)	A2109 (3 devices measured)
max. absorption	250 – 300 cm^{-1}	150 – 220 cm^{-1}
min. absorption	50 – 120 cm^{-1}	20 – 100 cm^{-1}

Table 3.4. Comparison of minimum and maximum absorption for LDs from the first and second batch.

3.3 Charge carrier lifetime in absorber section

The dynamical behavior of the absorber is determined not only by the absorption coefficient, but also by the charge carrier lifetime in the absorber, which can considerably deviate from the lifetime in the gain section due to the difference in internal field and the escape of charge carriers from the quantum wells in the negatively biased absorber section. The charge carrier lifetime in the absorber is analyzed by applying a variable bias voltage superimposed with a rectangular current pulse to the absorber of a multi-section laser diode with front absorber geometry (see Fig. 3.12a) and measuring the decay of the electroluminescence after a current pulse. The charge carrier lifetime is given by twice the electroluminescence decay time τ_{EL}. For this measurement, a fast electric pulse generator with 100 ps rise/fall time and a streak camera system with a temporal resolution better than 1% of the set time range and a spectral resolution of 0.2nm are employed. The pulse width is set to 80 ns and the magnitude of the pulse is adjusted to reach a current density of 2 kA/cm^2, which is roughly half the threshold current density of single section lasers from the same epitaxy. The gain section is not contacted during this measurement. Figure 3.12b shows a representative measurement from a multi-section laser diode with 4.5 nm quantum wells, 800 µm cavity length and a 100 µm absorber. The charge carrier lifetime decreases drastically with increasing negative bias, from 3.6 ns at +3 V to about 400 ps at -15 V.

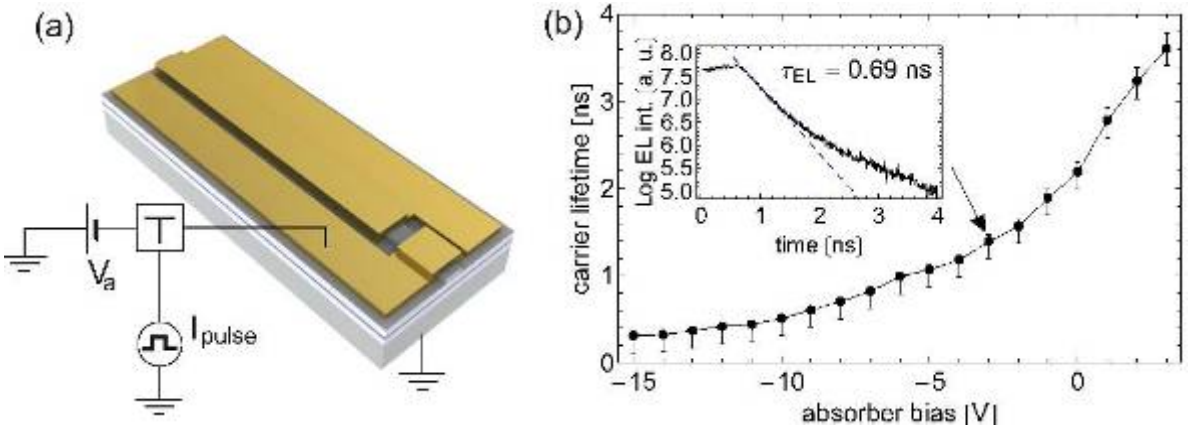

Fig. 3.12. Measurement scheme for the charge carrier lifetime in the absorber (a) and charge carrier lifetime in the absorber as a function of applied bias voltage (b). The asymmetric error bars are due to a systematic overestimation of the decay time because of the finite fall time of the electric pulse. The inset shows an example logarithmic plot of the electroluminescence decay at -3V bias, where the decay time is obtained from a linear fit at the end of the electric pulse (dashed line).

At a negative bias, the charge carrier lifetime τ_a a is composed of the charge carrier escape time τ_{esc}, the radiative lifetime τ_{rad}, and the nonradiative lifetime τ_{nr}, which includes defect-related and Auger recombination:

$$\tau_a = \left(\tau_{esc}^{-1} + \tau_{rad}^{-1} + \tau_{nr}^{-1}\right)^{-1}$$

The reduction of the charge carrier lifetime is due to an increase of radiative recombination and the escape of charge carriers from the quantum wells via thermionic emission and tunneling [Sch07]. The applied bias voltage adds to the field of the p-n junction, which causes a tilt of the band profile and a reduction of the internal fields in the QWs. This leads to an increase of the wave function overlap from about 20% at forward bias to nearly 100% and thereby enhances the radiative recombination. In addition, the tunnel barrier for charge carriers in the QWs is reduced and charge carriers are swept out of the active region, which further decreases their lifetime.

3.4 Differential gain and gain compression

The relaxation behavior of a laser diode upon turn-on is determined by several internal parameters, such as the differential gain, the gain saturation and the charge carrier lifetime. These parameters can be obtained from a systematic analysis of the frequency and damping of the relaxation oscillations and the turn-on delay. These properties are measured using a streak camera with a temporal resolution better than one percent of the set time range. Solving the rate equations for carriers and photons for small perturbations ΔN and ΔS from steady state yields the functional dependence of the oscillation frequency on pump current,

$$f_r = \frac{1}{2\pi}\sqrt{\frac{dg}{dN}\eta_{inj}\frac{c}{e}(j - I_{th})}$$

The differential gain per carrier number, $\frac{dg}{dN}$ is defined as the derivative of the modal gain with respect to the number of charge carriers in the active region, evaluated at the laser threshold and the laser emission wavelength. It cannot be obtained from optical gain spectroscopy alone, because that method does not allow an estimation of the charge carrier number. As can be seen from the equation above, $\frac{dg}{dN}$ can be determined from a linear fit of the square of the oscillation frequency to the pump current. Figure 3.13 illustrates this procedure.

As the equation for the oscillation frequency contains the speed of light in the medium c and the injection efficiency η_{inj}, these parameters have to be measured by high resolution electroluminescence spectroscopy in order to extract the differential gain form the relaxation frequency. Figure 3.14 shows optical gain spectra and output characteristics, from which the injection efficiency is extracted. For this sample, the internal losses are α_{int} = 18 ± 1 cm^{-1} and the mirror losses of the two uncoated facets, the reflectivity of which is approximately 17%, are α_m = 30 ± 1 cm^{-1}. The slope efficiency is 0.62 W/A per facet, which corresponds to an injection efficiency of (68 ± 2) %. This value indicates an insufficient function of the electron blocking layer and a considerable loss of charge carriers due to electron overflow. The group refractive index is calculated as n_{gr} = 3.84 ± 0.05 from the spacing of adjacent longitudinal modes, which is 37 pm at the laser wavelength. Table 3.5 summarizes the extracted parameters. Inserting these parameters into the equation for the frequency of the relaxation oscillations yields a

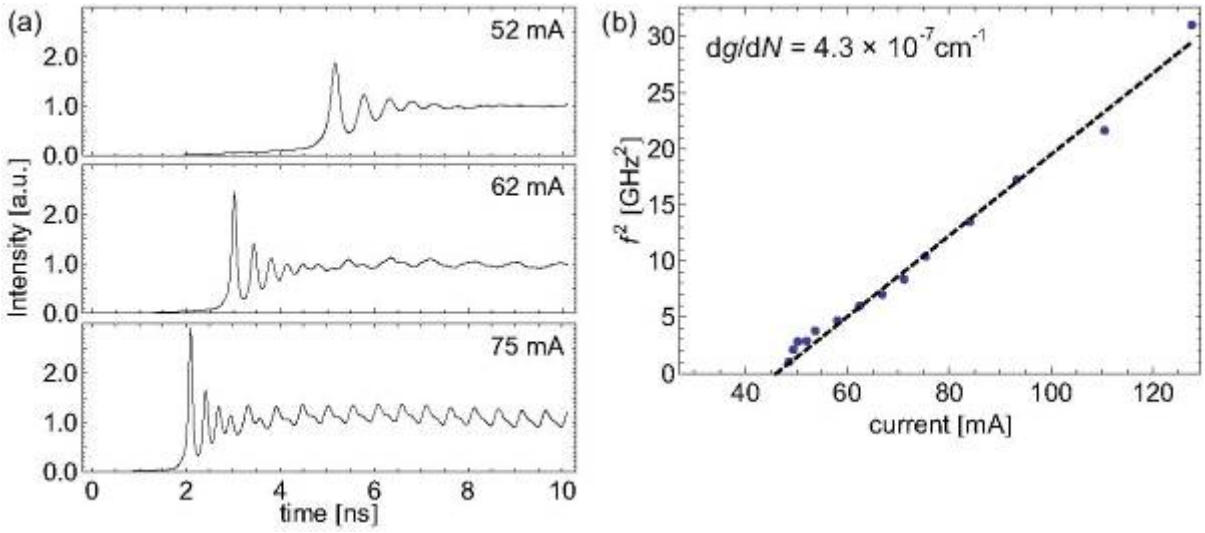

Fig. 3.13. (a) Laser emission intensity as a function of time for pump currents of 52mA (top), 62mA (center) and 75mA (bottom). The electrical excitation pulse is turned on at t = 0. (b) Relaxation oscillation frequency squared versus pump current (data points) and linear t to the data (dashed line).

differential gain per carrier number of $\frac{dg}{dN}$ = 4.3 x 10^{-7} cm^{-1}, which corresponds to $\frac{dg}{dN}$ = 7.0 x 10^{-18} cm^{-1}/cm^{-3} in the charge carrier density dependent notation. The differential gain per current at the laser wavelength 415.5 nm, extracted from optical gain spectroscopy, is $\left.\frac{dg}{dI}\right|_{\lambda=const.}$ = 1.5 ± 0.1 cm^{-1} mA^{-1}.

The gain saturation parameter k_{sat} describes the reduction of the gain at high photon density due to spectral hole burning [Pet91]. It acts as a damping term for the relaxation oscillations, and can thus be determined from a comparison of the time-dependent solution of the rate equations to the relaxation oscillations. Figure 3.15 shows time evolutions of the photon number in the cavity, simulated using carrier and photon rate equations, for different values of k_{sat}

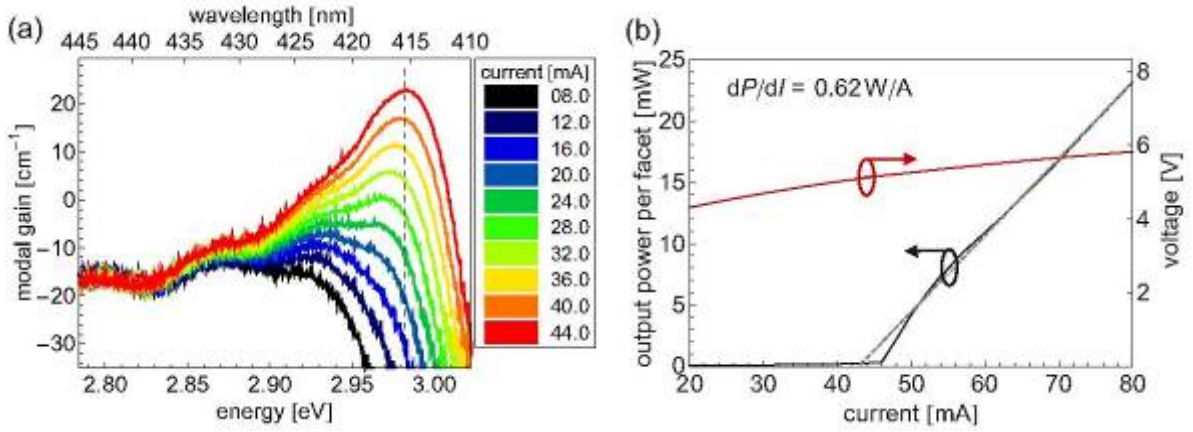

Fig. 3.14. (a) Optical gain spectra at currents from 8 mA to 44 mA in steps of 4 mA (from bottom to top). The dashed line marks the laser wavelength 415.5 nm. (b) Optical output power per facet and operating voltage in continuous wave operation. The dashed gray line is a linear fit to the output power above threshold.

compared to the experiment. The best agreement is achieved for k_{sat} = (4 ± 1) x 10^{-8}. To obtain a parameter that is independent of device geometry, this value has to be transformed into a photon-density dependent quantity. Therefore, it is multiplied by the active region volume and divided by the confinement factor, yielding a value of $\tilde{k}_{sat}$ = (2.2 ± 0.6) x 10^{-17} cm^3.

mirror losses	30±1 cm^{-1}
internal losses	18±1 cm^{-1}
dg/dI_{inj}	1.5±0.1 cm^{-1} mA^{-1})
inj. Efficiency	0.68±0.02
group ref. ind.	3.84±0.05

Table 3.5. Device parameter extracted from optical gain spectra and PI-curve (Fig. 39).

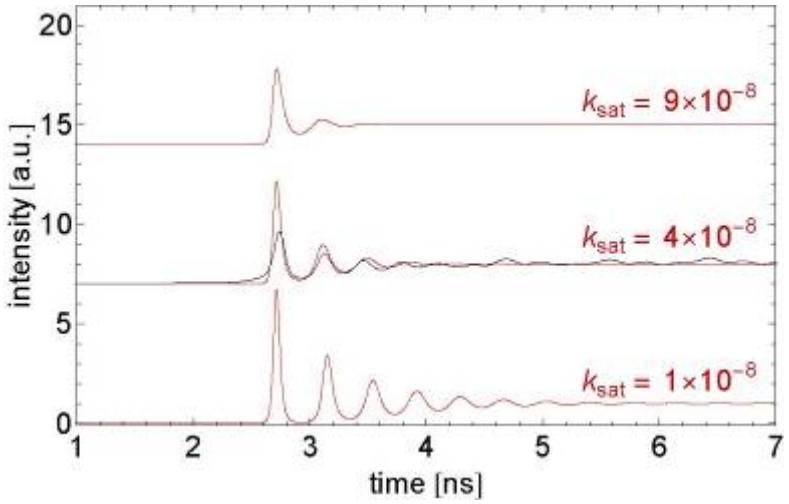

Fig. 3.15. Simulated time evolution of photon number in the cavity for k_{sat} = 1, 4, 9 x 10^{-8} (bottom to top) at a pump current of 67 mA. Curves are shifted vertically for clarity. The black line shows the experimental intensity trace at 67 mA.

3.5 Dynamic model parameters for multisection InGaN/GaN QW LDs

The consortium utilizes three dynamic models based on rate equations for the actively and passively modelocked LDs as well as superradiance. The key parameters of these models and their values defined from the modal gain spectroscopy measurements are indicated in the table below. These parameters are used in WP3 for numerical simulations supporting the final design. Note that TUB device parameters are not included since small differential gain.

Parameter	Symbol	A1902 (1-st run)	A2109 (2-d run)
QW width	d_{QW}	3 nm	4.35 nm
Number of QWs	N_{QW}	2	2
Carrier injection efficiency	η_{QW}	45%	70%
Group refractive index $v_g = c / n_g$	n_g	3.5	3.5
Waveguide width	w	2 μm	1.5 μm
Optical confinement	Γ	0.02	0.03
Carrier density at transparency (3D) Sheet carrier density	n_t	(1.6÷2.2)x10^{19} cm^{-3} (4.8÷6.6)x10^{12} cm^{-2}	3.3x10^{19} cm^{-3} 14.4x10^{12} cm^{-2}
Carrier lifetime in the gain section	τ_n	0.9-1 ns	2.1 ns
Carrier dephasing time Gain bandwidth	T_2 $\Delta\omega_g \approx 4\pi / T_2$	100fs 70-100 meV	100fs 70-100 meV
Differential material gain	$g_0=\partial g/\partial n$	1.2x10^{-6} cm^3/s 2 cm^2/s	0.5x10^{-6} cm^3/s 0.6 cm^2/s
Carrier lifetime in absorber	Ta	450 ps	450 ps
Diff. absorption to diff. gain ratio	$\sigma=(\partial a/\partial n)/(\partial g/\partial n)$	3.0	2.9
Range of normalized absorber biasing parameter	V_a	- 1 to 0.7	-0.4 to 0.8
Internal loss	α_i	35/cm	22/cm
Gain compression	ξ	1.5x10^{-17} cm^3 (strong compression)	1.4x10^{-17} cm^3 (strong compression)

Table 3.6. Parameters of samples A1902 and A2109 for use in numerical simulations of the final design.

Here, the group velocity and carrier lifetime in gain sections was measured in [RD-5]. The carrier lifetime τ is measured from the delay of the output lasing pulse in the gain switching regime with ultra-short excitation current pulses of 500 ps [RD-5]. The carrier injection efficiency η_{QW} is defined from the slop of L-I curves. Other parameters were defined using the following expressions:

$J_{t\_meas} = \eta_{QW} \frac{n_t}{\tau} e_q N_{QW} d_{QW}$ for the transparency current density;

$\partial G / \partial J_{meas} = \eta_{QW} \Gamma \frac{g_0 \tau_n}{v_g e_q N_{QW} d_{QW}}$ for the differential modal gain measured in § 3.2.1

$\alpha_{\mathrm{mod}} = \frac{g_0 n_t (1 - V_a)}{v_g} \sigma\Gamma$ for saturated modal absorption measured in § 3.2.5.

In this expressions, σ is the ratio of the differential absorption to differential gain g_0, Γ is he optical mode confinement factor ($\Gamma = 0.02$). V_a is the normalized absorber biasing parameter. It is related to the biasing voltage U_a at absorber section by $V_a = \frac{v_g}{\sigma g_0 n_t N_{QW} d_{QW}} \frac{U_a}{U_0}$ with U_0 being the characteristic potential of absorber, so as the inverse coefficient $a = 1/U_0$ defines the steepness of absorber tuning curve.

3.6 Conclusion with respect to project objectives of WP2 in phase 2

A large number of gain measurements using the Hakki-Paoli method were provided to the project partners. In the second project phase laser diodes both from EPFL and TUBerlin have been characterized by gain spectroscopy. One aspect was to provide feedback regarding basic laser parameters. Lasers from EPFL and TUBerlin showed high injection efficiency and moderate internal losses. A significantly lower differential gain was identified for laser diodes from TUBerlin which has to be verified.

The second aspect of the gain measurements was to provide laser parameters as input for the simulations regarding short pulse operation. The list of parameters was updated with respect to the new laser structures. This results in the list of dynamic model parameters for multisection InGaN/GaN QW LDs (section 3.5).

Absorption in the absorber sections was measured for the new structures from EPFL. The behaviour of absorption in InGaN/GaN laser diodes turned out to be significantly different from that observed in GaAs or InP baser laser diodes. Therefore these measurements are crucial to understand short pulse operation and define the correct bias on the absorber section.

In the second phase of the project, a method to measure charge carrier life time in the absorber section was established (see sect. 3.3). This method allows to determine carrier lifetime at reverse bias. This dataset is again extremely valuable for the understanding of the dynamical behaviour of InGaN/GaN QW laser diodes.

From relaxation oscillations we determined differential gain as function of carrier density dg/dN and gain compression. One has to keep in mind that Hakki-Paoli gain spectra provide differential gain with respect to current density, dg/dj. Combining dg/dN, dg/dj, and carrier lifetime allows to develop a precise understanding of the carrier dynamics in the gain section. Gain suppression is again crucial to understand ultrafast pulse operation.

With respect to phase 1 we largely expanded our knowledge of laser dynamics. Of particular importance is that we are able to distinguish between carrier dynamics in gain and absorber

sections. Both are operated at different bias voltages, resulting in a different internal field and band structure and consequently different carrier lifetimes in gain and absorber section.

Furthermore, micro-photoluminescence characterization and macroscopic photoluminescence mapping of full wafers were performed on a routine basis to assess the quality of epitaxy.

All parameters have been updated for the actual laser structures of phase 2.

We thus conclude that activities of the WP2 have reached their objectives previewed for phase 2 of the project.

4. Modeling and design of multisection InGaN/GaN QW lasers (WP3)

This section overview progress on modelling in WP3. Below we provide results on :

- Model parameters
- Impact of QW width
- Tunnelling time
- Analytic model and results for superradiance
- Comparative simulations for passive modelocking
- Comparative simulations for active modelocking

The models for optical bistability and map of dynamic regime ahaev been used to interpret experimental data. They are reported in section 6 along side with experimental results.

4.1 Model parameters for multisection InGaN/GaN QW LDs

The consortium utilizes three dynamic models based on rate equations for the actively and passively modelocked LDs as well as Dicke superradiance.

The model parameters have been established for tested samples from two growth runs (MS-LD of samples A1902 and A2109). The are shown in Table 3.6 of previous section of this report. These parameters have been used in model simulations.

Both samples have an active region with 2 QWs. The samples differ by the width of the QWs, which impact the gain and carrier lifetime, and by the p- doping, which impacts the voltage drop. In what follows, it is important to note that the material loss in A2109 are smaller and the gain section carrier lifetime is longer as compare to A1902.

4.2 Impact of InGaN/GaN QW width on the modal gain, absorption and carrier lifetime

The most important parameters that affect the dynamics of multisection laser are

- Differential gain;
- Ratio σ of the differential loss *da/dn* in absorber to the differential gain *dg/dn* of in the amplifier section;
- Ratio of the carrier lifetime in the absorber to the carrier lifetime of the gain.

It is preferably for the generation of shorter pulses to have large differential gain, large differential absorption to gain ratio and small absorber recovery time as compared to the carrier lifetime in the gain section. These conditions ensure the generation of stable mode-locked pulses and are expected to provide most favourable conditions to generate SR pulses.

The objectives of the project and results of experimental tests on multisection lasers have shown a necessity to optimize the QW composition so as to fit the above requirements. In parallel to the growth activities of QW of different width, theoretical analysis has been conducted in order to define the optimal QW width.

Our modeling of material gain and absorption in InGaN/GaN QW laser heterostructures is based on results reported in Ref [Bastard-91]. The model accounts for (see detailed description of the model in [RD-5]) :

- Excitonic absorption (2D excitons)
- Exchange interactions
- Inhomogeneous broadening due to variation of the QW width
- Quantum Confined Stark Effect (QCSE)
- Impact of the internal piezoelectric field and external biasing filed on wavefunction overlap
- The interplay of gain and absorption in setting up the lasing wavelength and the absorber tuning curve
- Impact of the saturation level of absorber

In InGaN/GaN QWs, the reduced exciton mass to free electron mass ratio $\frac{1}{m_0}\frac{m_e m_h}{m_e + m_h} \sim 0.15$ is by a factor of 3 larger then in GaAs/AlGaAs QWs and the Kane's energy parameter (20eV) is comparable to the one of GaAs (28.8eV [Piprek-03]). However, the gain and absorption are significantly lower due to QCSE of internal piezoelectric field, which pulls electrons and holes out of each other, yielding a reduced envelop wavefunction overlap $\left|\langle F_{c1} | F_{hh1} \rangle\right|^2$. The figure 4.1 below shows the wavefunction overlap $\left|\langle F_{c1} | F_{hh1} \rangle\right|^2$ in a QW of 2, 3 and 4 nm width as a function of external negative bias.

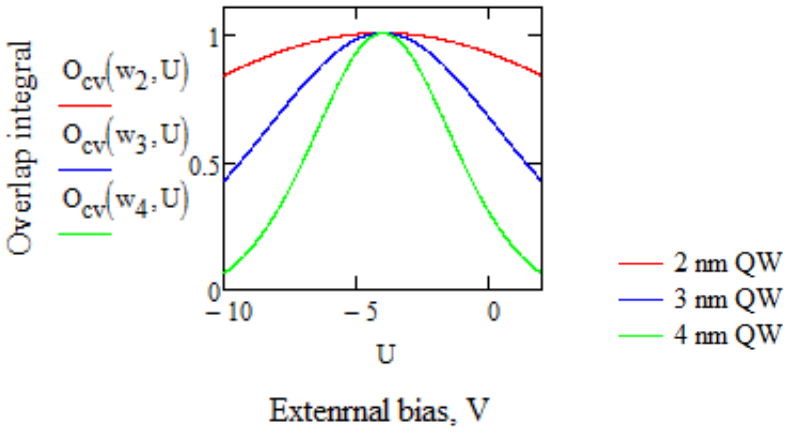

Fig. 4.1. Wavefunction overlap $\left|\langle F_{c1} | F_{hh1} \rangle\right|^2$ in a QW of 2, 3 and 4 nm width in fiction of negative bias.

For the optical gain calculations, the wavefunction overlap $\left|\left\langle F_{c1} \middle| F_{hh1} \right\rangle\right|^2$ at zero bias has to be used. It can be seen that, the optical gain in wide InGaN/GaN QWs is significantly degraded because of the small wavefunction overlap. The internal piezoelectric field in InGaN/GaN QWs is responsible for reduced modal gain and absorption as compare to their conventional III-V counterparts. Thus in opposite to that, GaAs/AlGaAs QWs can be made wider yielding higher optical confinement factor.

Fig 4.2 shows the calculated modal gain spectrum (solid curves) as well as modal absorption for unsaturated (dashed curves) and strongly saturated (doted curves) absorber. The gain curves are plotted at threshold conditions. The modal gain is calculated at the lasing threshold conditions in cavities with absorber of relative length 0%, 15% and 30% of the overall cavity. The set of spectra for unsaturated ($\Delta\mu << 0$) and strongly saturated absorber ($\Delta\mu = -70meV$) are calculated for external bias voltage of -4V (flat band conditions), -6V and -8V. The higher the absorber length, the higher the modal gain at threshold and the lasing wavelength is blue shifted.

Using these considerations, we examine the peak modal gain in function of the carrier density and in this way, we estimate the differential gain and the transparency carrier density. The results are summarized in Table 4.1 in function of the QW width. Fig. 4.3(a) shows the calculated differential gain. The ***differential optical gain decreases with the QW width***. The model prediction in agreement with the experimental measurements summarized in Table 3.6. Because of the reducing wavefunction overlap with the QW width, we find that there is a maximum width of the QW, at which the optical gain can be obtained. According to the model predictions, there will be no gain in QW of 5 nm width and higher.

Although the differential gain variations are in the reasonable quantitative agreement with experimental results, the samples A2109 with wider QW have revealed lower threshold as compared to narrower QW (A1902). In fact we find explanation of this paradox in Ref [Chow-99] (see Fig. 4.3(b)). Based on microscopic modelling utilizing semiconductor Bloch equations, it has bene shown that the carrier lifetime is increases with the QW width. As such the contribution of the spontaneous decay loss by electron-hole recombination process is reduced in wider QWs. Note that increase in the carrier lifetime in wider QW is in agreement with our calculations for the reduced wavefunction overlap in Fig. 4.1.

Figure 4.1 shows calculated threshold modal gain in cavities with different length of absorber. Longer absorber causes blue shift of the lasing mode. From the modal absorption curves plotted in Figure 4.1 it follows that the modal absorption is highly dependent on the relative position of the lasing mode at the tail of absorption. If the lasing mode approaches the tail of the excitonic contribution, the differential absorption will also be a function of the saturation level of absorber.

As can be seen, our model takes excitonic contribution into account. To justify this feature, we bring the following considerations. The excitonic contribution to the absorption has been observed in some samples of GaAs/AlGaAs QWs at room temperature conditions [Chemla-85]. The binding energy of InGaN/GaN QW excitons exceeds the one in GaAs/AlGaAs QWs [Christopoulos-07]. Therefore, one should expect that the excitonic peak at the lower-energy tail of the absorption spectrum should be well pronounced in unsaturated InGaN/GaN QW absorber as well. This has been carefully taken into account in our analysis of the gain and absorption interplay, in establishing the lasing wavelength.

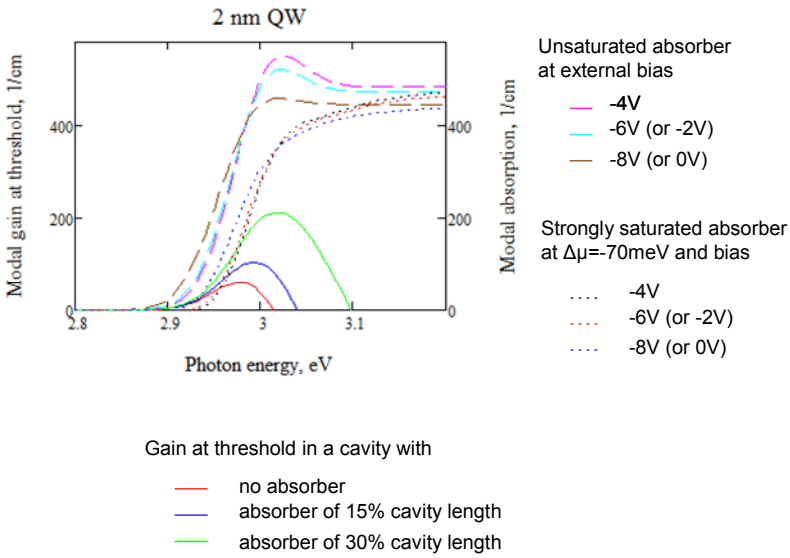

Fig. 4.2. Modal gain spectrum (solid curves), absorption spectra of unsaturated (dashed curves) and strongly saturated absorber (doted curves).

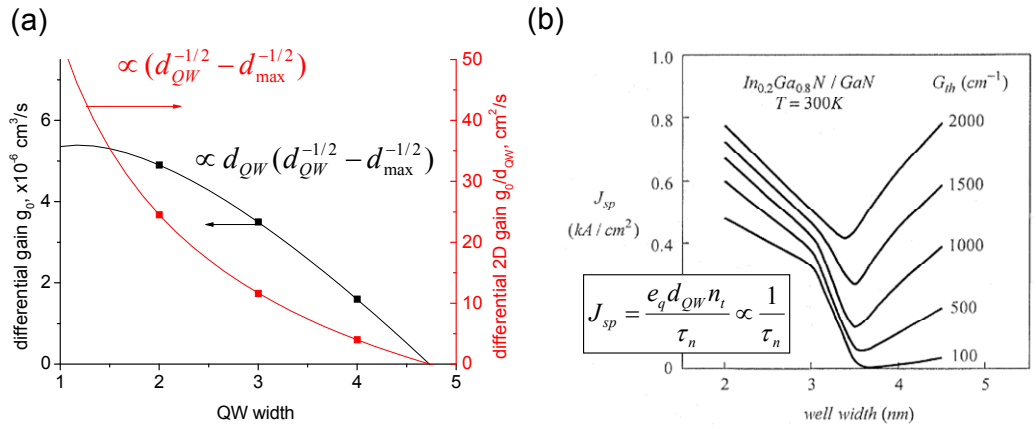

Fig. 4.3. (a) Calculated differential gain in function of the QW width. The left axis shows values normalized on 3D carrier density. Right axis shows the differential gain with respect to 2D carrier sheet density. (b) Reproduced from [Chow-99]: threshold current contribution from spontaneous decay calculated from microscopic Bloch equations.

Parameter	Symbol	2 nm QW	3nm QW	4nm QW
QW width	d_{QW}	2 nm	3 nm	4 nm
Number of QWs	N_{QW}	1	1	1
Carrier injection efficiency (based on exp. data)	η_{QW}~1/ dQW	35%	45%	70%
Group refractive index	n_g	3.5	3.5	3.5
Optical confinement	$\Gamma \propto N_{QW} d_{QW}$	0.013	0.02	0.026
Carrier density at transparency: 3D 2D	$n_t \propto 1/d_{QW}$	1.2×10^{19} cm^{-3} 2.4×10^{12} cm^{-2}	0.8×10^{19} cm^{-3} 2.4×10^{12} cm^{-2}	0.6×10^{19} cm^{-3} 2.4×10^{12} cm^{-2}
Differential material gain 3D 2D	$g_0=\partial G/\partial n$ $\propto d_{QW}$ ($1/\sqrt{d_{QW}}$—$1/\sqrt{d_{max}}$) g_0/d_{QW}= ($1/\sqrt{d_{QW}}$—$1/\sqrt{d_{max}}$)	4.9×10^{-6} cm^3/s 24.5 cm^2/s	3.5×10^{-6} cm^3/s 11.6 cm^2/s	1.6×10^{-6} cm^3/s 4 cm^2/s
Short absorber section , 0V				
Differential material absorption	$g_0=\partial A/\partial n$	19.3×10^{-6} cm^3/s	10.7×10^{-6} cm^3/s	3.2×10^{-6} cm^3/s
Diff. absorption to diff. gain ratio	$\sigma=(\partial a/\partial n)/(\partial g/\partial n)$	3.9	3.1	2
Long absorber section, 0V				
Differential material absorption	$g_0=\partial A/\partial n$	13.8×10^{-6} cm^3/s	11.4×10^{-6} cm^3/s	8×10^{-6} cm^3/s
Diff. absorption to diff. gain ratio	$\sigma=(\partial a/\partial n)/(\partial g/\partial n)$	2.8	3.3	5.0

Table 4.1. Calculated modal gain and absorption parameters in QWs of 2, 3 and 4 nm width

Fig 4.4 shows calculated lasing mode and modal absorption v.s. negative absorber bias (absorber tuning curve). The numerical simulations are conducted for unsaturated and strongly saturated absorber for cavities with relative absorber length of 0%, 10%, 20% and 30%. We conclude that absorber length and its saturation level impact significantly the lasing wavelength and, hence, the shape of the effective tuning curve of absorber.

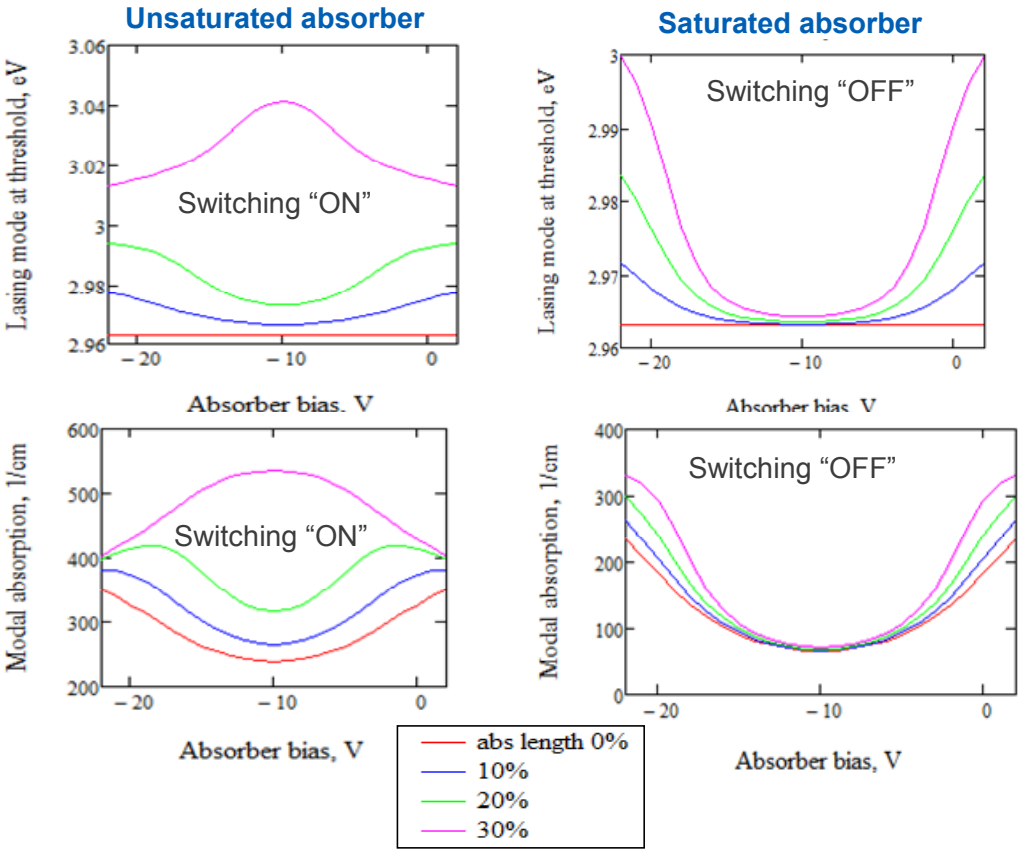

Fig. 4.4. Calculated photon energy for the lasing mode at threshold (top panels) and the absorber tuning curve (bottom panels) in function of the negative absorber bias. Left panels shows the curves plotted for unsaturated absorber, corresponding to the switching On threshold of the optical bistability domain. The right panels shows the lasing wavelength and modal absorption for highly saturated absorber. This can be regarded as the one for the switching off threshold of the optical bistability domain.

An increase of the absorber length shifts the lasing wavelength in the region of higher modal absorption, which is an important feature in the context of the conclusions made upon the outcomes of dynamical tests reported in Sec. 6. However this also indicates that the differential absorption measurements of Sec. 3, are impacted by the short length of absorber. Therefore, for the third period of the project it would be important to fabricate samples with different length of absorber, varying up to 40%.

As predicted by the model, the excitonic absorption can be observed in cavities with long absorber at low saturation of absorber. The excitonic contribution to the absorption results in abnormal tuning curve of absorber revealing a maximum at the flat band conditions and the blue shift of the lasing mode. The excitonic peak is suppressed in strongly saturated absorber.

Detailed simulations of the absorption in function of the saturation level of the absorber have been conducted. The saturated modal absorption coefficient versus carrier density in absorber QW is plotted in Fig. 4.5.

Figure 4.5 (a) shows the modal absorption at the wavelength of the *modal gain* peak in a cavity with a short absorber (or no absorber). These correspond to conditions of the absorption measurements in Sec. 3. The differential absorption [the slop of the curves in Fig. 4.5(a)] is

independent of the absorber bias, indicating that differential absorption coefficient cannot be deduced from the experimental data of Sec 3. As such, modelling in Sec. 5 utilizes differential absorption to differential gain ratio σ predicted by the theory (in the range from 2.5 to 3.5, see table 3.6). The absorber bias alters the value of non-saturated absorption at vanishing carrier density.

Fig. 4.5(b) exposes the impact of the absorber length on differential absorption. The modal absorption coefficient is calculated at the lasing wavelength (at the peak wavelength of the *net gain*). Longer absorber section increases the lasing threshold, causing operation at a higher carrier density in the gain section. The lasing mode shifts to higher photon energies due to the band filling effect. In this region, the slope of the absorption tail is steeper (the differential absorption is higher). This mechanism allows one to reach higher values of differential absorption coefficient.

Fig.4.6 shows calculated differential absorption in function of the QW width. The calculations are performed for the short and long absorber sections at two extreme levels of saturation. As the differential gain, the ***differential absorption decreases with the QW width***.

The results of simulations are summarized in Table 4.1. They indicate that narrow QWs (2-3 nm width) will provide higher differential gain and absorptions and thus are most suitable for sub-picosecond pulse generation in mode-locking or superradiance regimes.

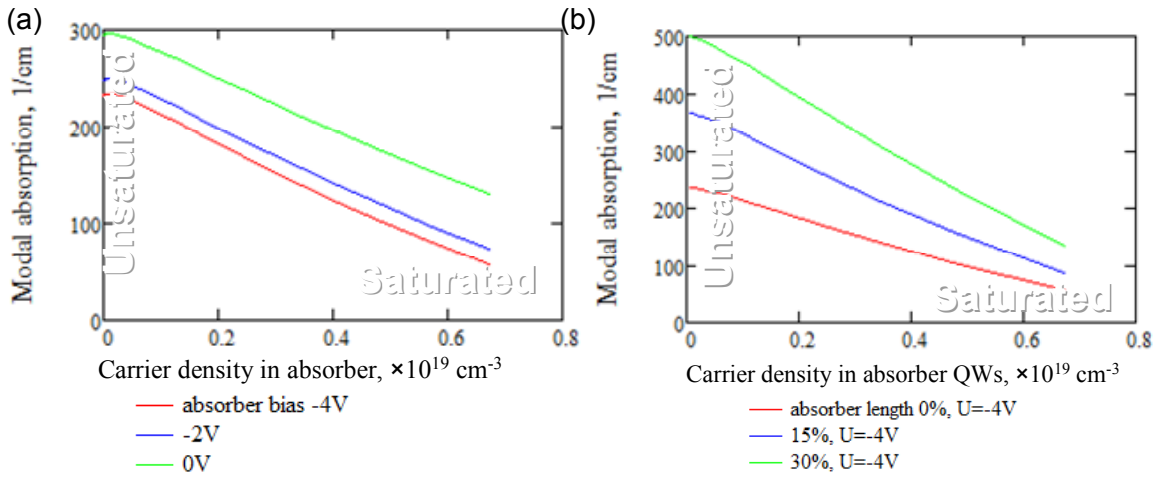

Fig. 4.5. Saturated modal absorption in function of the carrier density: (a) at the lasing wavelength in the cavity with relatively small absorber and absorber bias -4V (flat band conditions), -2V and 0 V; (b) at the lasing wavelength in a cavity with relative absorber length 0%, 15% and 30 % and absorber bias -4V (flat band conditions).

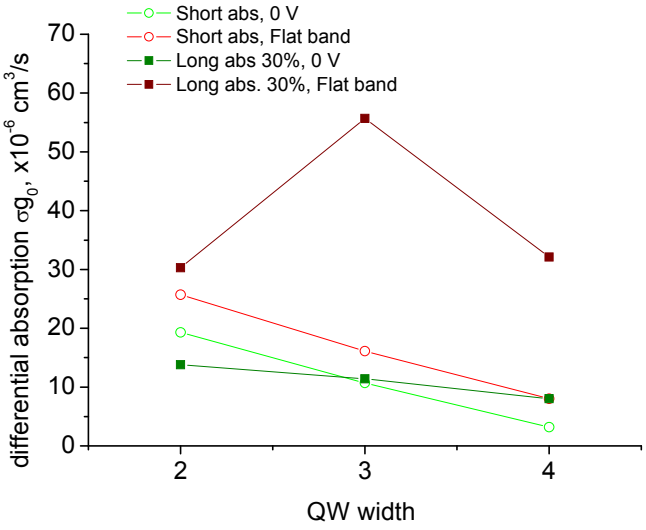

Fig. 4.6. Calculated differential absorption coefficient in function of the QW width aturated modal absorption in function of the carrier density: (a) at the lasing wavelength in the cavity with relatively small absorber and absorber bias -4V (flat band conditions), -2V and 0 V; (b) at the lasing wavelength in a cavity with relative absorber length 0%, 15% and 30 % and absorber bias -4V (flat band conditions).

4.3 Modelling of the tunnelling time in InGaN/GaN QW absorber

The band structure for this study has been calculated by using SiLENSe software package.The characteristic time for tunneling of an electron from the quantum well into the almost free (unbounded) state has been estimated as

$$\tau_{tun} = \tau_p W \,, \tag{4.1}$$

Here τ_p is the characteristic time of electron oscillation in the well (i.e., the characteristic collision time with the wall). The inverse quasi-classical probability of tunneling can be found as

$$W = \exp(2I), \qquad I = \int_{z_1}^{z_2} \left\{ \frac{2m}{\hbar^2}(U-E) \right\}^{1/2} dz \,, \tag{4.2}$$

U(*z*) is the barrier potential, integration is between the turning points of the tunneling process.

Below are the results of our estimates for two EPFL structures, namely, a) A1902, the width of the quantum well $d = 3nm$, and b) A2109, the width of the quantum well $d = 4.5nm$, configurations with and without spacer has been considered. Calculations are based on the data for the conduction bands of these structures, which has been simulated with SiLENSe package

a) EPFL A1902 structure

Configuration of the conduction band in the region of the quantum wells is shown in the Fig. 4.7.

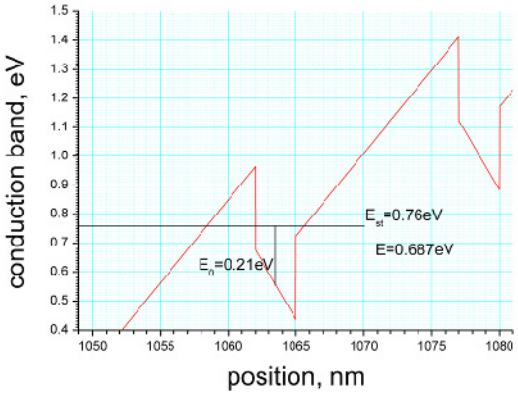

Fig.4.7. Conduction band structure and the electron energy levels for A1902 structure, bias voltage is -2V.

The electron energy level has been calculated in two different ways, using a) the triangle well approximation (which in the Figure 4.7 corresponds to the level E=0.687eV), and b) the rectangular well approximation (which is characterized by the lowest energy level $E_0 \approx 0.210eV$), the tilt in the quantum well potential has been taken into account through the Stark shift, the correspondent energy level in the case of bias voltage -2V is found to be $E_{st} \approx 0.76eV$. The characteristic time $\tau_{p1} \sim \frac{\pi\hbar}{E_0} \sim 10f\,\mathrm{sec}$ and coincides with the estimate $\tau_{p2} = \frac{2mc^2d^2}{\pi\hbar c^2} \approx 10f\,\mathrm{sec}$. Thus, the characteristic relaxation time due to the tunneling at the bias voltage of -2V is approximately 20psec (triangle well approximation) and 1.4psec (rectangular well approximation). Tunneling time is rapidly decreasing with the bias voltage up to dozen of femtoseconds.

The tunneling time is plotted in the Fig. 4.8 below, the red circles correspond to the triangle well approximation and the blue squares – to the rectangular well approximation with the Stark shift of the energy.

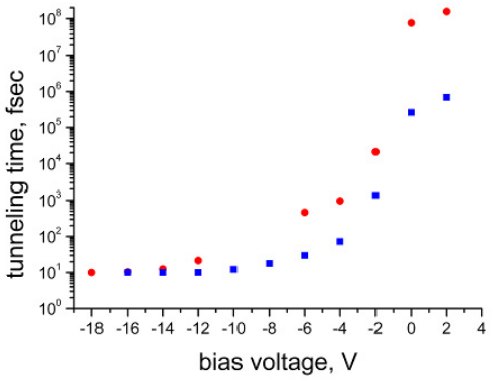

Fig.4.8. The tunneling relaxation time for the EPFL structure A1902.

b) EPFL A 2109 structure with and without spacer.

The estimates of the tunneling probability have been done for the two data sets of the conduction band energy, with and without a spacer.

The conduction band along with the electron energy levels at the bias voltage -2V are shown in Figs. 4.9 and 4.10 for the structures without spacer and with spacer, respectively.

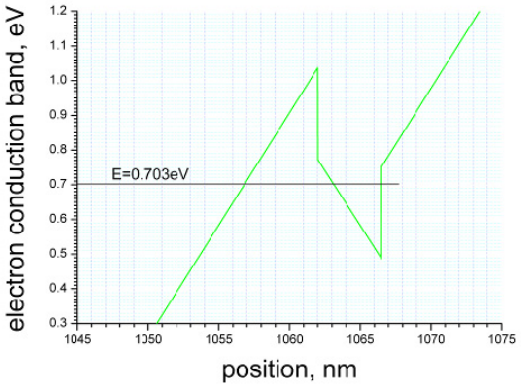

Fig. 4.9. Conduction band of the structure A2109 without spacer, the energy level in both the approximations (triangle well and rectangular well Stark shift) practically coincide E=0.703eV, the bias voltage is -2V

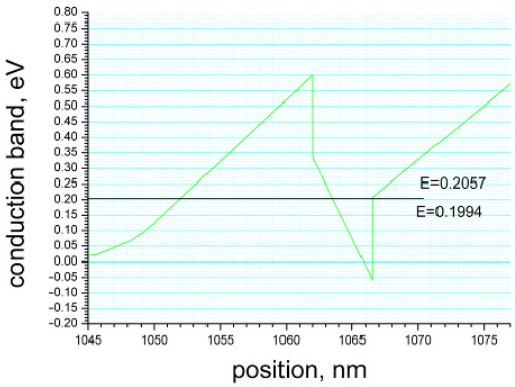

Fig. 4.10. Conduction band of the structure A2109 with spacer, the energy level in both the approximations (triangle well and rectangular well & Stark shift) practically coincide E=0.206eV and E=0.1994eV, the bias voltage is -2V.

One can find from the Figs.4.9 and 4.10 that in the configuration with the spacer, the energy level is lower and the tunneling potential is wider than in the configuration without spacer. Thus, the correspondent tunneling time turns out to be shorter in the cases without spacer. In the configuration without spacer, the tunneling time at the bias voltage -2V is approximately 0.4nsec ($\tau_{p1} = \hbar\pi / E_e \approx 20 f\,\mathrm{sec}$, $\tau_{p2} = \frac{2mc^2 d^2}{\pi\hbar c^2} \approx 20 f\,\mathrm{sec}$) and rapidly decreasing with the bias voltage.

The results of our estimates for the tunneling time are shown in the Fig. 4.11 below, in which the red circles corresponds to the configuration with spacer, and black squares correspond to

the configuration without spacer. Doubled points at given bias values correspond to values found in different energy level (triangle well and rectangular well) approximations.

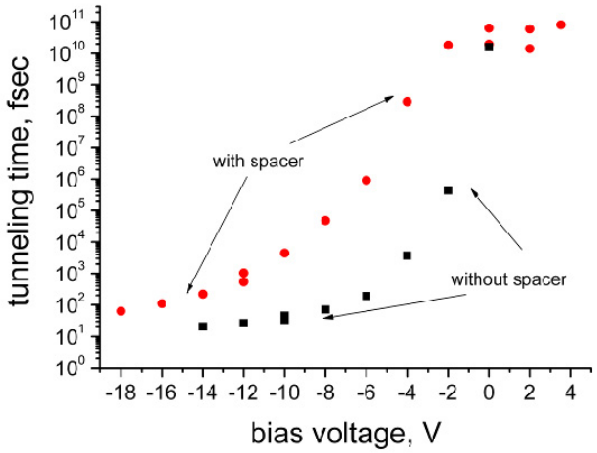

Fig. 4.11. The tunneling relaxation time for the EPFL structure A2109 with and without spacer.

In conclusion, our estimates of the tunneling time have shown that this value being of the order of half nanosecond (A2109 without spacer) and few dozen of picoseconds (A1902) at the bias voltage -2V rapidly decreases with the bias voltage up to few dozen of femtoseconds at voltages below -12V -14V when the potential barrier practically disappear.

An increase in the tunneling time, which is found in the experiment, can be related to the presence of a large amount of electrons in the region near the quantum well barrier, so that the all the quantum states will be filled out and the tunneling of electron from the state inside the quantum well will be condemned. To describe this one should 1) use the kinetic approach and 2) find out the source/origin of that large amount of electrons.

4.4 Superradiant source

4.4.1 Analytic model for superradiance

CSEM' numerical spatio-temporal model for Dicke superradiance regime established in the first period of the project is based on numerical solver of semi-classical Maxwell-Bloch equations [RD-5]. It requires substantial amount of computer time to accomplish the cavity optimization task. The triggering of superradiance is a stochastic process, for which the numerical model incorporates the Langevin noise terms. As such, predicted pulse parameters show large variations between individual realisations. This feature, on one side reproduces the experimental conditions. However on another side such variations may put out of sight the real trends in the output pulse parameters. In order to overcome these difficulties, a pure analytical model has been developed for spontaneous build up of superradiance in semiconductors.

A spontaneous build-up of macroscopic coherences in solids, or in other words, a phase transition to a single macroscopic quantum state of matter, has always been a fascinating subject for scientific and engineering communities. The superradiance (SR) in semiconductor

edge emitters can be considered as an example of spontaneous macroscopic coherences in solids.

A hypothesis has been drawn that in semiconductors, the SR is assisted by formation of a transient coupled electron-hole (e-h) pair state mediated by photons, much like as phonon mediation in a superconducting BCS (Bardeen, Cooper, and Schrieffer) state [Vasil'ev-01]. According to that, the e-h system undergoes the second order non-equilibrium phase transition when the coherent BSC-like state of e-h pairs is building up during SR pulse emission.

An attempt of rigorous treatment of SR as a spontaneous build up of macroscopic quantum state is undertaken. We show that SR can be considered as condensation of lower polaritons in a trap if the coordinate system is chosen so as to be co-propagating with the optical constituent of polaritons (optical pulse in the cavity). A master equation, which has the form of Ginzburg-Landau or Gross–Pitaevskii equations, has been obtained for SR emission. Its two solutions allowed us to predict two different regimes of SR emission in an edge-emitting semiconductor cavity.

As model system, the longitudinal polaritons in an edge emitting cavity with InGaN/GaN QWs are considered here (Fig .4.12a). We focus on features related to 1D dispersion (and condensation) of such longitudinal polaritons, while two other degrees of freedom has minor impact on the results reported here. The band anticrossing occurs at photon energy corresponding to the interband transition energy. James –Cuming model predicts a gap of ~5 meV for the typical SR pulse parameter (see the inset in Fig.4.12a). The group velocity $\partial E/\partial \hbar k$ of UP and LP at the band anticrossing is exactly $v_g/2$, a half of the cavity mode group velocity, indicating that polaritons are half matter – half light composite bosons. Fig. 4.12b) shows the band anticrossing features in the coordinate system co-propagating with UP and LP at $v_g/2$ velocity. The relativistic correction at such coordinate transform is negligible ($1/\sqrt{1-(v_g/2c)^2} \sim 1.01$ for GaN) and UP′ (LP′) energies are obtained from transformation $E' = E - \frac{1}{2}\hbar k v_g$. The band edge of LP′ with negative effective mass represents a trap. The effective mass of polaritons $|m^*| = (\partial^2 E/\hbar^2 \partial k^2)^{-1}$ ~$10^{-11} m_e$ assumes possibility of room temperature condensation, during SR pulse emission. The thermal de Broglie wavelength criteria for macroscopic quantum degeneracy predicts very low critical densities, indicating that, thermodynamic considerations does not provide main limiting factor for LP′ condensation and SR pulse emission.

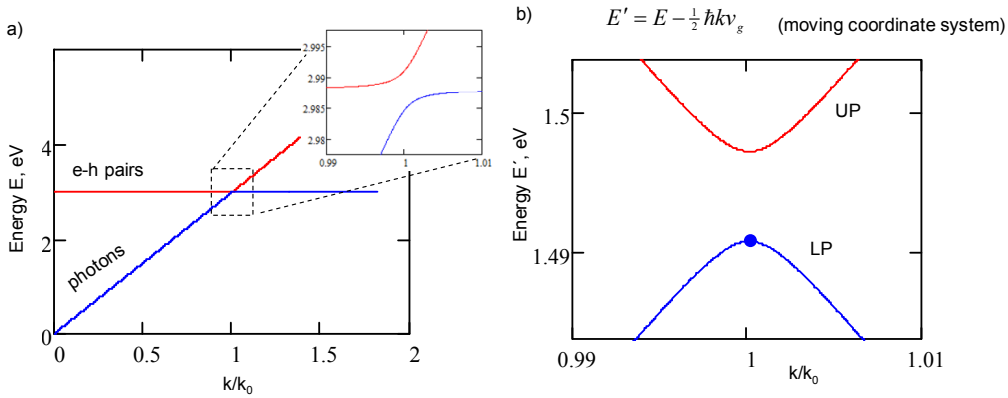

Fig. 4.12. a) Energies of longitudinal 1D polaritons. The inset shows the band anticrossing at the band slope of $v_g/2$. b) Same energy diagram in the moving at $v_g/2$ coordinate system. The dot indicates the LP′ polariton trap

An analysis of semi-classical Maxwell-Bloch equations in the internal coordinate system of the photonic constituent of the SR pulse $\xi = t - z/v_g$ has revealed a possibility to obtain a master equation for SR emission in semiconductors [Boiko-11]

$$\left\{-\frac{\partial^2}{\partial\xi^2}+\frac{\Gamma^2 g_0^2}{v_g^2 T_2^2(\alpha_i+2/L_c)^2}\left((n_0-n_{cr})^2-2P^2\right)\right\}P=0 \qquad (4.3)$$

where macroscopic polarization P is the order parameter, n_0 is the initial carrier density before SR pulse emission, n_{cr} is the critical carrier density, L_c; is the coherence length, Γ is the optical confinement actor, g_0 is the linear gain coefficient, α_i is the material loss coefficient and v_g is the group velocity (see Table 3.6).

This master equation is similar to the of Gross–Pitaevski or Ginzburg-Landau equation (GLE). Its solution can be approximated by the hyperbolic secant function. An analysis shows that in particular case of SR emission, there are two types of cardinally different solutions, distinguished by the ratio between the size of the sample L (cavity length or gain section length) and the size of the condensate fraction domain defined by the coherence length L_c.

In type- I SR regime, $L_c > L$ indicating that fixed phase relationships are established over the entire sample. The peak power reveals a characteristic quadratic growth $S_{peak} \propto (n_0 - n_{cr1})^2$ (Fig. 4.13, red dashed curve) as predicted by Dicke for a gas medium [Dicke-54]. With increasing initial carrier density n_0, the SR pulse width reduces. At the second critical density n_{cr2}, it becomes shorter than the length of the sample. In the type-II SR regime, $L_c < L$, so as only partial coherence is established over the sample, yielding a more gentle dependence $S_{peak} \propto (n_0 - n_{cr2})^{3/2}$ (see Fig.4.13, blue dashed curve). At any moment of time, the condensate fraction domain is smaller than sample. An analysis of the critical carrier densities n_{cr2} and n_{cr2} in function of the sample length indicates that type-I SR might be possible in a narrow region of pump rates provided the cavity is made sufficiently short. In most of the cases, type-II SR will be established.

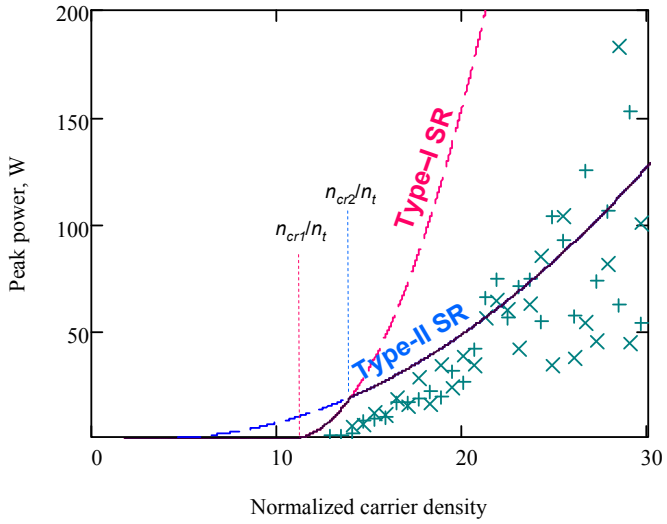

Fig. 4.13. Peak power of SR pulse in 50 um length cavity. Dashed lines show the analytic model predictions for type I and type II regimes, points show prediction of the numerical traveling wave model, "+" and "x" distinguish SR pulses at the two cavity facets

These analytic model predictions have been compared to the numerical solution of the semi-classical Maxwell-Bloch equations in a 50 μm long GaN cavity (Fig. 4.13, points). To reproduce spontaneous build up of SR pulse, the numeric model incorporates noise, which is responsible for stochastic variations of the pulse peak power.

The first critical density for type-I SR regime in such cavity is n_{cr1}~$11n_t$ (n_t is the transparency carrier density). For $n=13n_t$ (the case $n_{cr1}<n_0< n_{cr2}$ in Fig 4.14, top panels), the pulse width is ~5 ps, much longer than the cavity roundtrip time 1.2ps. The SR pulse builds up after 15 cavity roundtrips. The order parameter *P* (macroscopic polarization) reaches the maximum of $2n_t$. The pulse shape well agrees with hyperbolic secant shape used in analytic model.

The second critical density for type-II regime is n_{cr2}~$14n_t$. Fig 4.14 (middle panels) shows the pulse shape and spatio- temporal dynamics of macroscopic polarization build up for the initial carrier density $n_0=20n_t$. The SR pulses are emitted after ~6 cavity roundtrips, when the order parameter *P* reaches a maximum of $8n_t$. The output pulse envelope exhibits oscillations due to reflections of the cavity facets and multiple cavity roundtrips. At each roundtrip, the SR pulse width is ~450 fs.

At higher pump rates ($n_0=28\ n_t$ in Fig 4.14, bottom panels), all stored energy is emitted in a single-shoot SR pulse, just after 2-4 cavity roundtrips and the pulse width reduces further (0.38ps in Fig.4.14). It follows that, type-II SR regime is mostly promising for practical applications, endorsing to use relatively long edge emitting cavities.

Further development of this analytical model consisted in incorporation of the gain compression effects (see Table 3.6 and conclusions in [RD-5-CA]). It appears that in the presence of gain compression, Eq.(4.3) takes the form:

$$-T_2^2\Delta^2\frac{\partial^2 P}{\partial\xi^2}+\left[\eta_0^2-2P^2\right]P=\Theta\left(8\eta_0^2P_+^3-9P_+^5\right)+\frac{8}{3}\Theta\Delta\eta_0^3P+\frac{4}{3}\Theta T_2\Delta^2\left(5P_+^2-2\eta_0^2\right)\frac{\partial P}{\partial\xi} \qquad (4.4)$$

were $\eta_0=n_0-n_{cr}$ is the excess of the initial carrier density above critical density, $\Delta=\frac{v_g(\alpha_i+2/L)}{\Gamma g_0}$ accounts for the cavity loss, and $\Theta=\frac{1}{2}\frac{\xi}{g_0T_2\Delta^2}$ accounts for the gain compression ξ (see Table 4.1). One can recognize the unperturbed master equation (4.3) in the left-hand side of this equitation. Its analytic solution in the presence of the gain compression has been obtained by using perturbation theory.

The dynamics in the presence of gain compression is cardinally different. The pulse width in type –I SR regime is limited by the ratio of the gain compression coefficient to differential gain. $\tau_c^{(I)}\geq\frac{2}{3}\xi/g_0$.

Comparison of analytic and numeric models for the case of gain compression in A1902 and A2109 samples (ξ~10^{-17} cm^3 in Table 3.6) has revealed that approximations used in analytic model are not valid for the case of high gain compression, when $\Theta n_0^2\sim 1$. Therefore the numerical simulations have been performed fro final design.

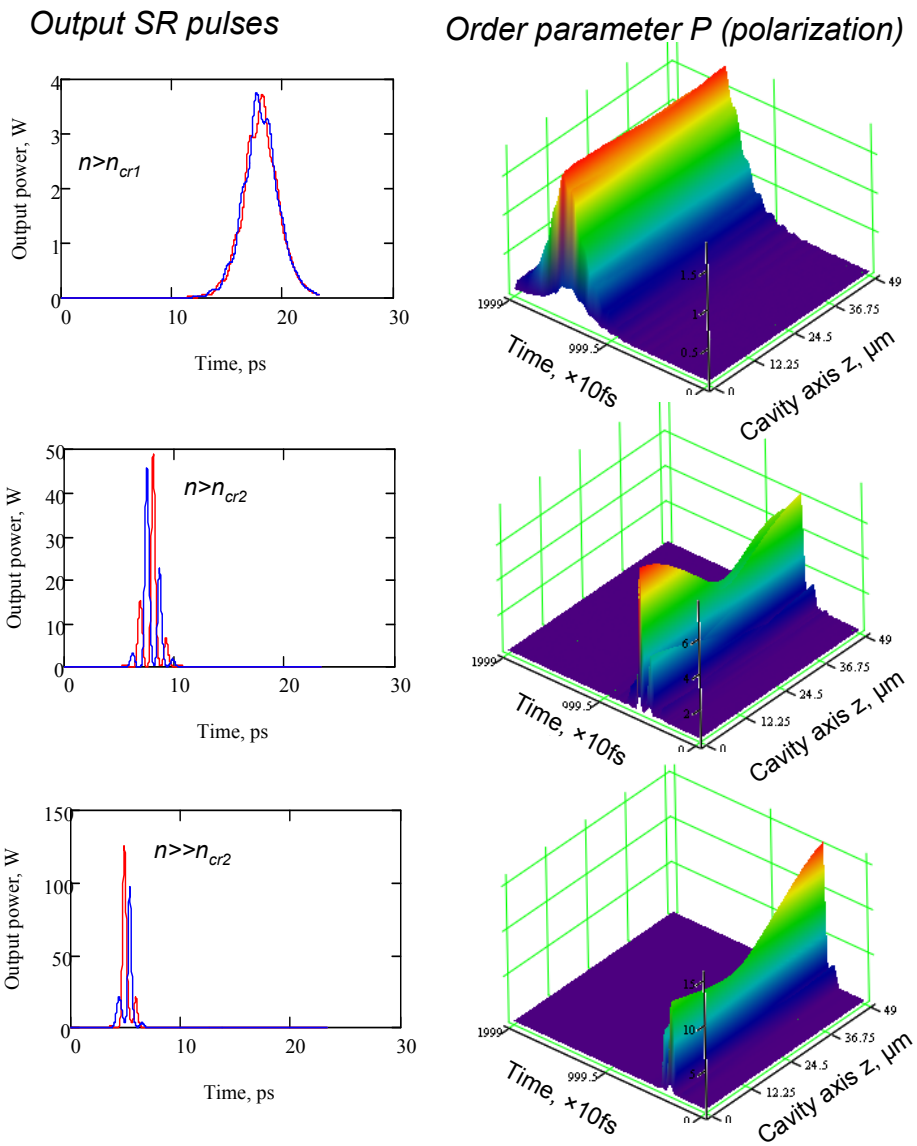

Fig. 4.14. Output SR pulses (left panels, red and blue curves distinguish opposite cavity facets) and spatiotemporal dynamics of macroscopic polarization *P* (right panels) at initial carrier density n_0 of $13n_t$, $20n_t$. and 28 n_t . The pulse width is 5 ps, 450fs and 380fs.

4.4.2 Final design of SR source

This section can be found in Confidential Annex of this deliverable [RD-13].

4.5 Comparative modelling of self-starting mode-locking regime in A1902 and A2109 structures

This section can be found in Confidential Annex of this deliverable [RD-13].

4.6 Modelling of active mode-locking regimes - the importance of absorber lifetime

This section can be found in Confidential Annex of this deliverable [RD-13].

4.6.1 Modelling A2109 devices with absorber lifetimes measured by Femtoblue

This section can be found in Confidential Annex of this deliverable [RD-13].

4.6.2 Modelling with decreased absorber lifetime

This section can be found in Confidential Annex of this deliverable [RD-13].

4.6.3 Modelling devices using A1902

This section can be found in Confidential Annex of this deliverable [RD-13].

4.6.4 Summary

This section can be found in Confidential Annex of this deliverable [RD-13].

4.7 Conclusion with respect to project objectives of WP3 in Phase 2

The objectives of Phase 2 have been reached. The Milestone M3.2 Final design of multisection laser structures is reached de-facto. The milestone confirmation document assigned in DoW is the MoMs of the Final Design Review meeting. It will be issued upon the Review of the Project scheduled for November 2011.

The rest of this section can be found in Confidential Annex of this deliverable [RD-13].

5. Manufacturing of multisection lasers (WP4)

5.1 Development of advanced processing technology

This section can be found in Confidential Annex of this deliverable [RD-13].

5.2 Dedicated high-frequency mounting of ultrafast multisection lasers

The mounting concept of FemtoBlue devices has been elaborated in [RD-5]. The concept enables to address three dynamic regimes (sub-objectives of the project) using same set of mounted devices:

2.1 Study of the active mode-locking regime

2.2. Study of the self-modelocking regime

2.3. Study of the superradiance regime.

It was important to take into account that large voltage drop at the active region of InGaN/GaN LDs and p-doped layers of the structure in combination with high peak current (when operated in Dicke superradiance regime) result in important Joule heat generation. Therefore, as a baseline for mounting ultrafast multisection InGaN/GaN laser diodes we have chosen a proven solution for high power laser diodes. It consists in mounting laser diode chip on a high thermal conductivity submount which is then installed on a metal laser microbench to provide heat sinking and convenient form factor for manipulation on the optical table. The laser submount has separate metal contact pads for wirebonding the p-contacts of the gain and absorber sections as well as for the n contact of the laser structure. The absorber section contact is a 50GHz microstrip line enabling operation of the structure in the active modelocking regime. It has no impact on passive modelocking or superradiance regimes, when a constant bias voltage is applied to the absorber. The mounting concept of FemtoBlue devices is detailed in Fig. 5.5.

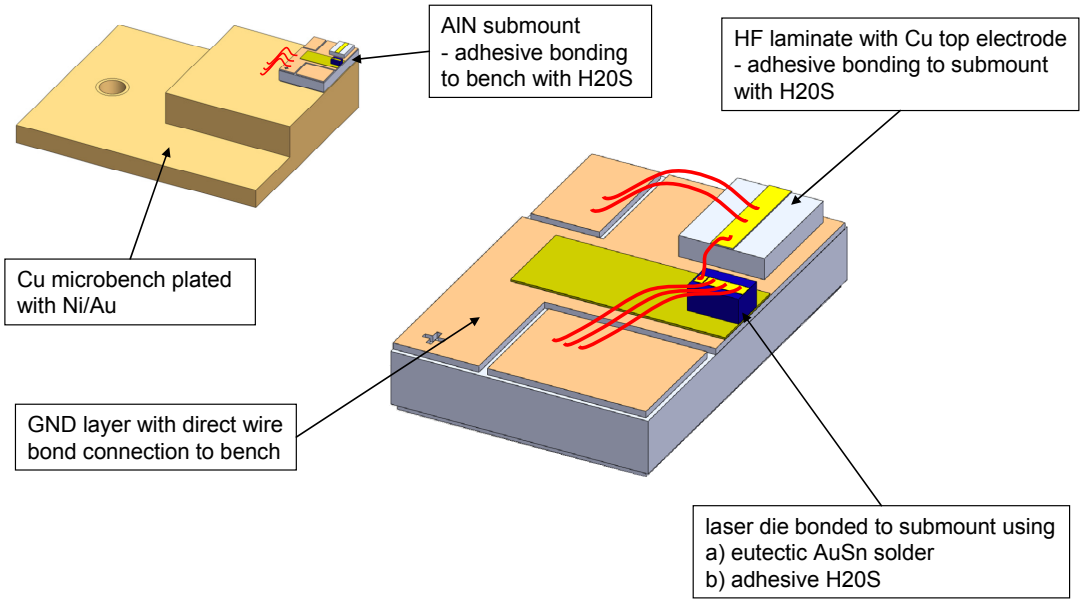

Fig. 5.5. FemtoBlue laser diode assembly showing location of MS-LD, high speed mircrostrip line and wirebonds. MS-LDs of various lengths can be mounted. The laser submount allows a close contact of the microstrip line to the laser with a short wire bond. This maximizes the modulation voltage to the absorber section of the laser.

The MSLD structures were grown and processed (sample A1902). They were cleaved in laser bars comprising 8-10 single section and multisection LDs of different absorber length and different waveguide width.

The bars have been tested and LD showing low threshold currents and reasonable matching to the design requirements [RD-5-CA] have been selected for mounting.

The selected laser bars have been sawn into solitary LDs. The process introduces cracks in the volume of the LDs and creates fractures on the sides of LD chips. Therefore the diced LD chips have been inspected under the microscope and partially tested with the current probes. Optimization of sawing parameters and careful testing of diced laser chips allowed us to increase the yield of this operation. In this way, 66 MS-LD devices have been secured for mounting. Figure 5.6 shows a solitary multisection laser chip under the functional test after the dicing operation.

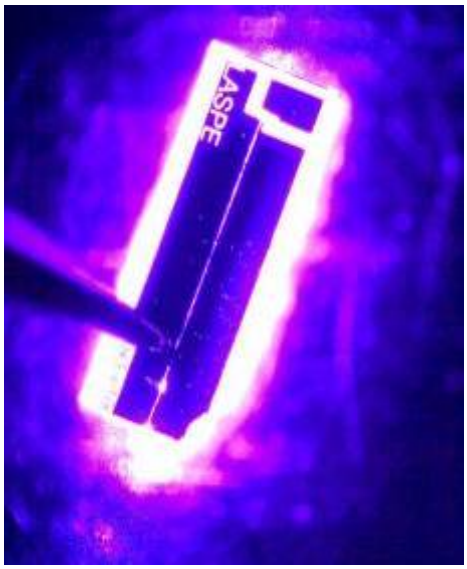

Fig. 5.6. Solitary MS-LD chip under functional tests before mounting

Several tests on laser chip bonding and wire bonding have been conducted. Fig. 5.7 illustrates testing of MS-LD bounded with eutectic Au/Sn solder (325 ^{o}C, 1 min). The measured maximum shear strain sustained by LD chip is by a factor of 1.5 below the expected value, indicating insufficient adhesion of LD chip to submount. Apart from the high risk of detaching of the LD chip during the wirebonding operations (this has been observed in 4 out of 10 cases), this also indicates that the thermal heat sinking resistance might be not as low as expected due to surface roughness of LD chips. Therefore a decision has been taken to bound the major part of the samples with thermally and electrically conductive epoxy H20S (cured at 100 ^{o}C for 2 hours). The parameters of the ball wirebonding to the LD chip were kept at minimum values to reduce the impact on the laser (150 mW, 350 ms, 150 mN).

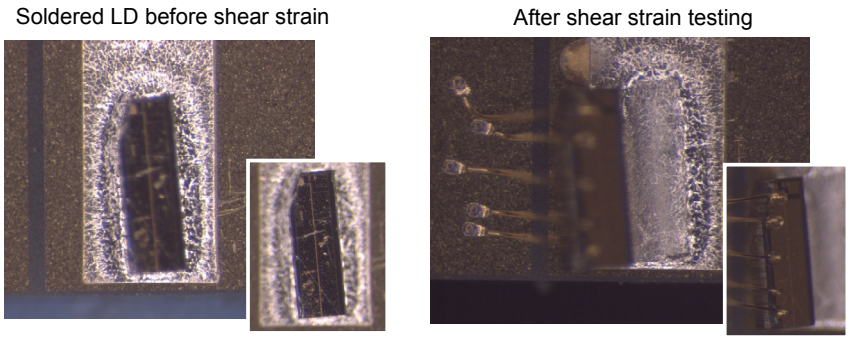

Fig. 5.7. Shear strain test of ML-LD bonded with eutectic Au/Sn solder

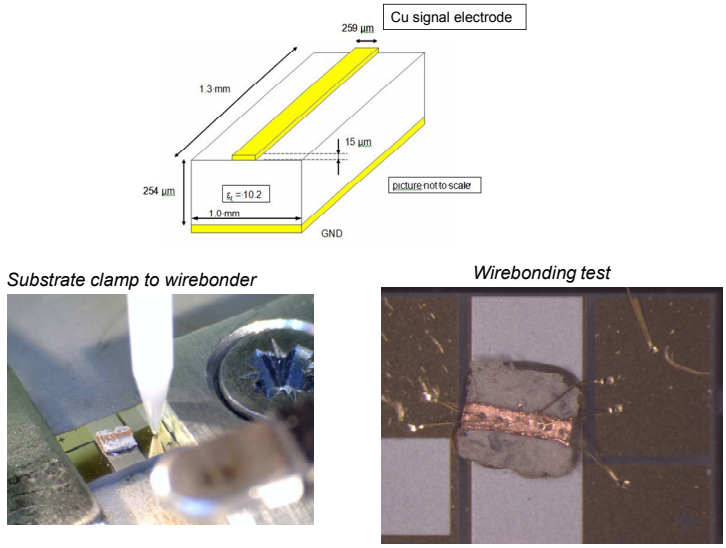

Fig. 5.8. Design of microstrip line (top); bonding and wirebonding tests (bottom)

The design of microstrip line for injecting 50GHz modulation signal in the active modelocking regime has been reported in [RD-5]. 70 samples of microstrip lines have been fabricated. Additional tests on bonding and wirebonding have been conducted validating the use of epoxy H20S for bonding the microstrip line to the laser submount (Fig. 5.8). At the same time, the wirebonding tests have indicated that wirebonding to the Cu strip contact is challenging and demanded from us additional optimization of bonding parameters for the wedge bonding at the microstrip line (500mW, 250ms, 250 mN).

Finally the multisection InGaN/GaN lasers have been assembled following the process flow in Fig. 5.9

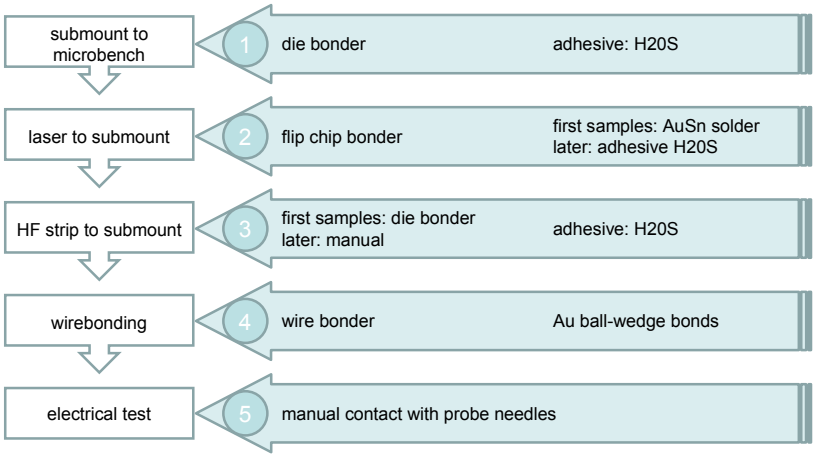

Fig. 5.9. Process flow of FemtoBlue laser mounting

Figure 5.10 shows a photographic image of part of the fabricated Femtoblue devices ready for tests in three dynamic regimes. The photographic images of the devices assembled using eutectic Au/Sn solder or epoxy H20S are also shown.

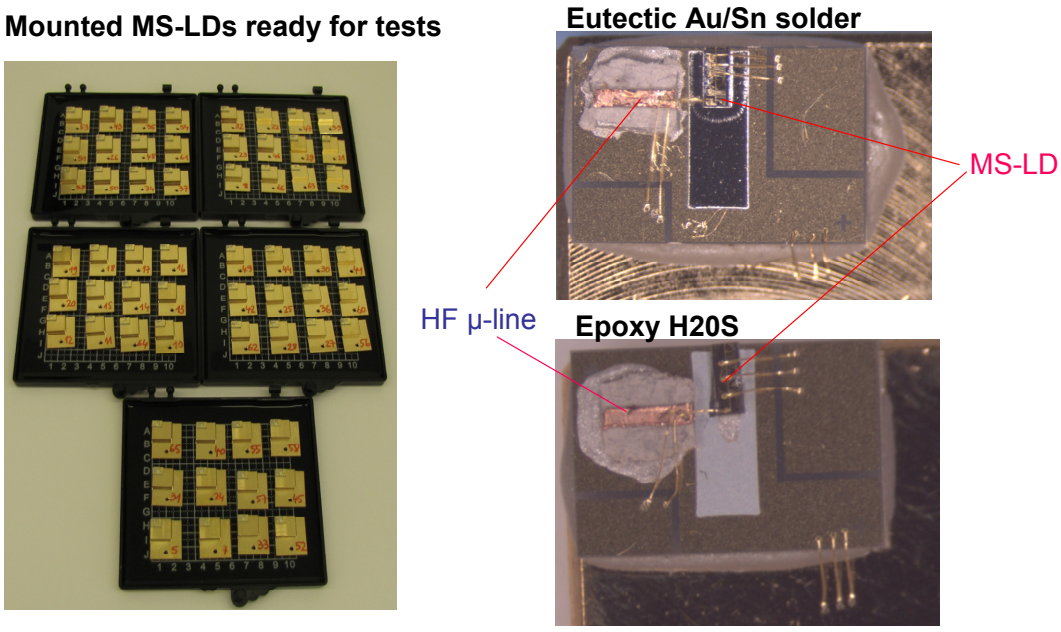

Fig. 5.10 Photographic image of mounted Femtoblue devices ready for dynamic tests: **Milestone M4.1 is reached.**

The table below summarizes devices available for tests and indicates Partner Institutions to which devices will be delivered for dynamical tests.

Cavity length, μm	CSEM	LPI	UCAM	Total
600	0	0	0	***0***
800	11	2	0	***13***
1000	6	6	9	***21***
1200	0	8	7	***15***
1500	0	6	7	***13***
Total	***18***	***22***	***23***	**63**

5.3 Conclusion with respect to project objectives of WP4 in phase 2

Evaluating success of activities of WP4 towards objectives of Phase 2, we conclude that the main objectives of the tasks WP4.3 and WP4.4 with the final result of “Milestone M4.1 Preliminary samples of multisection laser structures” have been reached.

In addition the consortium has developed advanced to the SOA processing technology to meet the final design requirements, which will be used in Phase 3 of the project.

6. Tests and evaluation of multisection laser structures (WP5)

This section serves to

1. Describe the characteristics of the first set of multisection devices fabricated within the Consortium;
2. Describe preliminary measurements of parameters of ultrashort optical pulses generated by GaN-based lasers in active and passive mode locking as well as in superradiant regimes;
3. Make a conclusion on how to proceed further and what should be modified in the design of lasers

6.1 Tests of preliminary samples of multiple section lasers in self-mode locking regime

22 devices were provided from CSEM for testing the laser operation in self-mode locking regime. They have different cavity configurations and emission properties. In further Sections we briefly describe the samples, their c.w. performance, and operation under strong reverse bias of the absorber sections and ns pulsed driving of the gain sections. The last regime is supposed to produce self-mode locking effect.

6.1.1 Samples description

All devices under test have emission wavelength of around 412-417 nm at room temperature. Typical c.w. threshold currents were in the range of 55-85 mA. Some lasers have 2 micron width of the active waveguide, while the rest have 3 μm wide active regions. The cavity lengths of the lasers were 800 (2 samples), 1000 (5 samples), 1200 (7 samples), and 1500 μm. The absorber section lengths varied from 50 up to 150 microns.

The devices ## 37, 40, 63, and 64 did not lase from the very beginning. They produced just spontaneous emission with strange far-field emission patterns (## 63 and 64). They were useless for further measurements. It has been found from the very beginning that fast degradation of lasers is the main obstacle for achieving mode locking and proper measurements of the laser performance. Some lasers have so short lifetime (~ 30 minutes) that it was difficult to get reliable even static emission parameters.

6.1.2 c.w. performance of the samples

Static emission parameters of the devices were determined first. This allows us to separate the devices which degrade quickly from those which can generate large power levels for long enough time. Figure 6.1 illustrates L-I characteristics of the lasers # 14 and 51.

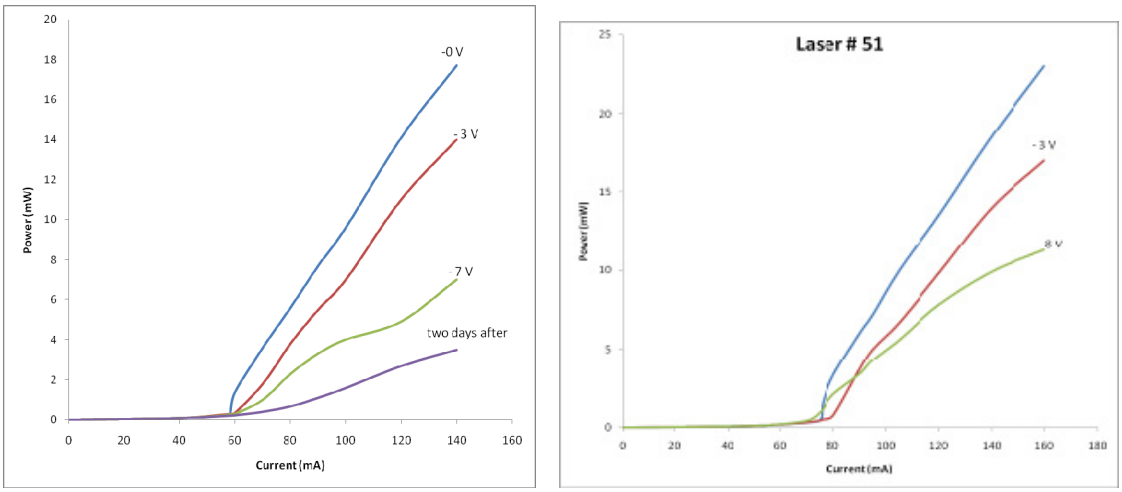

Fig. 6.1. L-I characteristic of the laser # 14 and 51 at different reverse biases.

The general feature of L-I characteristics of more or less properly working devices is weak dependence of the threshold current on the reverse bias. The optical power drops strongly with increasing the bias, whereas the threshold increasing not much. This is because that saturable absorption does not increase substantially. Fig. 6.1 (top) shows how the device degraded after 2 days of testing.

Some devices exhibited L-I curves which resembled superluminescent diodes but not standard lasers. Figure 6.2 illustrates this fact.

2 devices of the available set (# 61 and 63) were very insensitive to variations of the reverse bias. This is shown in Figure 6.3.

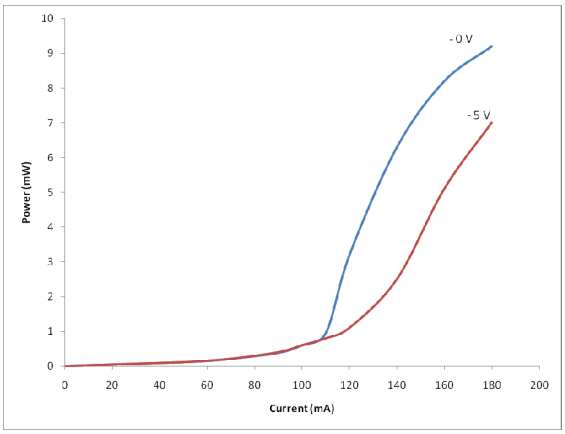

Fig. 6.2. L-I characteristic of the device # 36

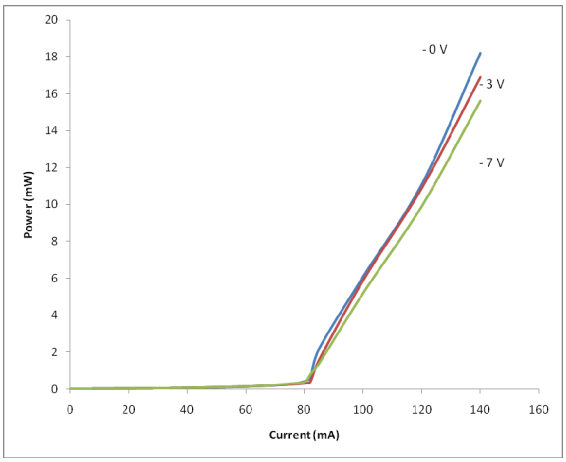

Fig. 6.3. L-I characteristic of the device # 61

All devices were gradually degraded during c.w. measurements. Typical dependence of the emission power on time is presented in Figure 6.4.

It has been found that the rate of the degradation increases with increasing the reverse bias. The problem of laser degradation is a big problem and must be solved later on. The reason of the very fast degradation of the present samples is unclear at the moment.

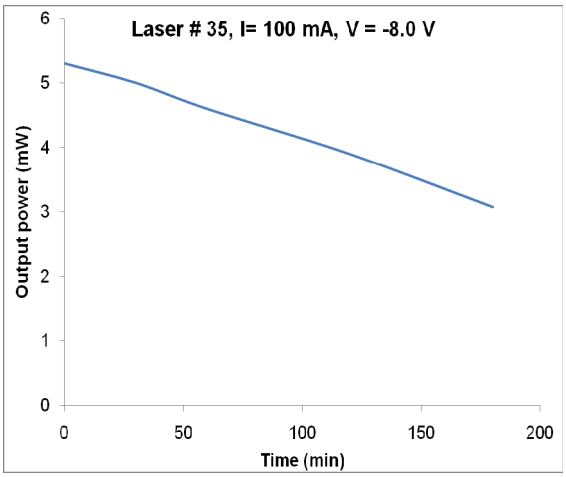

Fig. 6.4. Typical degradation of lasers under test

6.1.3 Optical spectra in pulsed regime

It was found some time ago that optical spectra of GaN-based lasers exhibited some peculiarities. Longitudinal mode clusters are often observed in optical spectra. The typical separation between individual clusters is about 8-10 times larger than the longitudinal mode spacing. This effect has also been observed in the lasers under test. Figure 6.5 illustrates typical optical spectra of the lasers.

The separation of the mode clusters is 0.16, 0.22, and 0.29 nm, whereas the longitudinal mode spacing is around 0.016 nm and 0.024 nm for 1500 and 1000 micron long lasers.

6.1.4 Streak camera measurements in pulsed regime

Due to the observed degradation, we decided to use pulsed driving conditions with low duty circle and measure laser dynamics with the available single-shot streak camera. The measurements were carried out at 2 fastest streak speeds of the streak camera, namely at about 200 ps and 750 ps scales on the screen. The ultimate temporal resolution at these speeds was 0.9 ps and around 4 ps, respectively. The laser beam was collimated on the input slit of the camera. The output power levels were enough to observe clearly individual optical pulses. Using the streak camera it was possible to monitor different dynamic regimes of the lasers under test, including relaxation oscillations, self-Q-switching, and very fast pulsations at repetition rates nearly the cavity resonant frequency. Figure 6.6 shows typical Q-switched pulses from the laser # 39.

The shortest pulse width is just above 20 ps, the pulse repetition rate is 7.7 GHz. The pulse frequency is strongly dependent on driving current amplitudes. Nanosecond (2-10 ns long) electrical pulses were applied on the gain sections of the devices with amplitudes varying in the range of 7-14 V across 47 Ohm serial load and the laser diode. These Q-switched pulses can be easily detected by high-speed photodiodes and sampling oscilloscopes.

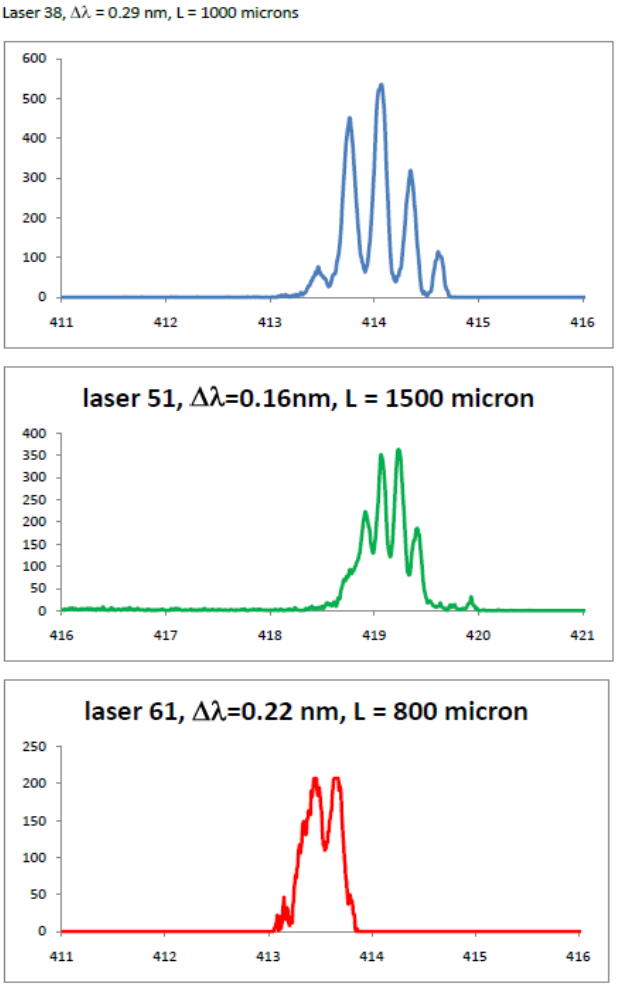

Fig. 6.5 Optical spectra of devices ## 38, 51, and 61

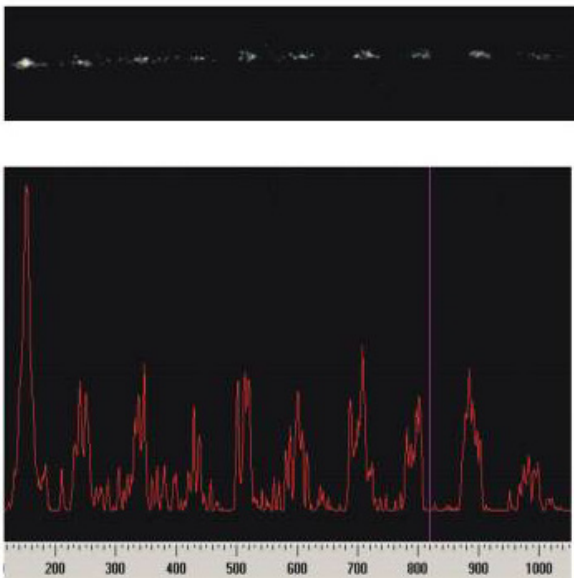

Fig. 6.6. Q-switched pulses of the laser # 39. Applied voltages are 9.7 V at gain section and 0 V at the absorber section

6.1.5 Very-high-speed self-pulsations or passive mode locking in GaN-based lasers

It has been found during the present study that some lasers can generate very high speed pulsations with a few picoseconds pulse durations. The pulse period of these pulsations is close to the round trip time of the laser cavities. Such pulses were generated from the lasers ## 35, 36, 38, and 51. Figure 6.7 illustrates self-pulsations from the laser # 36. The duration of individual pulses in the train varies from 6 to 10 ps, the pulse period is 31 ps. The laser # 36 has the cavity length of 1000 microns and the absorber length of 150 microns. At some currents these pulsations were modulated by lower frequency (3-5 GHz), much like in the case of Q-switching mode-locking [Hönninger99]. These are shown in Figure 6.8.

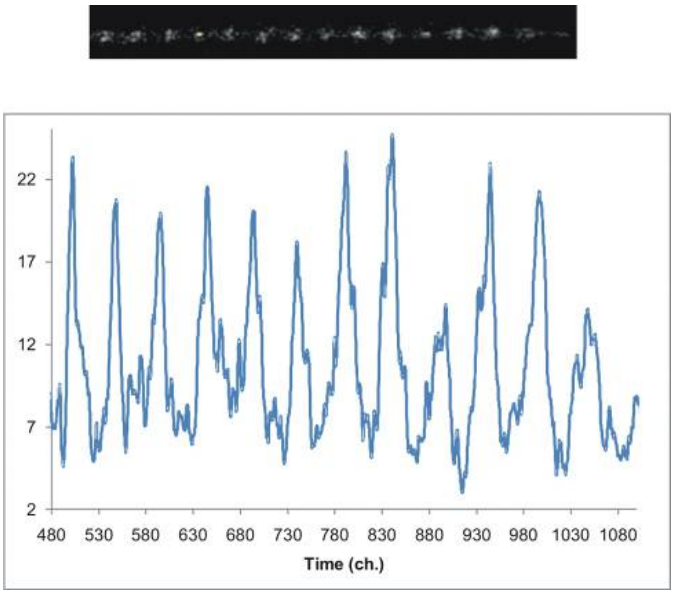

Fig. 6.7. Pulses from the laser # 36. Applied voltages are 13.7 V at gain section and -8.7 V at the absorber

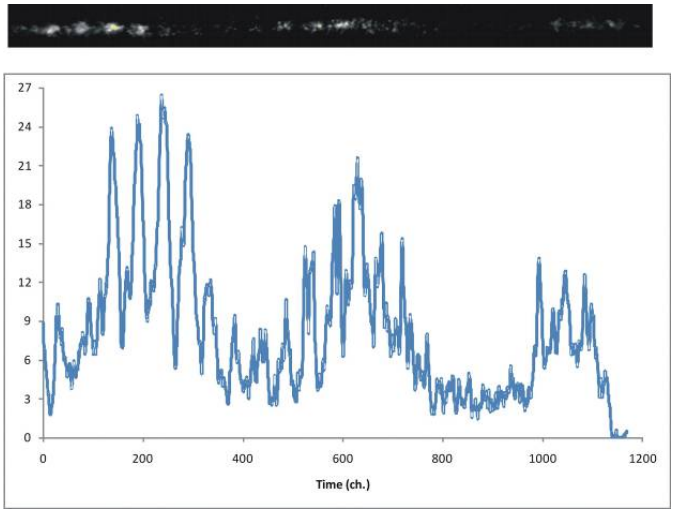

Fig. 6.8. Pulses from the laser # 36. Applied voltages are 9.2 V at gain section and -8.7 V at absorber. Pulse period is 32 ps. Pulse widths are 7-14 ps.

The frequency of pulsations is close to the round trip frequency of the laser cavity. Similar pulsations were observed from the device # 38 (Fig. 6.9).

The laser # 38 has the cavity length of 1000 microns and the absorber length of 50 microns which is 3 time shorter than in the previous case.

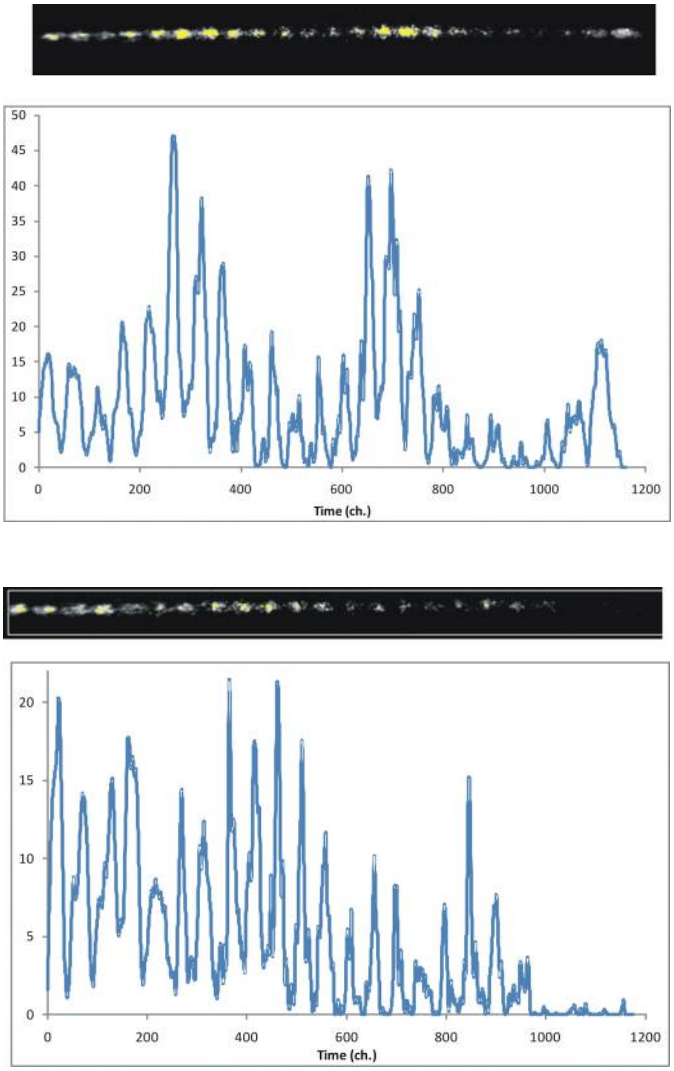

Fig. 6.9. Pulses from the laser # 38. Applied voltages are 9.6 V at gain section and -5.3 V at absorber (top) and – 15.5 V (bottom). Pulse period is 32 ps. Minimum pulsewidth is 7 ps.

Laser # 51 generated even faster pulsations. It has the cavity length of 1500 microns and the absorber length of 150 microns. Picosecond pulses from the laser are shown in Fig 6.10.

The rough estimation of the minimum peak powers of the observed pulses is over 150 mW.

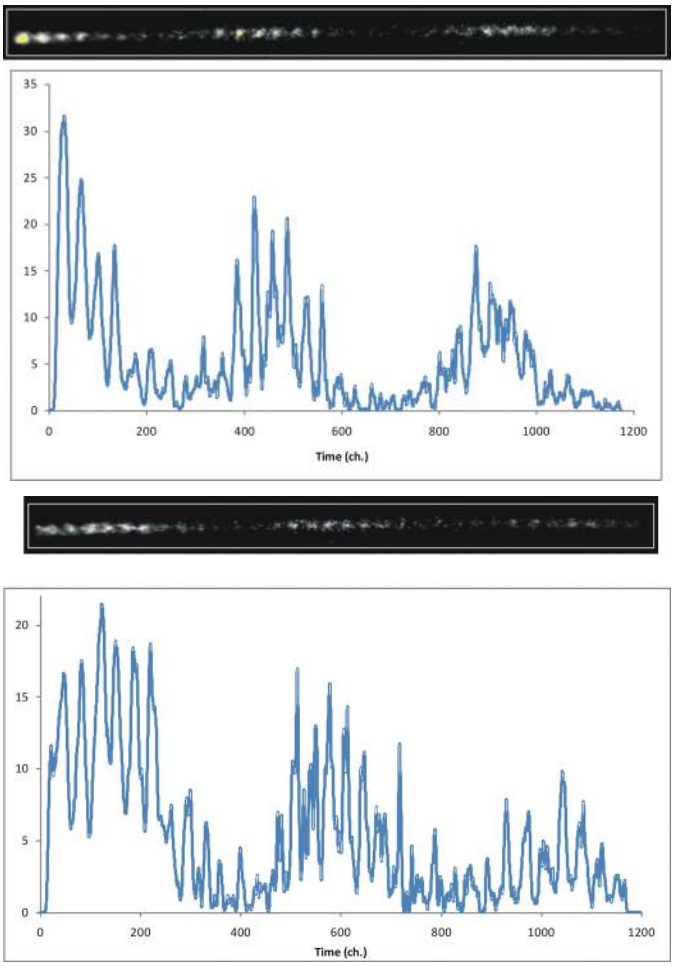

Fig. 6.10. Pulses from the laser # 51. Applied voltages are 8.7 V at gain section and -6.0 V at absorber (top) and – 3.9 V (bottom). Pulse period is 22 ± 2 ps. Minimum pulsewidth is 5 ps.

However we have noticed the following inconsistency between the measured and evaluated pulse repetition rates in the passive mode-locking regime. The round trip time for the lasers 36 and 38 is around 23.3 ps (44 GHz) at the group refractive index of 3.5 and the cavity length of 1000 microns. Passive mode-locked pulses are supposed to have this period. The same value for the device # 51 is 35 ps (32 GHz). In our case the experimental data show that the pulse period for shorter lasers (36 and 38) is 32 ps, whereas for the longer laser # 51 it is 22 ps. Thus, instead of 23 ps we have 32 ps, and instead of 35 ps we have 22 ps. The first measurements showed that the pulse repetition rate does not strongly depend on the driving current amplitude and the value of the reverse bias, as it should be in passive mode-locking regime. Thus in case of passive mode locking, the period of pulses must not depend on the driving conditions and depends on the parameters of the cavity [Vasil'ev-95]. On the other hand, the physical origin of such high–frequency pulsations is unclear, if they cannot be attributed to passively mode-locked pulses.

6.1.6 Conclusion

The main conclusions of the study are:

1) Unusually fast degradation was observed in all fabricated devices;
2) The control of the amount of the intracavity absorption using the reverse bias is weak. In most of the lasers, increasing of the reverse bias does not result in substantial increase of absorption. This behavior is different as compared to GaAs/AlGaAs lasers;
3) The absorber section in all tested devices is not sufficiently long. This results in insufficient absorption in the cavity;
4) The absorber lengths in future lasers should be at least 20-25 % of the total length of the devices;
5) Due to poor performance of the lasers under test, it was not possible to measure pulse durations using SHG autocorrelation;
6) Ultrafast self-pulsations have been observed in some lasers with pulse periods of 22 and 32 ps and the minimum deconvolved pulsewidth of 3-5 ps;
7) The periods of picoseconds pulses are close to these of passively mode-locked pulses. The discrepancy of pulse periods should be clarified in further experiments with a new set of fabricated lasers
8) At the moment, we are not 100% sure that the observed picoseconds pulses originate from passive mode locking.

6.2 Tests of preliminary samples of multiple section LDs under active mode locking

UCAM received 22 samples of mounted two section devices with different device lengths and waveguide widths. Extensive measurements showed that only a small proportion of devices exhibit RF components. These RF corresponded to their round trip frequencies and represented amplitude if electrical signal was greater than 1 mV. All 22 devices were initially tested. This included a detailed investigation of their VI performance however, 5 devices were rejected due to absence of a p-n junction (in the absorber section). The remaining 17 devices were investigated further. A second test aimed to establish the amount of absorption provided by a reverse bias applied to the absorber section. This test revealed that 8 out of 17 devices exhibited no change in output power as function absorber voltage up to -10 V. This left 9 devices for further investigation.

6.2.1 Initial characterization

The remaining 9 devices exhibited changes of output power and absorption with time, therefore output power was studied as function of time for fixed driving conditions to determine how the devices behaved. This measurement aimed to quantify the typical lifetime of the absorber section at the moderate absorber voltage of -5 V. This was necessary, as stable operation over an extended time is a prerequisite for measurements of both passive and active mode-locking operating conditions. The output power was measured using a calibrated photodiode with a

large input aperture. In Fig.6.11, output power vs. time is plotted for two different devices. Here, device denoted as I is device no.10. This device was 1 mm long with a 50 µm long absorber section and waveguide width of 2 µm. Another device (II) is device no.26. This second device was also 1 mm long but with a 100 µm long absorber section and a 3 µm wide waveguide.

In both cases the absorber section was biased with - 5 V and the gain section was biased with direct current (d.c.) chosen to yield average output powers between 10 and 20 mW. The output powers in Fig.6.11 show that the power was relatively constant then underwent a rapid change after 1-2 hours, followed by a largely unchanged output power level. In these devices the output power stabilised within the time window shown in fig.6.11, and remained largely constant thereafter.

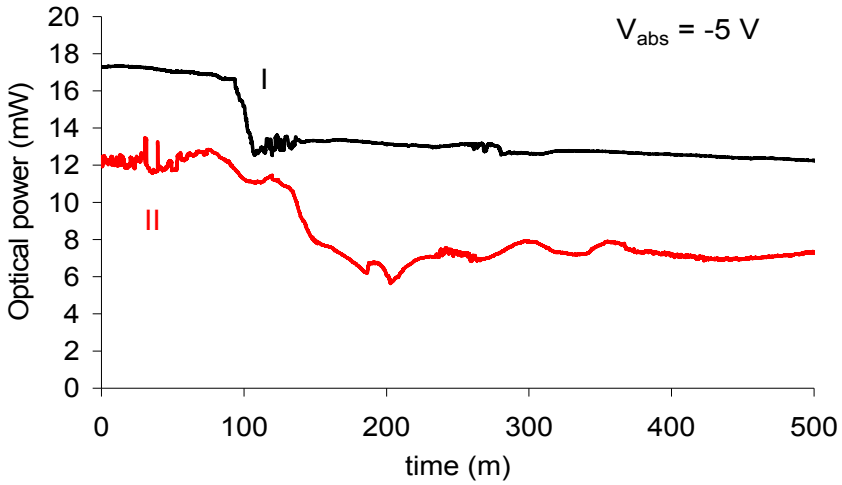

Fig. 6.11: Output power as a function of time for two 1 mm long devices. The device denoted as I has 50 µm long absorber section and 2 µm wide waveguide compared to device II with 100 µm long absorber section and 3 µm waveguide width. Both devices are 1 mm long.

The main difference between devices of type I and II is the performance of the absorber section after the short stabilisation time reported above and shown in Fig. 6.11. In some devices (type I) there was little initial voltage dependent absorption, which was no longer detectable after an hour of operation (Fig.6.12a). However, other devices (type II) stabilised after a few hours and showed almost 3dB of voltage dependent absorption, as shown in Fig. 6.12b. There has been no device tested which has enough voltage dependent absorption to frustrate lasing. This clearly implies that the absorber length should be increased in future device designs. A comparison between inter-contact resistances before and after the fact degradation revealed no significant change in the inter-contact resistance. A typical value of inter-contact resonance was around 650 kΩ.

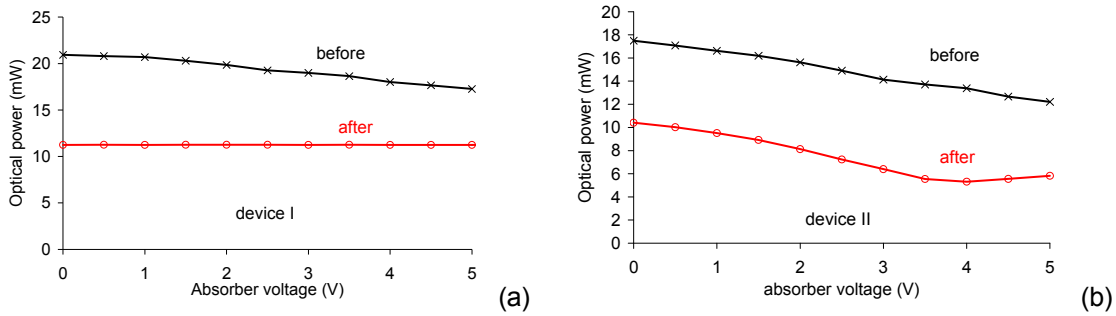

Fig. 6.12 Output power vs. voltage before and after the rapid change in output power in Fig. 6.11.

6.2.2 RF characterization

It is important to characterise the RF performance of a mode-locked laser, as both actively and passively mode-locked operation produces a large component of its optical power modulated at the round-trip frequency. Thus measurements of the RF content of the optical signal are a key first step to demonstrating mode-locked operation. Hence measurements of the dynamic performance have been made on a number of devices, which show similar trends, with device no. 26 (of type II above) being reported here in detail.

The measurement setup used to study the round trip frequency is described schematically in figure 6.13. The absorber section is biased with a d.c. reverse bias voltage. Output power is collimated to the single mode fibre using a set of microscope objectives (Melles Griot 25x and 44x) and connected to a fast (40 GHz) visible photodiode (New Focus 1004). This photodiode is attached to the RF spectrum analyser (RFSA) with a maximum bandwidth of 50 GHz.

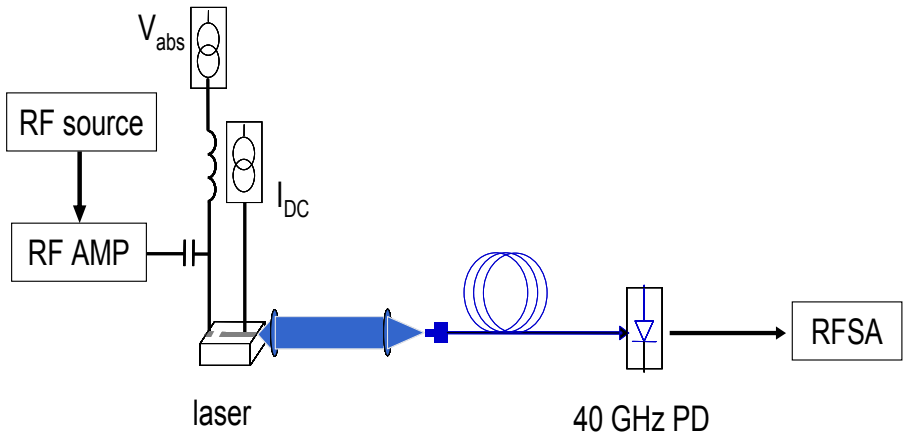

Fig. 6.13 A schematic representation of measurement setup used to stud RF frequency and enhancement of RF components when RF modulation is applied. 40 GHz PD correspond to the fast photodiode and RFSA is RF spectra analyser.

Figure 6.14 represents the LIV performance of the laser diode no. 26 where the absorber section is biased with -5 V and the gain current is varied up to 120 mA. LI data indicate an

optical kink (which might be attributed to a transverse mode hop) and the maximum output power which was reached for gain current of 110 mA. This fact restricted the use of safe gain current level up to 115 mA. The performance of the laser under this regime of operation is repeatable, with the laser having a good lifetime.

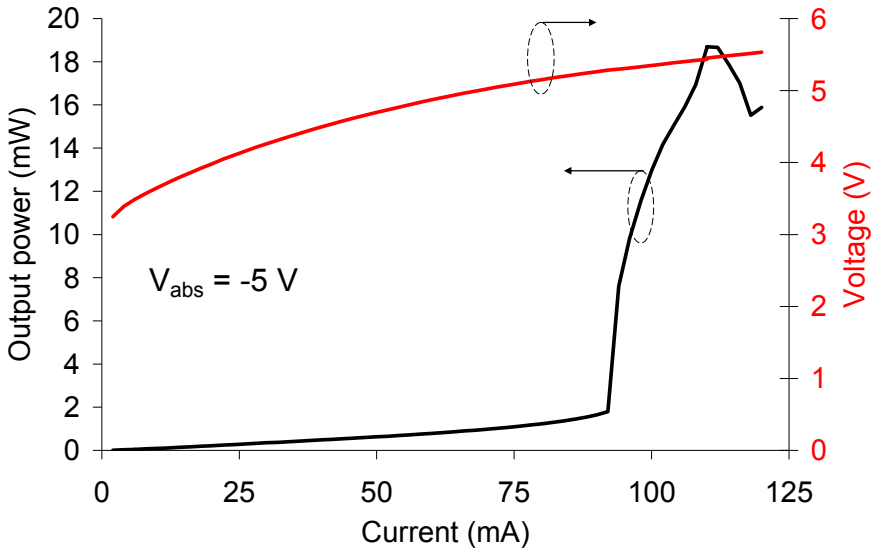

Fig. 6.14 LIV performance of FB laser where absorber section is biased with -5 V and gain current is varied up to 120 mA.

The output power and absorber current are plotted as a function of reverse bias voltage to the absorber section in figure 6.15. This figure shows initial performance as well as that after the power drop experienced after about 1 hour of operation, indicating that even after the rapid change in optical power, the absorber voltage still changes the optical power and absorber current (thick lines in figure 6.15).

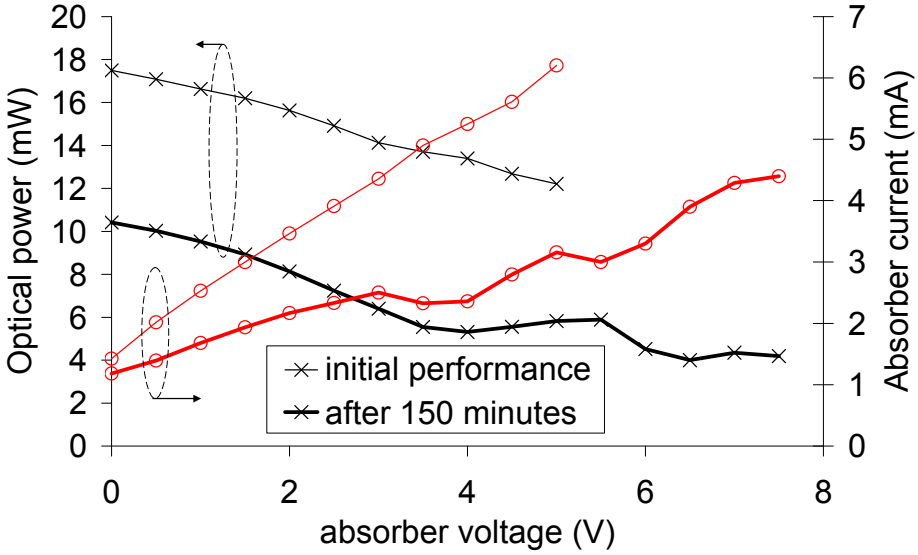

Fig. 6.15 Optical power and absorber current for current of 110 mA as function of absorber voltage prior to the measurements (thin line) and after 150 minutes for absorber biased with -5 V (thick line).

In order to discover regions of operation which might be candidates for active mode-locking, RF spectra were studied for gain currents between 90 and 115 mA and reverse biases up to -7.5 V applied to the absorber section. A strongly modulated RF spectrum, at the laser's round trip frequency, was indicative of the potential for short pulse generation. The results revealed that peak electrical power greater than – 72 dBm was only observed for gain current of 110 (figure 6.16) and 115 mA (figure 6.17).

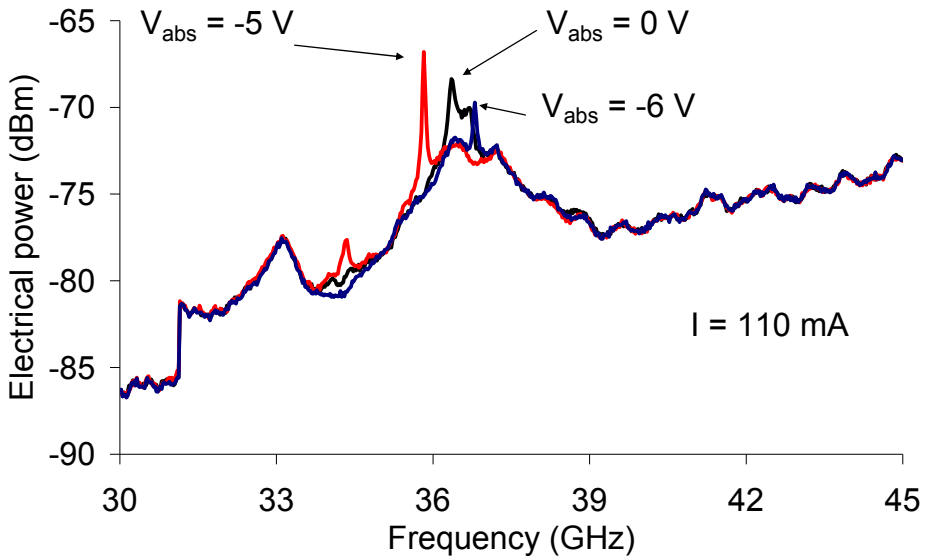

Fig. 6.16 RF spectra for gain current set to 110 mA and absorber voltage equal to 0, -5 and - 6 V.

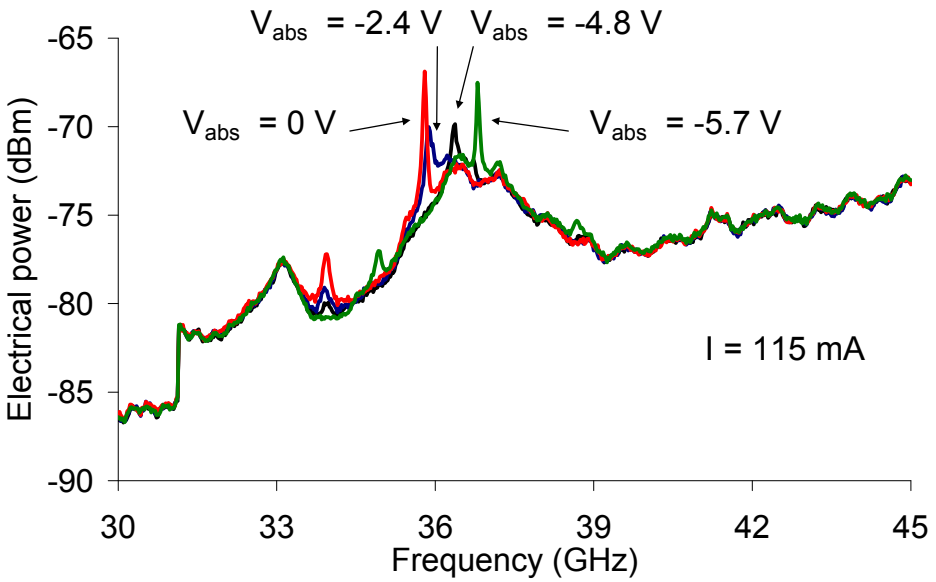

Fig.6.17 RF spectra for gain current set to 115 mA and absorber voltage equal to 0, - 2.4, - 4.8 and - 5.7 V.

The maximum detected RF power from the fast photodetector was equal to - 67dBm. This rather low value corresponded to 3 mW modulation amplitude into a 50 Ω load. This explains why no modulation was detected on an oscilloscope.

6.2.3 Active mode locking

Finally, active mode-locking has been investigated. An RF synthesizer fallowed by an RF amplifier (with bandwidth between 33 GHz and 39.8 GHz) was used to apply an RF signal combined with reverse bias to the absorber section of the lasers. For the d.c. conditions investigated above, the RF frequencies were swept over 100MHz around the round-trip frequency indicated by the RFSA in the passive mode-locking experiment. No visible enhancement to the RF power emitted by the laser was detected. This was again attributed to the low voltage dependent absorption, together possibly with the large value of carrier lifetime measured in the absorber section of these lasers.

6.2.4 Conclusion

The conclusions of the present investigation are:

1) Initial was observed in all devices under test;
2) Most devices showed output powers independent of reverse bias after the initial degradation
3) The absorber section lengths in all devices are too short. This results in insufficient modulation of the absorption in the cavity;
4) Active mode locking has not been achieved using the first set of fabricated two section lasers.

6.3 Optical bistability measurements

Optical bistability is observed in cw-operating InGaN-based laser diodes including a saturable absorber (SA) section. The dependence of the light-current hysteresis on the SA section length and reverse bias (V_{SA}) has been studied. An analytical approach is developed to estimate the carrier lifetime τ_a in the SA section from the measurements of the hysteresis width, which leads to τ_a = 1.9 ns at zero bias. τ_a is found to decrease rapidly for higher reverse biases and a minimum of τ_a = 0.4 ns is interpolated for flatband conditions. We explain the dependence of the carrier lifetime on V_{SA} via the modification of the quantum-confined Stark effect.

Under certain conditions, the saturable absorber (SA) section in MS-LDs causes a hysteresis loop in the light-current (*L-I*) characteristics. Such optical bistability is a desirable property for all-optical switching and signal processing applications. For the objectives of the project it enables to make assessment of several important device parameters. It was found that the conditions for bistable and unstable regimes notably depend on the carrier lifetime and the absorption coefficient in the SA section.

We report on optical bistability in InGaN/GaN-based MS-LDs operating in cw at 420 nm (A2109 sample). The reserve bias (V_{SA}) applied to the SA section allows to control the width of the *L-I* hysteresis. Analytical expressions are obtained for switching-on and switching-off threshold currents by solving rate equations. The numerical fit of the experimental data enabled us to estimate the carrier lifetime in the SA section as a function of V_{SA}. Interestingly, instead of revealing a monotonous saturating decay as in devices fabricated with conventional III-V compounds, τ_a reaches a minimum value due to the quantum-confined Stark effect (QCSE) taking place in the MQWs.

The MS-LD layer A2109 was grown in a metal-organic vapor phase epitaxy reactor on a 2 inch *c*-plane free standing GaN substrate. The active region is made of a double (N_{QW} = 2) InGaN MQW heterostructure, optimized for emission at 420 nm. The thickness of each QW is d_{QW} = 4.5 nm. MS-LDs are fabricated using common processing techniques and following the standard ridge-waveguide LD process flow. The nominal width of the ridge is W = 2 µm. The gain and absorber *p*-type electrodes are separated by a 15-µm-wide stripe and are electrically isolated (the series leakage resistance is 500 kΩ). Laser bars are cleaved and the facets left uncoated (reflectivity is R = 0.17). Structures with three different absorber lengths (L_{SA} = 50, 100 and 150 µm) have been studied, alongside with a single-section LD. The length of the cavity is L_{cav} = 800 µm. To reduce the impact of variations in the growth parameters of the layers and processing imperfections, four devices from the same laser bar are tested.

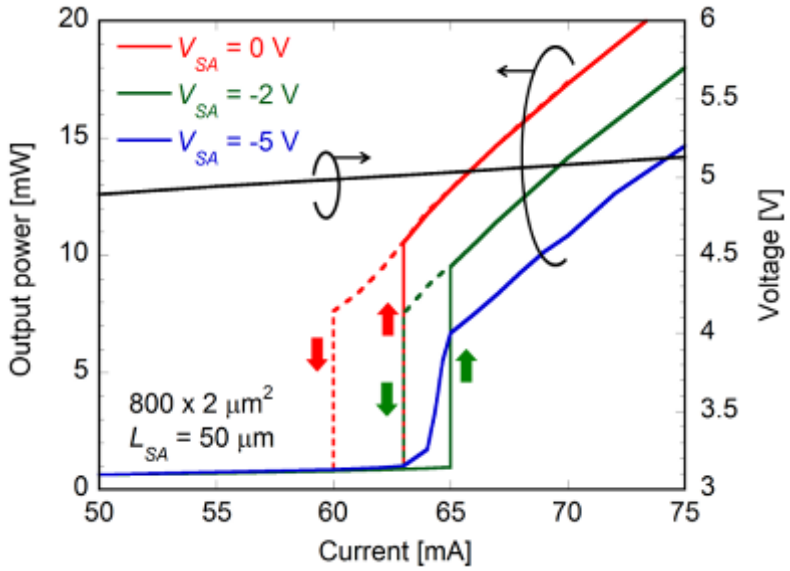

Fig. 6.18 L-I-V characteristics of the MS-LD with L_{SA} = 50 µm for V_{SA} = 0, -2 and -5 V.

Figure 6.18 shows the cw L-I-V curves of the MS-LD with L_{SA} = 50 µm for different reverse bias. Threshold current and voltage are around 63 mA and 5 V, respectively. A hysteresis loop is observed in the L-I characteristics of the device for V_{SA} = 0 and -2 V (see arrows). In the bistable region, both optical states (laser on and off) are stable. When further increasing the reverse bias to V_{SA} = -5 V, the hysteresis disappears.

In order to interpret the measurements, we use a standard LD rate equation model extended for two sections. We assume linear gain and absorption approximations, single mode operation, and neglect spontaneous emission and current leakage from the gain to the absorber section. A dimension-less parameter V_a is introduced to describe the change in the low-signal absorption coefficient. It is a non-linear function of the reverse bias V_{SA} and accounts for the variation of the transparency carrier density n_T = 1.5x10^{19} cm^{-3} in the SA section: $n_T(1\text{-}V_a)$. Expressions for the normalized switching-on threshold $J_{n,th}$ and the hysteresis loop width $\Delta J_{n,th}$ are obtained using the Lyapunov exponent method and calculating the boundaries of the region with three non-negative solutions for the photon density:

$$J_{n,th} = \frac{2L_{cav}\alpha_i - 2\ln(R)}{g_0 n_T \tau_n \Gamma(1-\alpha)} + \frac{T_{cav}}{\tau_n}\left[1 + \frac{\alpha\sigma(1-V_a)}{1-\alpha}\right], \quad (6.1)$$

$$\Delta J_{n,th} = \left[\sqrt{\frac{\alpha(1-V_a)}{(1-\alpha)}\left(\frac{T_{cav}}{\tau_n}\sigma - \frac{T_{cav}}{\tau_a}\right)} - \sqrt{\frac{2L_{cav}\alpha_i - 2\ln(R)}{g_0 n_T \tau_a \Gamma(1-\alpha)\sigma}}\right]^2. \quad (6.2)$$

Analytical solutions are also calculated for the output power and the absorber current of the MS-LDs as a function of the pump current. These expressions depend on the length ratio of the absorber to the cavity α, the injection efficiency η_{inj} = 0.8, the carrier lifetime in the gain section τ_n = 1.4 ns, the confinement factor Γ = 0.03, the cavity round-trip time T_{cav} = 18.7 ps, the differential material gain g_0 = 0.6x10^{-6} cm^3/s, the ratio of differential absorption to differential gain σ = 5.5, and the internal loss α_i = 20 cm^{-1}. Device parameters were determined by optical gain spectroscopy and lifetime measurements performed on the single-section LD.

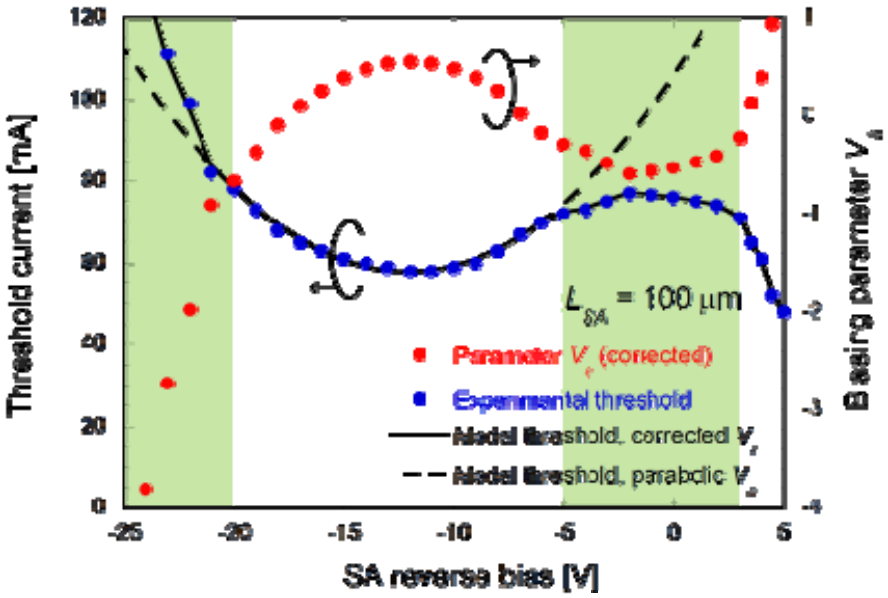

Fig. 6.19 Measured and simulated threshold currents for L_{SA} = 100 µm and corrected bias parameter V_a.

The switching-on threshold current was recorded as a function of V_{SA}. Bistability is present in two distinct voltage ranges: -5 V < V_{SA} < +3 V and V_{SA} < -20 V (Fig. 6.19, green area). The threshold dependence of MS-LDs on V_{SA} is a consequence of the QCSE which modifies the wavefunction overlap of electrons and holes and shifts the absorption edge in the SA section. A detailed study about its effect on the absorption has been published elsewhere.[13] A simultaneous fit of Eq. (6.1) to the threshold currents of the three MS-LDs enables us to define the relation between the biasing parameter V_a and the reserve bias V_{SA}. The QCSE energy shift and the variations in the wavefunction overlap are second–order perturbations in the Hamiltonian of the carriers confined in the QW without external electric field. Therefore, we initially assumed that $V_a = V_{aFB} - \mu(V_{SA}-V_{FB})^2/V_{FB}^2$ with V_{FB} = -12 V being the external bias compensating the internal piezoelectric and spontaneous polarization fields in the QWs, the parameters V_{aFB} and V_{aFB} - μ defining the effective transparency carrier density for flatband conditions and zero bias, respectively. As shown in Fig. 6.19, this parabolic approximation

exhibits a good agreement with the experimental data in the range -20 V < V_{SA} < -5 V. Outside this range, other effects take over that affect the threshold current in MS-LDs. From Eq. (6.2), we calculate that the MS-LD will operate in the bistable regime provided that:

$$\tau_a > \frac{\tau_n}{\sigma}\frac{1-\beta}{-\beta},\ \beta = -\frac{g_0 \sigma T_{cav} \Gamma n_T (1-V_a)}{2L_{cav}\alpha_i - 2\ln(R)}\alpha, \qquad (6.3)$$

where β is the ratio of the unsaturated modal absorption to the cavity loss.[7] This condition indicates that optical bistability is expected when the carrier lifetime and/or the unsaturated absorption in the SA section are significant. Interestingly, β is proportional to the parameter α. Using the parameters reported by the numerical fit, we find that, at V_{SA} = -5 V, the shortest carrier lifetime τ_a in the right- hand-side of Eq. (4.3) is equal to 1, 0.6 and 0.5 ns in the cavity with absorber length of L_{SA} = 50, 100 and 150 μm, respectively, indicating that bistability is more likely to occur with longer absorber section. This was confirmed at V_{SA} = -5 V and V_{SA} < -20 V, by observing bistability in the cavities with L_{SA} = 100 and 150 μm but not with L_{SA} = 50 μm.

The width of the hysteresis loop was measured in the three MS-LDs. For each reverse bias V_{SA}, it was plotted as a function of α and numerically fitted with Eq. (6.2) using τ_a as a free parameter, as shown in the inset of Fig. 6.20 for V_{SA} = 0 V. This way, we estimate the dependence of the carrier lifetime on V_{SA} in the bias voltage ranges where optical bistability is observed (Fig.6.20).

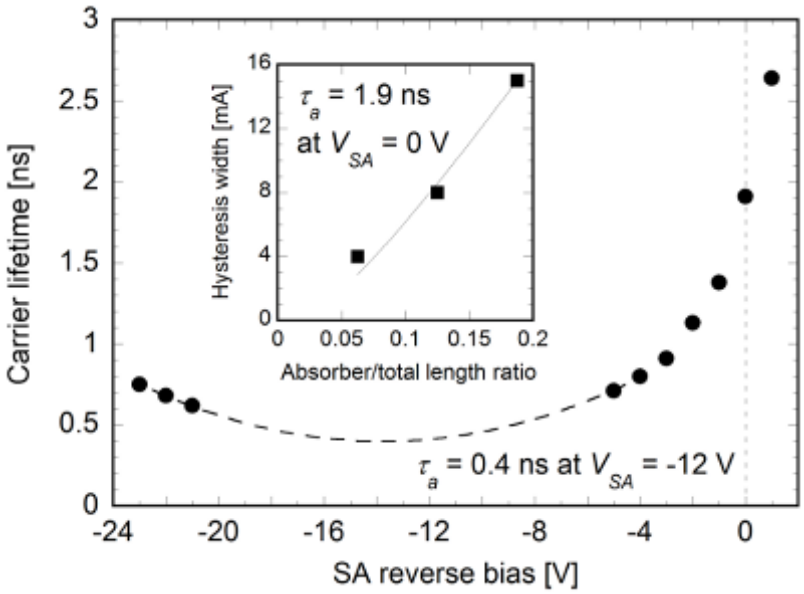

Fig. 6.20 Estimated carrier lifetime vs. V_{SA}. Inset: fit of the hysteresis width at V_{SA} = 0V.

The carrier lifetime at V_{SA} = 0 V is τ_a = 1.9 ns and it reaches a maximum at V_{SA} = 1 V. This is an expected behavior because, at small bias, the tunnelling probability from the QWs to the barriers is low and the recombination rate is decreased due to the reduced wavefunction overlap in the QW. When approaching flatband conditions (V_{SA} = -12 V), a sharp decrease of τ_a is observed and the bistability disappears at V_{SA} ≤ -6 V. At high reverse bias (V_{SA} < -20 V), the bistability reappears in MS-LDs with long absorber sections (L_{SA} = 100 and 150 μm). We believe that the increase of τ_a in this range is due to the pulling of electrons and holes in opposite directions of external field, yielding a reduced wavefunction overlap and, consequently, a lower recombination rate. Otherwise, if the leakage current from the gain section to absorber is the

dominating mechanism for optical bistability at high reverse bias, a noticeable absorber current would be detected at vanishing output power of the laser (see discussion linked to Fig. 6.21 below). The carrier lifetime was interpolated in the intermediate absorber bias range and a minimum of τ_a = 0.4 ns is predicted for flatband conditions. Here, the absorption coefficient is minimal due to strong QCSE energy shift, while tunnelling of the carriers from the QW to the barriers is increased. In this range, we expect that the absorber require a higher photon density to be saturated.

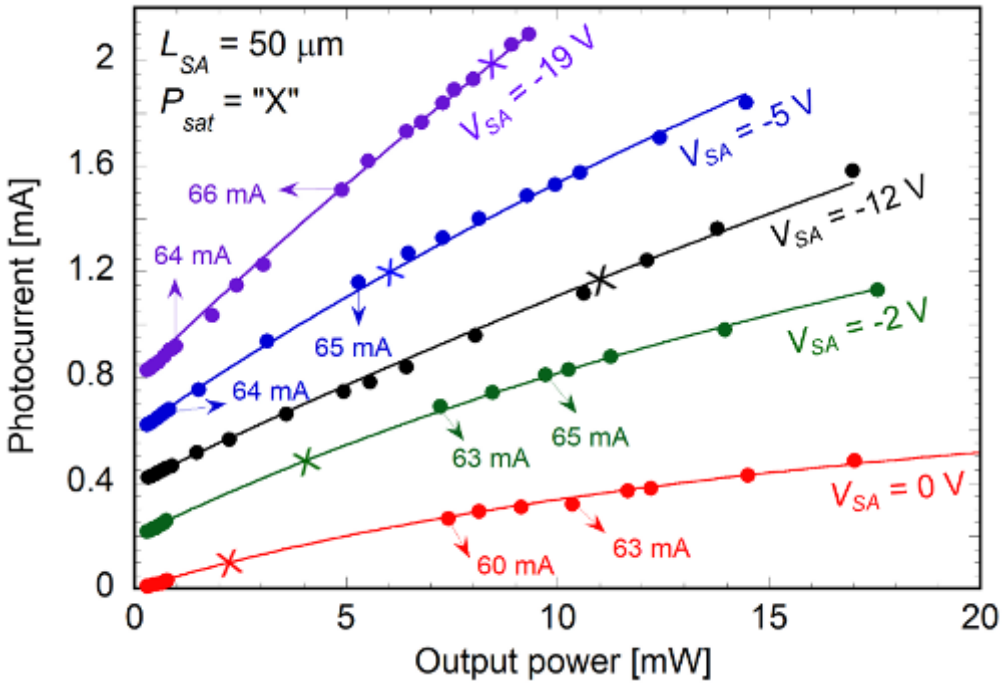

Fig. 6.21 Measured and simulated absorber photocurrent vs. output power in the MS-LD with L_{SA} = 50 µm. Curves are rigidly shifted by 200 µA steps for the sake of clarity.

To confirm our predictions, we measure the photocurrent I_A generated in the SA section as a function of the output power P_{out} of the device for different V_{SA} values. The latter is plotted in Fig. 6.21 for the MS-LD with L_{SA} = 50 µm (dots), along with modelling curves (solid lines). When interpolated at vanishing output power, all curves intersect at zero photocurrent, which confirms that the leakage current is indeed negligible in these MS-LDs. The photocurrent depends on several factors: the carrier generation rate as a function of optical power, the carrier recombination rate and the carrier tunnelling and drift rates through the active region. Also, at high negative bias the photocurrent is subject to the avalanche gain effect. Drift and tunnelling rates are expected to increase with the reverse bias. This can be evidenced by looking at the curves at low output power. The absorption coefficient of the SA at V_{SA} = 0, -2, -5 and -19 V is almost constant (similar V_a) but the I_A curves display a regular slope increase with increasing reverse bias, which means that carriers are extracted more rapidly from the active region. The only exception is observed for V_{SA} = -12 V where the absorption coefficient is lower (higher V_a).

The transition toward saturated absorber can be assessed by a change in the slope of the I_A curves. The model predicts that $I_A \propto P_{out}/(P_{out}+P_{sat})$ where the "saturation" power $P_{sat} \propto 1/\tau_a$ is 2.2, 3.8, 6.1, 11 and 8.5 mW for V_{SA} = 0, -2, -5, -12 and -19 V respectively (Fig. 6.21). This allows linking the absorber state to the operating regime of the MS-LD. As expected, at high

reverse bias, P_{sat} is large and reached above threshold: the MS-LD will operate in the stable or unstable regime in this range. On the other hand, in the bistable regime (V_{SA} = 0 and -2 V, Fig. 6.21), due to the long carrier lifetime, P_{sat} is low and reached below the switching-on threshold. This means that the threshold current is conditioned by the on-going saturation process and the sudden decrease of the absorption coefficient in the SA section. As soon as the MS-LD starts lasing, the photon density in the cavity increases bringing the absorber at a higher level of saturation, further reducing absorption. At this point, to switch the laser off, a decrease of the pump current is required in order to decrease the photon density in the cavity, the carrier density in the absorber, and, consequently, recover absorption.

These results show that not only the absorption coefficient can controlled by the negative reverse bias applied to absorber, but also the absorber recovery time τ_a. The evolution of τ_a is governed by the interplay between photocurrent extraction and carrier localization induced by the QCSE, reaching a minimum value for flatband conditions. This should have a strong impact in the ability to control the output of MS-LDs for stable, bistable and pulsating regimes. These findings are used in next section to interpret the experimental results on lasing dynamics.

6.4 Test of preliminary samples in superradiance regime

6.4.1 MLD samples

In this report, test results obtained from multisection LD of samples A1902 and A2109 of EPFL are included. Both sets of samples have an active region with 2 QWs. The samples differ by the width of the QWs, which impact the gain and carrier lifetime, and by the p- doping, which impacts the voltage drop. In what follows, it is important to note that the material loss in A2109 are smaller and the gain section carrier lifetime is longer as compare to A1902 (parameters of the samples are given in Table 3.6, Sec 3.5).

There were two mounted A1902 LD samples available (lasers #C and #I), out of which, laser #C has a crack over the active region and was not operating. Laser #I has shown lasing. (Other mounted devices of A1902 growth has been sent to LPI for tests).

Out of the growth A2109, there were 17 devices with the cavity length varying from 800 to 1000 µm with absorber length 50, 100 and 150 µm and waveguide width 2 and 3 µm. Four devices were utilizing eutectic Au/Sn solder for LD die mounting, while the rest utilize conductive epoxy (Epotek H20S).

6.4.2 Experimental setup

A dedicated experimental test setup has been assembled. The laser probing unit allows easy exchange of FemtoBlue mounted devices (Fig.6.22). It also capable to accept unmounted laser bars or solitary die (see the inset). For particular tests in superradiance regime, it incorporates high frequency probe (10 GHz) for driving gain section with nanosecond current pulses and two low frequency probes for DC biasing the absorber section. The microscope simplifies current probe positioning at the contact pads.

Figure 6.23 shows that the collimated output beam (from the gain section side) is sent to spectrometer (0.025 nm resolution), fs-ps autocorrelator and ultrafast photodetector whose output is monitored on the sampling scope (70 GHz bandwidth). Two fast detectors are available: 7ps / 50 Ghz with transimpedance 50 Ohm and 29 ps /12 GHz with transimpedance 1 kOhm .

The sensitivity of SHG autocorrelator is limited both spectrally and in power. The BBO crystal used in autocorrelator enables SHG for the input wavelength down to 410 nm. In the vicinity of this limit, the efficiency is lower. Most of tested femtoblue devices are very close to this limit. Quoted power limitation at the peak sensitivity of autocorrelator is defined by the product of average and peak power $P_{peak}P_{ave} \sim 3 \cdot 10^{-8} W^2$. In the vicinity of spectral range edge 410 nm, it is reasonable to assume that this value is increased by one order of magnitude. Fig 6.24 shows $P_{peak}P_{ave}$ product for pulse repetition rate limited by self-heating effects (period 550 ns) and assuming the relatively lower power regime of gain switching with pulse width of 20 ps. It can be seen that autocorrelator is expected to detect pulses of peak amplitude above 100 mW.

The gain section of DUT (Device Under the Test) was driven from a commercial current source proving 9 ns pulse of 1 A amplitude. Further reduction of the pulse width was obtained using home – build electronics enabling to produce 800ps pulses of 0.6 A amplitude into 50 Ohm load.

The peak power is estimated form the following inputs (i) measured average power (ii) pulse repetition rate of the pump current and (iii) recorder time-resolved traces of the optical pulse intensity.

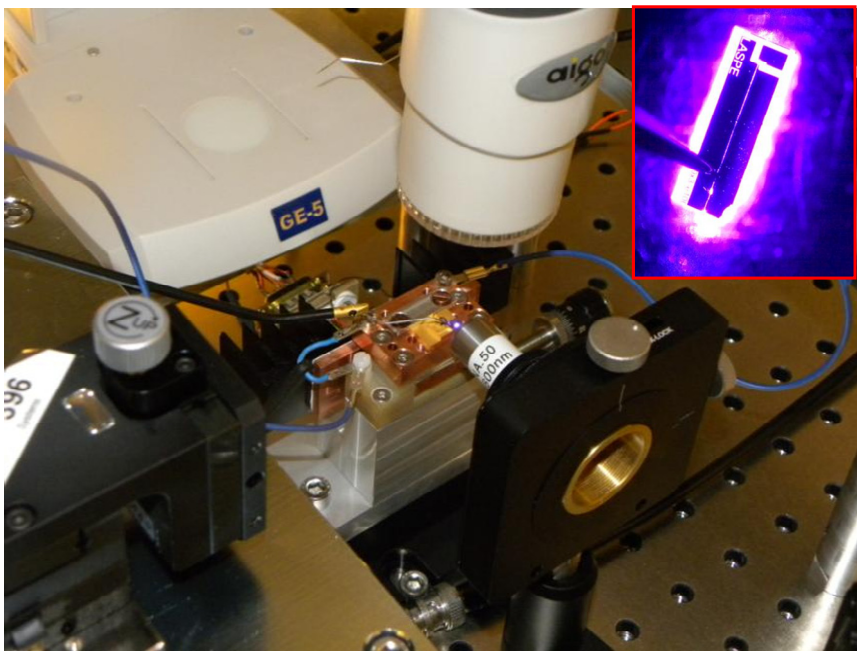

Fig. 6.22. FemtoBlue Laser probing unit with microscope, high frequency and low frequency probes, collimation optics and active cooling system. The image shows lasing mounted FemtoBlue device. The inset shows solitary die under the test.

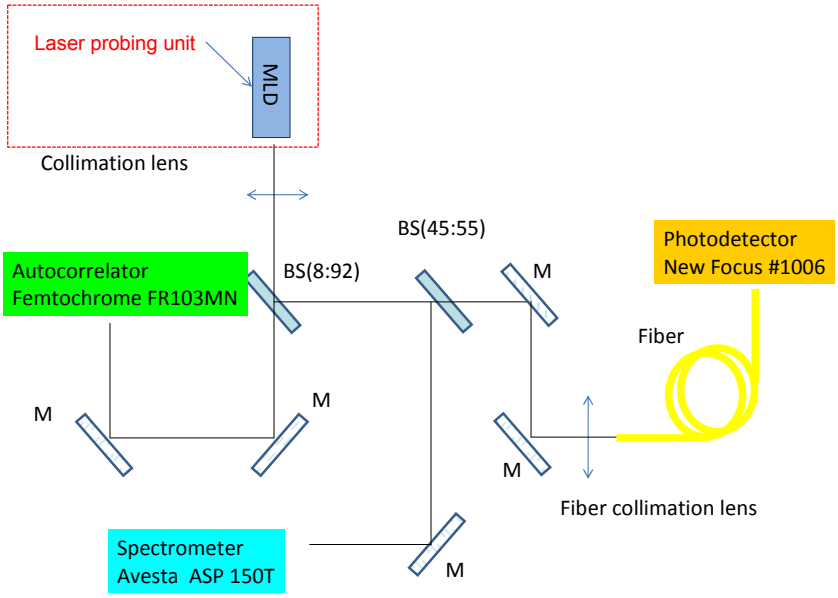

Fig. 6.23. Schematics of experimental test setup build for SR regime tests of FemtoBlue devices

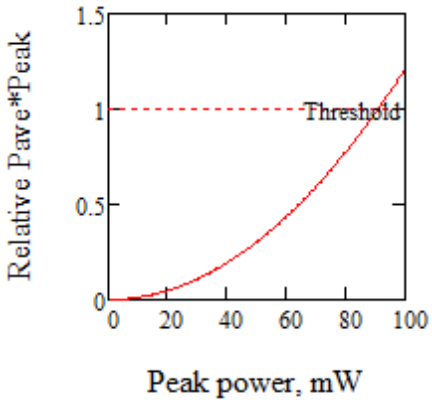

Fig. 6.24. Sensitivity threshold of SHG autocorrelator for gain switching regime of FemtoBlue devices vs pulse peak power. Pulse period is 550 ns, pulse width 20 ps. It follows that pulses of peak power 100 mW are expected to be detectable in SHG autocorrelator.

6.4.3 Results and discussion

Important observation was that there were no impact of using epoxy instead of a solder on devices performance. Devices were tested under short current pulses of large amplitude. The impact of absorber was verified by observing the optical spectrum. Only few devices were not emitting light. In one device, the output beam was off-axis, rendering this device not suitable for subsequent tests.

About half of the tested devices have shown no impact of the absorber bias on the emission spectrum. Although the directional emission of a beam have been observed, the emission spectrum in these devices was broad and as a rule, that devices had a waveguide of 3 μm

width, thus being transversally multimode. The fact that absorber had no impact on the emission features and spectrum, indicates that these devices were operating in superluminesence regime so as the cavity roundtrip has no impact on the emission spectrum emanating the cavity from the gain section side.

The approach for test was to perform detailed mapping of the lasing regimes, and then directly test the laser under conditions assuming the SR emission regime.

6.4.3.1 A1902 sample, 20 ns current pulse

Emission under short current pulses drastically differs from emission under cw operation regime. These devices utilize narrow QWs (3.5 nm width) and non optimal yet p doping. As a result, under reasonable pump rates at short pulses (20 ns), there were no lasing emission detected, even in the gain switching regime.

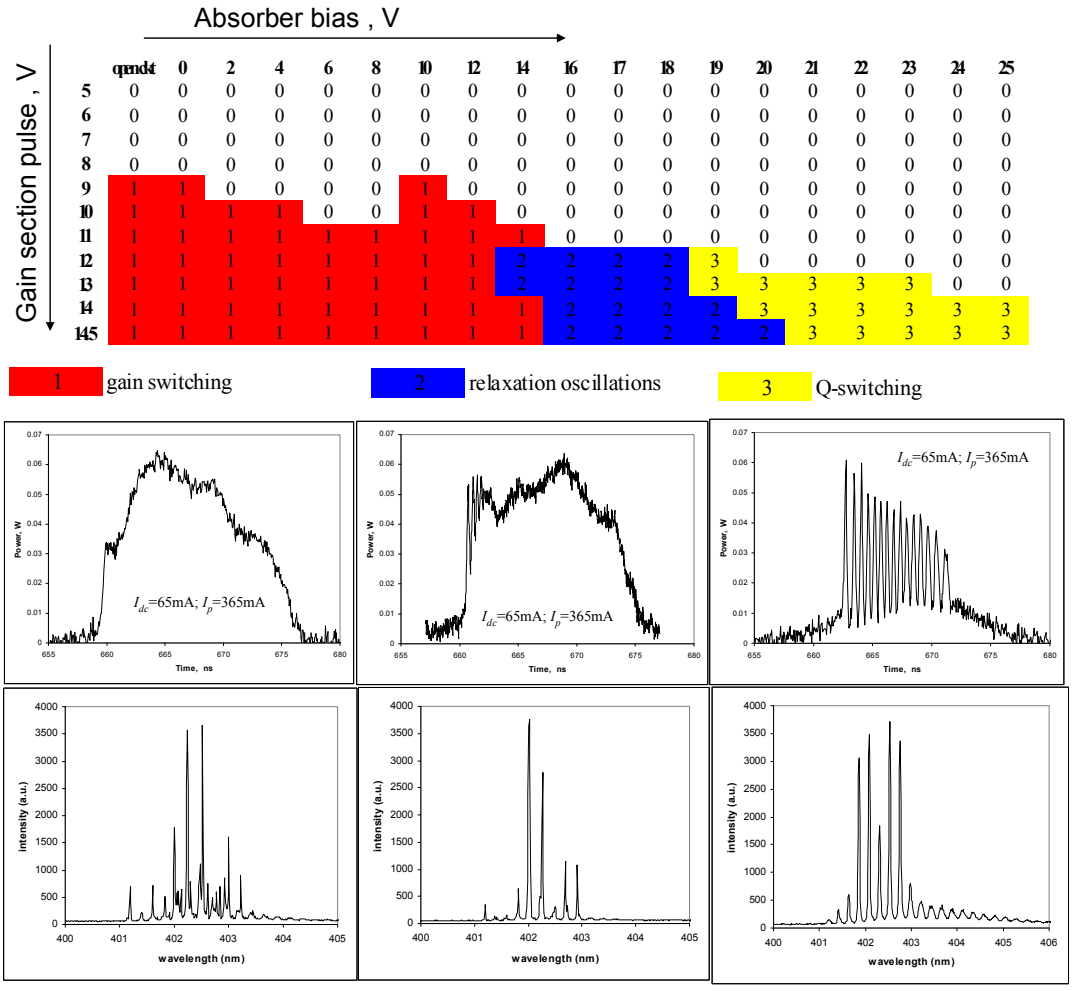

Fig. 6.25. Map of dynamic regimes in A1902 (laser #I) in function of absorber bias (Volts, horizontal axis) and pulse amplitude applied to the gain section (Volts, vertical axis, 1 Volt corresponds to the current amplitude 25 mA). The pulses of the width 20 ns and repetition period 550 ns are superimposed on DC bias current of 65 mA. The map shows dynamic regimes of gain switching (1), relaxation oscillations (2), Q-switching (3). Panels in the middle indicate typical pulse shape for each regime. The corresponding optical spectra are shown in the bottom panels. (Spectra are systematically blue--shifted by 6 nm as a result of an error in operating the spectrometer.)

The device under the test (laser #I) has a cavity length 800 μm with the length of absorber section 75 μm. The waveguide width is 2 um. To achieve lasing under short current pulses, the device was DC pre-biased at the level of 65 mA (below threshold). The nanosecond current pulses of variable amplitude were superimposed on DC pre-bias using bias-tee. The absorber was DC biased in reverse direction and the bias voltage was change in the range 0 to – 25 V. It was possible to operate at relatively high absorber reverse bias without degrading the structure. However at above 25 V, rapid degradation has been observed. The detection of time-resolved output pulses was made using 50GHz bandwidth detector. The results are summarized below.

Figure 6.25 shows the map of detected regimes in function of the absorber bias (horizontal axis) and amplitude of the pulse at the pulser output applied to the gain section. The dependence of the peak current form the pulse amplitude is linear, 14.5 V pulse amplitude corresponds to the current pulse amplitude of 365 mA superimposed on DC pre-bias.

The dynamic regimes of gain switching, excitation of relaxation oscillations and self-pulsations (or Q-switching) are observed in function of the absorber reverse bias. In all regimes, the peak power does not change significantly with the absorber bias, while the average power changes dramatically (Fig. 6.26).

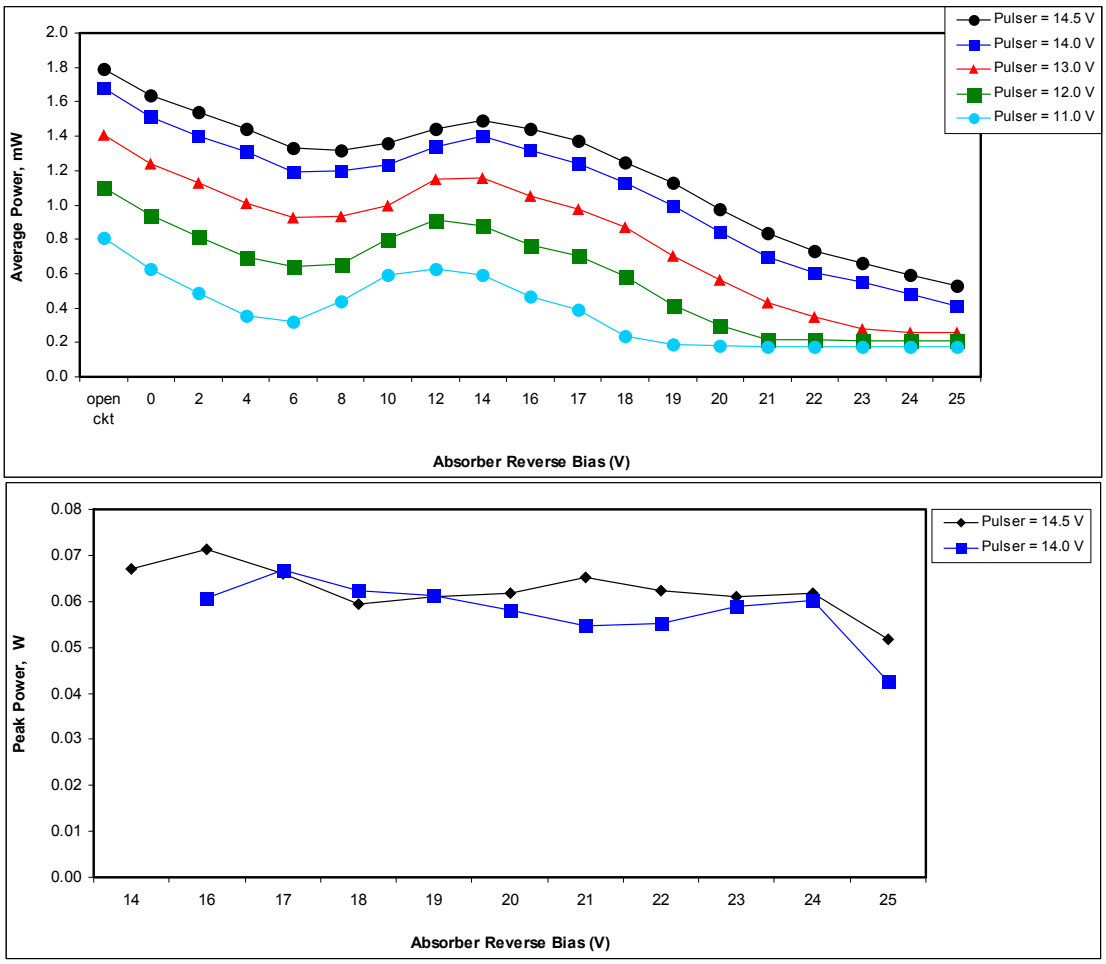

Fig. 6.26. Average power (top panel) and peak power (bottom panel) in function of absorber bias in A1902 (laser #I). The gain section is driven by pulses of amplitude 14.5 V (430 mA), 14 V (417 mA) 13V (388 mA) 12V (358 mA) and 11 V (332 mA) superimposed on DC pre-bias current of 65 mA. The pulse width is 20 ns and period is 550 ns.

From the dependence of the average power in Fig. 6.26, it follows that the structure should be capable of SR regime in the range of absorber bias voltages 20-30 V for the pump current amplitude up to *390 mA*, at the boundary corresponding to quenching of the Q-switching regime. However no such indications appear in the pulse shape and peak power. This might be attributed to two possible reasons: (i) insufficient temporal resolution or too low pump current. At higher currents, such as 430 mA, the quenching of Q-switching regime is expected to occur at absorber bias of 30-35 V, which is above the breakdown voltage. The solution can be found in increasing the length of absorber.

Interestingly, the average power in Fig 6.26 follows the threshold current and slope efficiency dependences (Fig. 6.27). The average power maximum and lowest threshold current are observed at the absorber bias in the range 10-12 V, corresponding to the flat band conditions. The slope efficiency drops at such absorber bias. These indicates (see Eq.(6.1)) that the absorber reveals the lowest modal absorption at 10-12V bias. In the range 0 to 10 V of absorber reverse bias, the absorption does not varies monotonically, while at higher reverse biases, it constantly increases in agreement with CW measurements in section 4 .

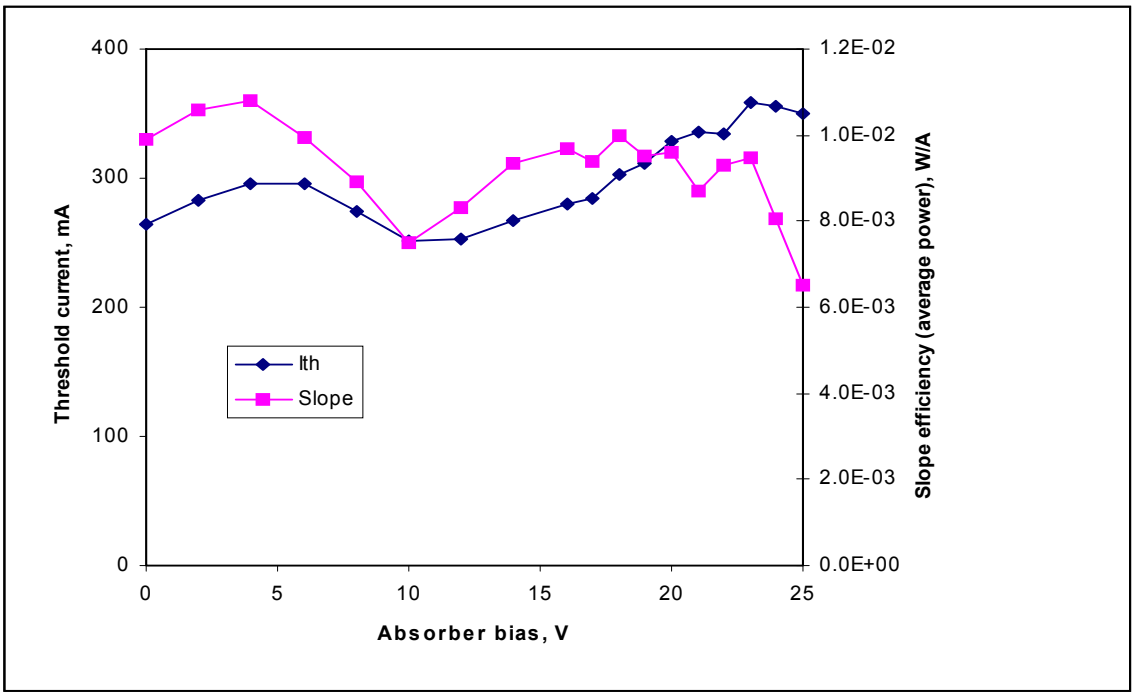

Fig. 6.27. Threshold current (left axis) and average-power slope efficiency (right axis) in function of absorber bias in A1902 (laser #I). Structure is driven by 20 ns current pulses with repetition period 550 ns superimposed on DC pre-bias current of 65 mA.

The self-pulsations (or Q-switching) operation regime was observed at reverse absorber bias exceeding 18 V. In the range 14-18V excitation of damped relaxation oscillations has been observed. The pulse width is plotted in Fig. 6.28 as a function of the absorber bias. With increasing current pulse amplitude applied to the gain section, the pulse width decreases. In the studied range of absorber bias, at the current amplitude 417 mA or higher, the pulse width remains constantan, clamped at 210ps. Since the peak power is also constant (Fig. 6.26), the decay of the average power seen in (Fig. 6.26) is caused by increase of the period between the pulses. Such behaviour is typical for the self-pulsations or Q switching regime. Indeed, the pulse repetition rate shows typical increase in function of the pump current excess above threshold

(Figure 6.29). With increasing absorber bias above the flat band conditions, the threshold current growths (see Fig 6.27), yielding a reduction of the pulse repetition rate seen in Fig. 6.29.

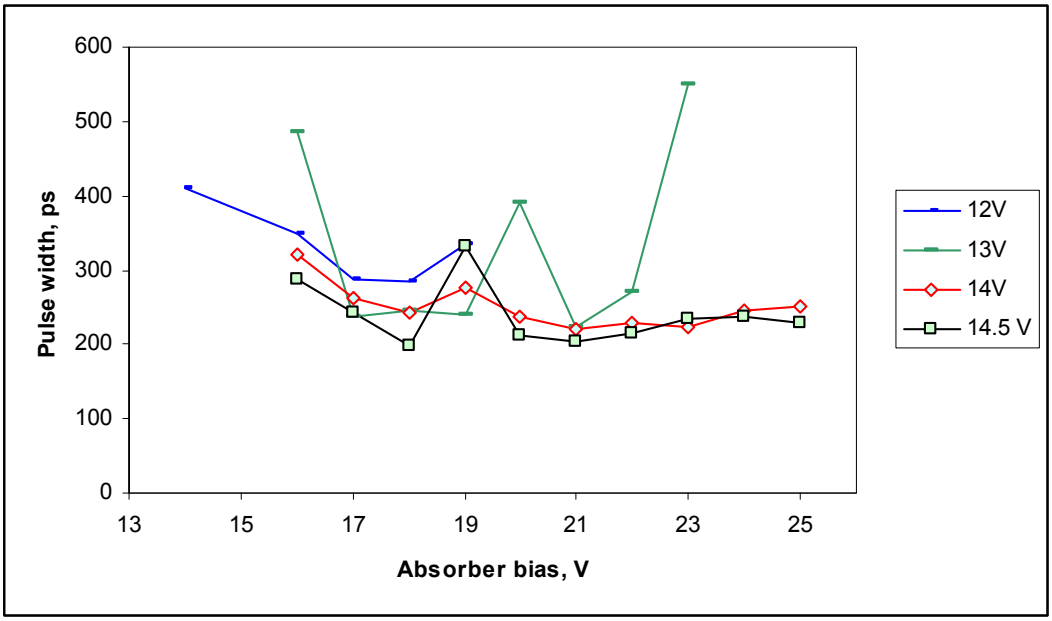

Fig.6.28. Pulse width in self-pulsations (Q-switching) or relaxation oscillations regime in function of absorber bias in A1902 (laser #I). Structure is driven by 20 ns current pulses superimposed on DC pre-bias current of 65 mA.

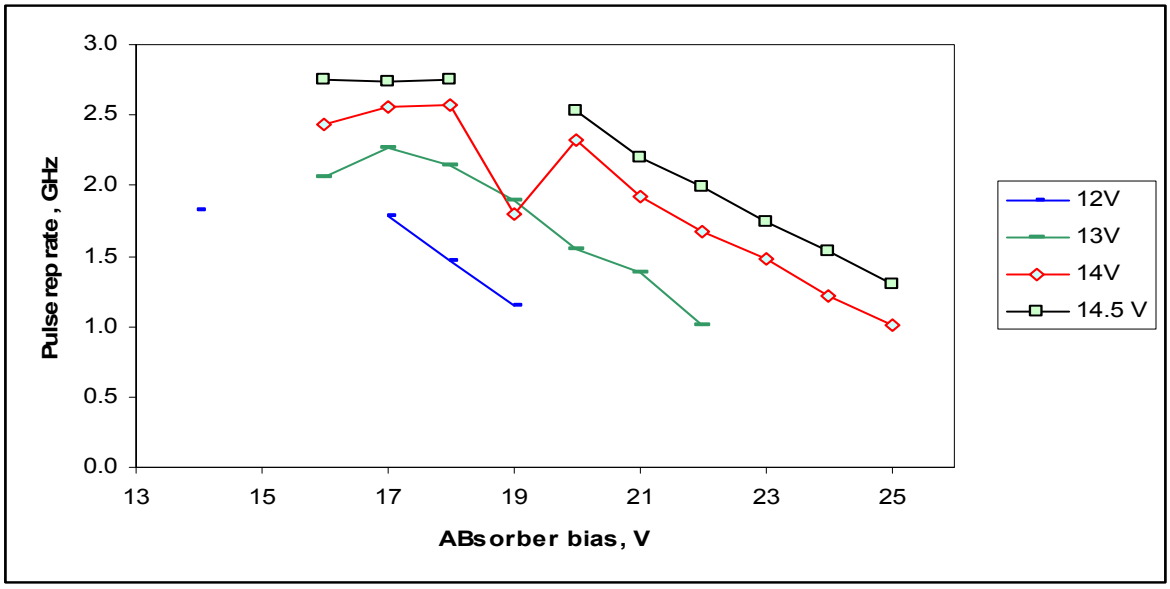

Fig. 6.29. Pulse repetition rate in Q-switching or relaxation oscillations regime in function of absorber bias in A1902 (laser #I). Structure is driven by 20 ns current pulses superimposed on DC pre-bias current of 65 mA.

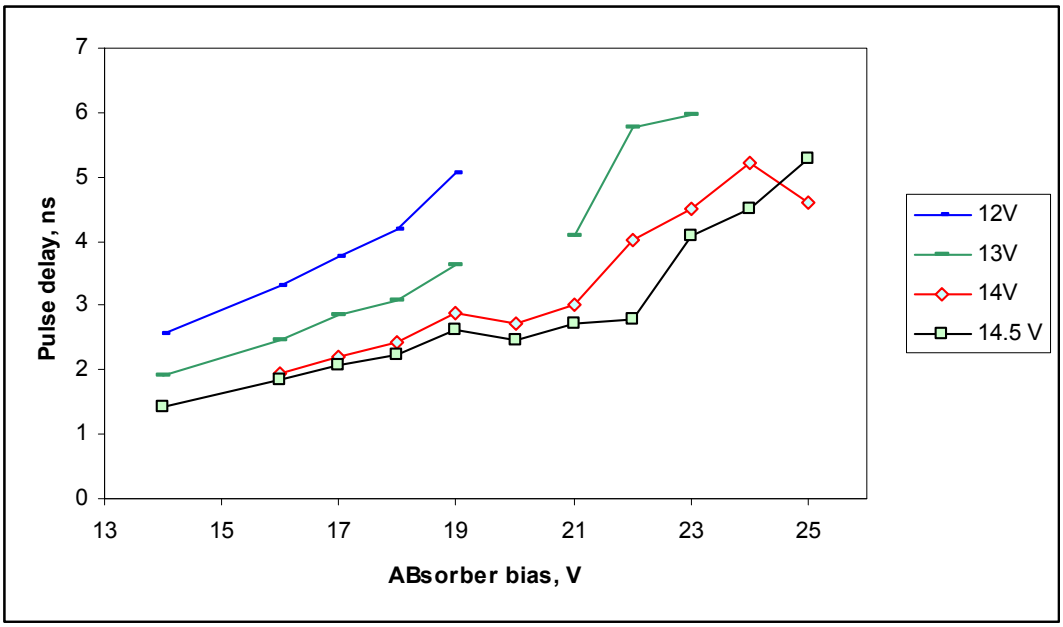

Fig.6.30. Pulse delay in gain switching, Q-switching or relaxation oscillations regime in function of absorber bias in A1902 (laser #I). Structure is driven by 20 ns current pulses superimposed on DC pre-bias current of 65 mA.

Fig. 6.30 shows measured delay time to emission of the first lasing pulse from the rising front of the current pulse. Interestingly, the both delay time and period of the pulses increases with applied reverse bias. On one side , this feature enables solitary pulse production in the pulse-on-demand mode. On the other hand, large delay to emission of pulse enables accumulation of carriers in the gains section, which is important for reaching the SR regime. In particular sample, an accumulation time of 6 ns has been reached, which is expected to be sufficient for SR regime. An attempt to operate the structure under 1 ns current pulses was not successful because of the large delay to the pulse emission.

Interesting features are observed in the optical spectrum. The signature of (longitudinal) multimode emission with stochastic envelope of spectrum are seen under small bias, in the gain switching regime (red region in Fig 6.25). With increasing the absorber reverse bias and transition to the dumped relaxation oscillations (blue region) and then to self-pulsations or Q-switching regime (yellow region), the stochastic envelope is replaced by well defined periodic pattern. Clearly visible periodic clusters of modes are spaced by 0.22 nm, while no modes are excited in between. Such spectral modulation is typical for Q-switching regime or mode-locking regime with Q-switching envelop. The frequency splitting of the adjacent mode clusters is of 390 GHz, which corresponds to the mode separation in a Fabry-Perot cavity of the length 110 μm (in GaN). The origin of such modulation can be attributed to reflections of the interface between the gain and absorber sections.

The measured shift of the peak emission wavelength in function of the absorber bias is shown in Fig. 6.31. It is significantly different as compare to the wavelength shift in CW operating devices. In particular, it is difficult to interpret it in terms of the expected blue shift of the lasing mode with increasing cavity loss and absorption. This might be caused by ambiguity in defining the peak wavelength in a spectrum composed of the mode clusters as well as by the fact that in the gain switching regime or regime with excited dumped relaxation oscillations, the width of the psectrum is smaller compare to selfpulsations of Q-switching regime.

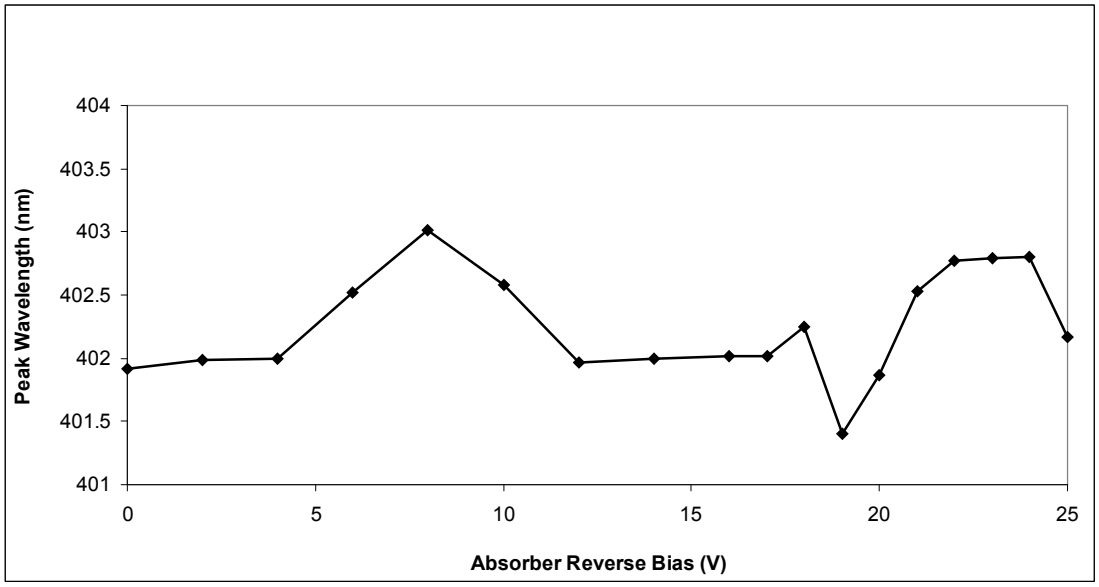

Fig. 6.31. Peak emission wavelength in function of absorber bias in A1902 (laser #I). Structure is driven by 20 ns current pulses superimposed on DC pre-bias current of 65 mA. (Spectra are systematically blue- shifted by 6 nm as a result of an error in operating the spectrometer.)

In summary the narrow QW structure have shown large threshold current, long delay to the pulse emission and withstand reverse bias up to 20 V. These features are attractive for SR emission. However the absorber length needs to be increased in order to shift the Q-switching quenching region in the range of lower absorber biases (below 20V) to avoid the break-down damage of the absorber. The pulse width of 210 ps and peak power of 70mW have been achieved in regime of selfpulsations (Q-switching). In narrow QW structure A1902 the flat band condition occurs at 10V negative bias. The dynamic regimes in the range of biases 0-10V and 10-20V are significantly different, which might be caused by reduction of the absorber recovery time with reverse bias.

6.4.3.2 A2109 structure, 20 ns current pulse

Technically, the growth run A2109 differs by thicker QWs and optimized p doping. The number of QWs is the same as in A1902. Possibly due to the impact of the substrate quality variations, the material losses in A2109 are lower.

Wider QWs resulted in better carrier capturing into the QWs. This together with the smaller material loss yielded lower threshold current. The optimized p doping resulted in a reduced voltage drop across the structure so as no DC pre-bias was needed to operate under 20 ns current pulses. However without pre-biasing of the gain section, the output power was reduced as compare to A1902 and it was not possible to use 50 GHz bandwidth detector with 50 Ohm transimpedance. Instead of it, a slower detector with the transimpedance 1KOhm and bandwidth 12 GHz (30 ps response time) was used. The reduced bandwidth have no impact on detected pulse parameters in the gain switching, damped relaxation oscillations and Q-switching regimes, making thus possible a direct comparison with the performances of A1902 sample.

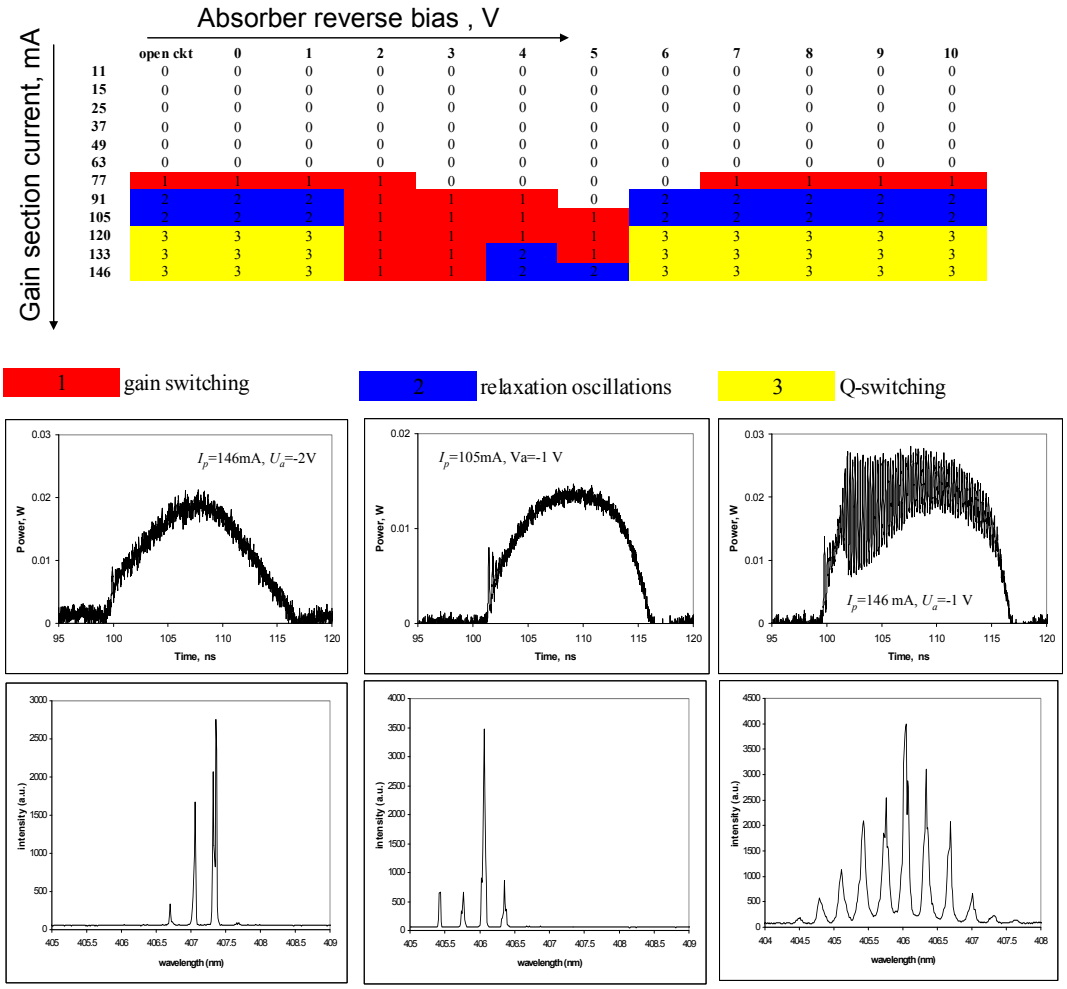

Fig. 6.32. Map of dynamic regimes in A2109 (laser #21) in function of absorber bias (Volts, horizontal axis) and current pulse amplitude applied to the gain section (mA, vertical axis). The gain section is driven by current pulses of the width 20 ns and repetition period 550 ns. The map shows dynamic regimes of gain switching (1), relaxation oscillations (2), Q-switching (3). Panels in the middle indicate typical pulse shape for each regime. The corresponding optical spectra are shown in the bottom panels. (Spectra are systematically blue--shifted by 6 nm as a result of an error in operating the spectrometer.)

The particular device described below (laser #21) has the cavity length 800 μm with the length of absorber section 100 μm and the width of the ridge waveguide 2 μm. The cavity design is thus close to the one of laser #I reported in previous subsection.

As in A1902, the dynamic regimes of the gain switching, damped relaxation oscillations and Q-switching are observed. The A2109 structures with wider QWs and improved p-doping have shown smaller lasing threshold and no need to apply a d.c. pre-bias. However, it has been noticed that unrecoverable degradation occur at a smaller reverse bias applied to the absorber as compared with A1902. Therefore in these measurements, the absorber bias is limited to -10 V.

In Fig. 6.32, Q-switching regime exhibits widest spectrum, as in A1902. The optical spectrum in all lasing regimes exhibit periodically spaced lasing mode clusters. Their splitting of 0.3 nm corresponds to the Fabry-Perot effect in the 80 μm long cavity (in GaN) formed by reflections of the output laser facets and of the gain – absorber section interface. The difference from the

nominal length of the absorber section can be attributed to imperfections of fabrication, in particular to the ones introduced by laser facet cleave.

In distinguishing from the sample A1902, in A2109 devices, both the average and peak power (figure 6.33) exhibits large sensitivity to the absorber reverse bias. The flat band conditions measured in CW regime occurs at the absorber reverse bias of about -10 V (see section 4), at which both average and peak power have maxima. On the other hand, these two parameters

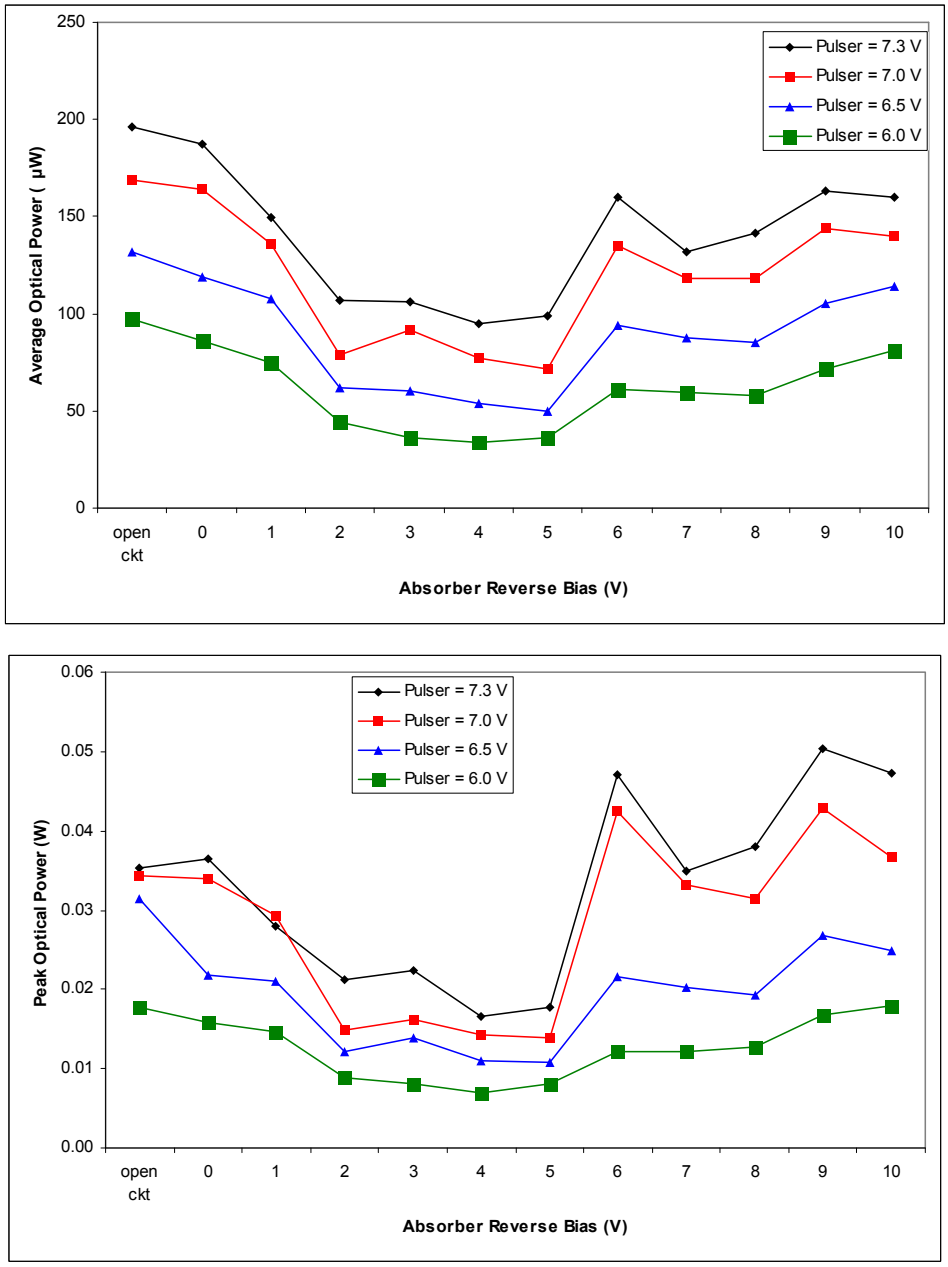

Fig. 6.33. Average power (top panel) and peak power (bottom panel) in function of absorber bias in A2109 sample (laser #21). The gain section is driven by the current pulses of the width 20 ns, repetition period 550 ns and amplitudes 7.3 V (146 mA), 7 V (133 mA) 6.5 V (120 mA) and 6V (105 mA).

exhibit local minima at the reverse bias 3-5 V. Moreover, the threshold current defined from the linear part of L-I curves and the slope of the L-I curves show complimentary maximum and minimum in the range of 3-5 V (Fig.6.34). In distinguishing from the A1902 sample, the A2109 devices show tendency to relaxation oscillations and Q-switching self pulsations in the range of small (~0-2 V) absorber reverse bias (compare Figs. 6.25 and 6.32).

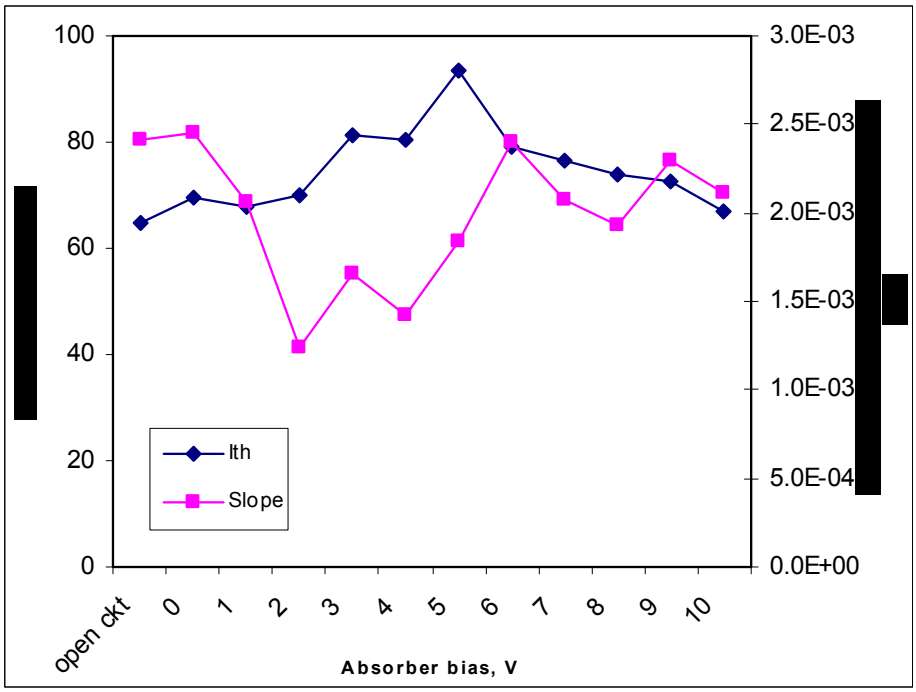

Fig. 6.34. Threshold current (left axis) and slope efficiency (right axis) in function of absorber bias in A1902 (laser #I). Structure is driven by 20 ns current pulses superimposed on DC pre-bias current of 65 mA.

To interpret such difference, a map of regimes has to be analyzed in function of the differential absorption to gain ratio σ (see Table 3.6 of Sec 3.5), carrier lifetime in the gain section QW τ_n and recovery time of absorber τ_a defined by the tunnelling time of carriers form the absorber QWs to the barriers and by the drift time through the i-region of the structure. An analysis have shown that it is convenient to map the dynamic regimes in the coordinates of

$$\Delta = \frac{\tau_a}{\tau_n}\sigma - 1, \quad Q_0 = \frac{\Gamma \alpha \sigma g_0 (1 - V_a)}{v_g (\alpha_i - \ln(R)/L)} \tag{6.4}$$

where Q_0 is the small signal absorption normalized on cold cavity loss. The regions of stable CW, bistable CW (below switching-"On" threshold) and unstable CW (self-pulsations, Q-switching, mode-locking) for two samples are depicted in Fig. 6.35. They are obtained by analyzing stability of all CW lasing solutions with respect to Routh-Huwitz criterion. The points in the map show location of the dynamical system at zero absorber bias (0V), flat band conditions (12 and 10V for samples A1902 and A2109 respectively) and, finally its location at reverse absorber bias exceeding the flat band bias. The arrows indicate a path that the system undergoes with increasing reverse absorber bias. These are in agreement with the measured dynamic maps in figures 6.25 and 6.32.

A1902 A2109

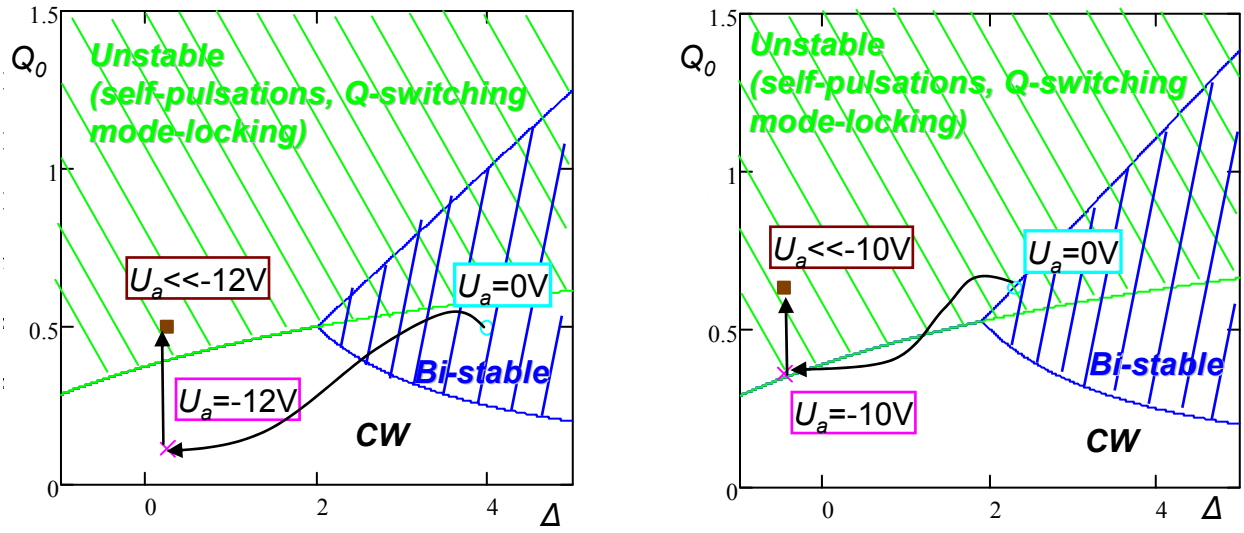

Fig. 6.35. Map of calculated dynamic regimes in A1902 (left) and A2109 (right) samples showing stable CW region, unstable CW region above the switching-"On" threshold and bi-stable CW region below the switching –"On" threshold. The maps are plotted in coordinates from Eq.(6.4).

Peculiar difference in the sequence of dynamic regimes observed with increasing absorber bias in the two samples is attributed to the fact that due to higher loss in A1209 (see table 3.6 of Sec 3.5), it operates at higher carrier density and smaller carrier lifetime in the gain section QWs τ_n. As such, it operates at higher Δ and lower Q_0 and shows smaller tendency to self-pulsations, Q-switching or mode-locking at the flat band conditions. This can be corrected by increasing the length of absorber and thus shifting the dynamic regimes upwards. On another side, A1902, exhibit higher contrast of Q_0 variations with the absorber bias. Thus for SR regime, narrow QW structures with long absorber section will be preferable, while for mode-locking regime wider QW structures, also with longer absorber are preferable.

As can be seen from the measured average power in Fig.6.33, the modal absorption decreases non-monotonically in the range from zero absorber bias to the bias compensating the internal piezoelectric field (flat band conditions). The modal absorption reaches a local maximum at 3-5 V. This is also confirmed by a blue shift of the lasing mode envelope at 4 V bias (Fig. 6.36), indicating that the average modal gain is clamped at a higher photon energies in order to compensate for the increased overall cavity losses. (Due to the band filling effect, the spectral peak of the gain curve blue shifts with increasing carrier density.) These features are reproduced in Fig. 6.35 by wavy arrows indicating the dynamic system trajectory from zero bias to the flat band conditions. In particular they reproduce a region of small absorber reverse bias voltages in A2109 sample were self-pulsations (or Q-switching) have been observed. The A2109 samples exhibit self pulsations in the range of reverse biases around flat band conditions and around zero bias (as opposed to A1902) due to smaller material losses leading to higher Q_0, longer effective carrier lifetime τ_n in the gains section QWs and lower Δ. The slope efficiency in A2109 devices obtained by measuring the average power v.s pump current (Fig.

6.34, right axis) is lower than in A1902 devices since A2109 were operated without pre-biasing of the gain section. In both A1902 and A2109 devices, the average power measured with non-contacted absorber (open circuit) is higher than in the case of 0 V source connected to absorber (short circuit operation.) This indicates that (i) the absorber effectively impacts the lasing characteristics and that (ii) in the open circuit configuration, the recovery time of absorber is longer and limited by the carrier lifetime in the QWs. In the short circuit configuration (zero bias) or under a negative bias, the carrier tunnelling from the QWs to the barriers and drift through the i-region of the structure become important.

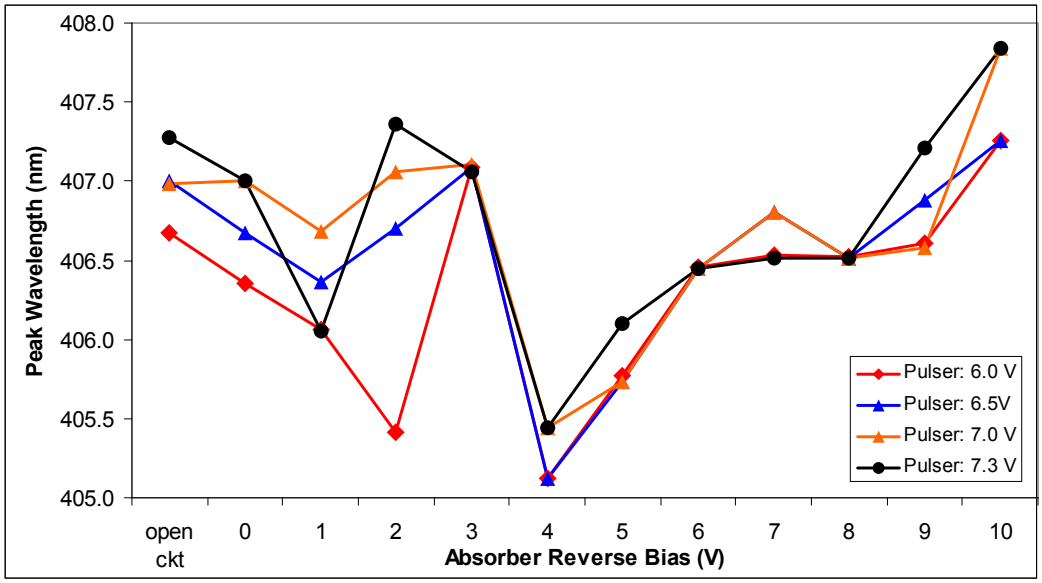

Fig. 6.36. Peak emission wavelength in function of absorber bias in A1902 (laser #I). Structure is driven by 20 ns current pulses superimposed on DC pre-bias current of 65 mA. (Spectra are systematically blue- shifted by 6 nm as a result of an error in operating the spectrometer.)

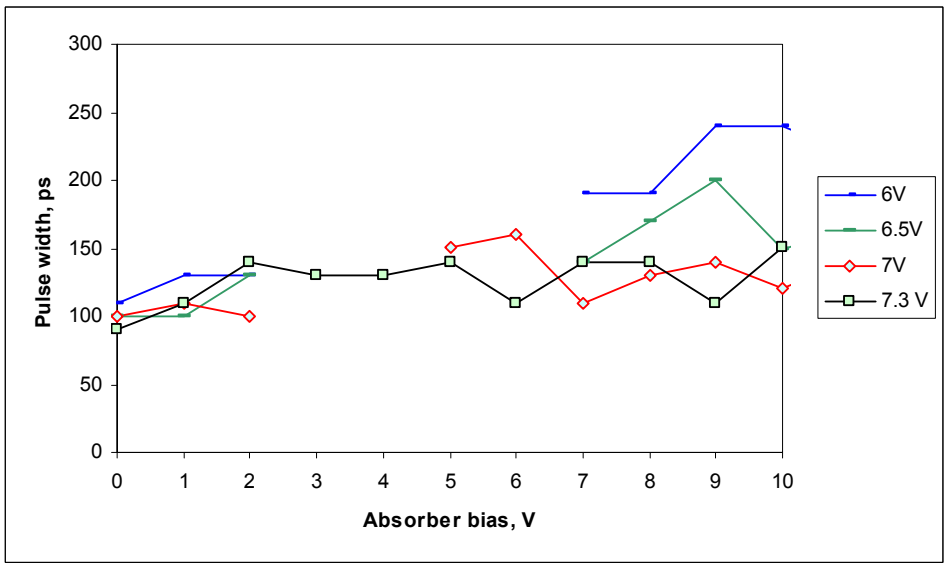

Fig. 6.37. Pulse width in Q-switching or relaxation oscillations regime in function of absorber bias in A2109 (laser #21 Structure is driven by 20 ns current pulses of different amplitude.

The peak lasing wavelength in A2109 shows larger variation with the absorber bias as compare to A1902 (Fig 6.36). This might be attributed to lower material losses and hence higher impact of absorber (larger Q_0 in Fig.6.35).

In both domains of Q-switching in the sample A2109 (Fig. 6.37), the pulse width decreases with increasing current amplitude at the gain section. The shortest pulse width achieved is slightly below 100 ps, that is smaller than in A1902 devices.

As in the case of A1902 device, the delay time to emission of the optical pulse in A2109 sample (Fig 6.38) is in agreement with variations of the absorption level of absorber, as exchibited by the threshold current variations in Fig.6.34. As expected, it is anticorrelated with the average power variations (see figure 6.33). Note however that the measured threshold current is the same at 0 and 10 V bias of reverse bias, while the average power is higher at 10 V and the delay time to the pulse emission is shorter at 10V. This allows to assume that the carrier leakage from the gain section or carrier generation in the absorber section of A2109 devices (via avalanche multiplication) might prevents the efficient operation of absorber at high reverse biases. This conclusion is also confirmed in measurements of the pulse repetition rate (see Fig. 6.39).

The pulse repetition rate (in Q-switching or relaxation oscillations regime) increases with the pump current. However there is no impact of changing the reverse absorber bias in the range from 6 to 10 V. Interestingly, the repetition rate at small absorber biases (0-2 V) is higher than at large bias. This can be attributed to longer absorber recovery time (and hence its stronger saturation) at small reverse biases, which is in agreement with dependence shown in Fig 6.20. Finally note that the measured leakage current in absorber with no current pulses applied to the gain section indicates a leakage resistance of 15 kOhms.

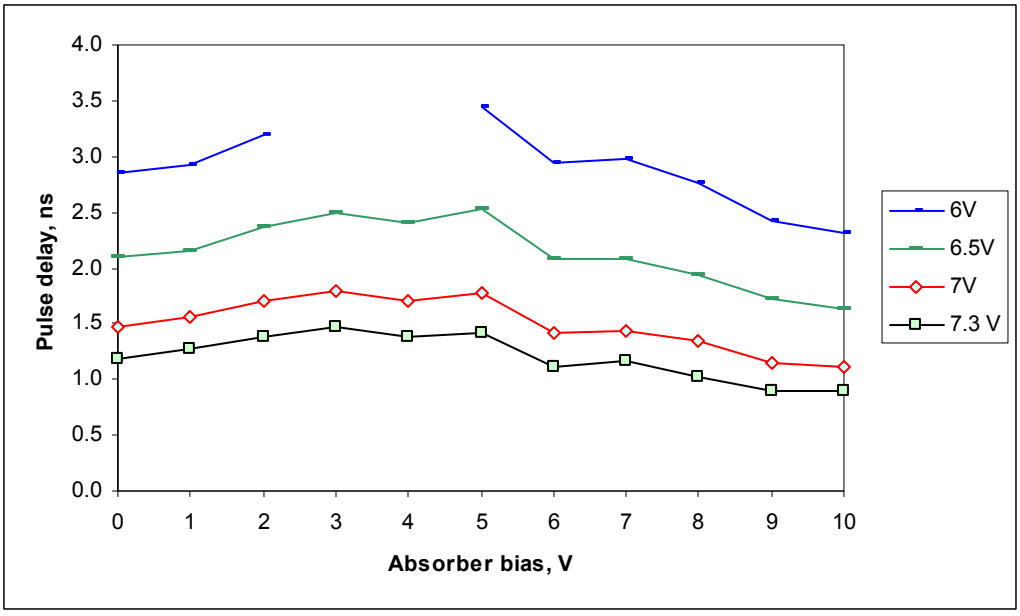

Fig. 6.38. Pulse delay in gain switching, Q-switching or relaxation oscillations regime in function of absorber bias in A2109 (laser #21 Structure is driven by 20 ns current pulses of different amplitude.

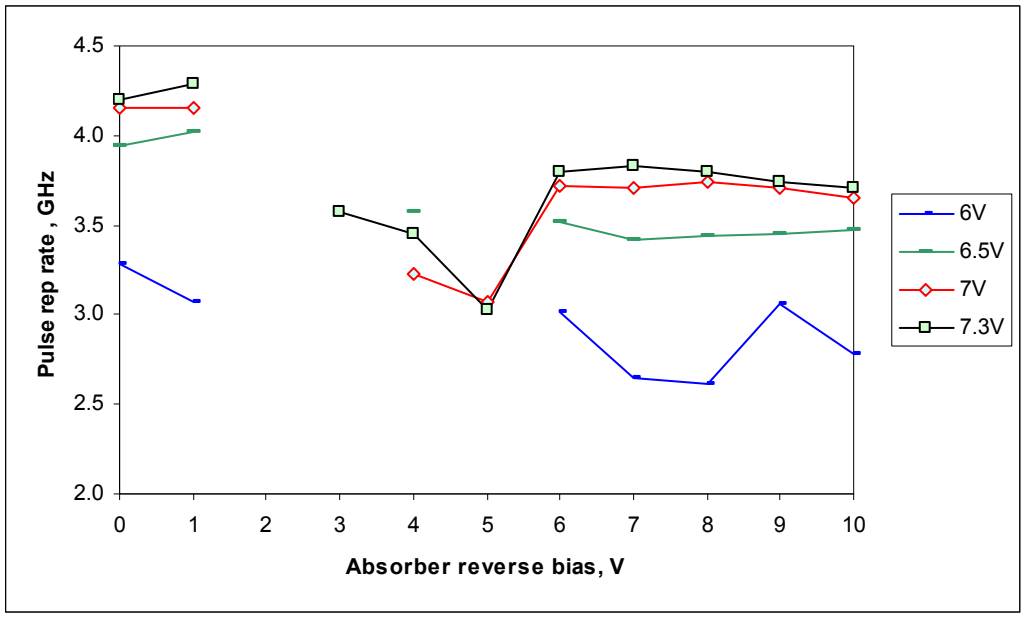

Fig. 6.39. Pulse repetition rate in Q-switching or relaxation oscillations regime in function of absorber bias in A2109 (laser #21 Structure is driven by 20 ns current pulses.

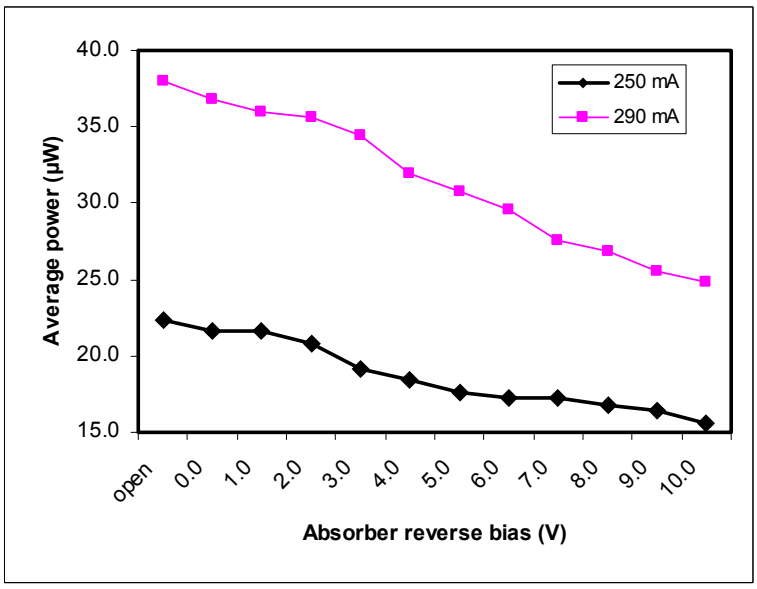

Fig. 6.40. Average power in function of absorber bias in A2109 sample (laser #21). The gain section is driven by the current pulses of the width 0.8-1 ns, repetition period is 550 ns and amplitudes 250 or 290 mA.

6.4.3.3 A2109 structure, 800 ps current pulse

From the oscillation frequencies in Fig 6.39, it follows that the absorber recovery time is at the scale of ~1 ns for small absorber bias (see also Fig 6.20). To avoid the impact of long recovery time of absorber, the structure A2109 was tested under current pulses of sub nanosecond width, that is shorter than the recovery time of absorber. In this regime, it was possible to operate at higher gain section current. Although this pumping regime is not suitable for mode-locking oscillations, it can be applied for SR emission. As indicated by measured average power in Fig 6.40, it was now possible to observe the lasing quenching effect of absorber (compare to Fig. 6.33).

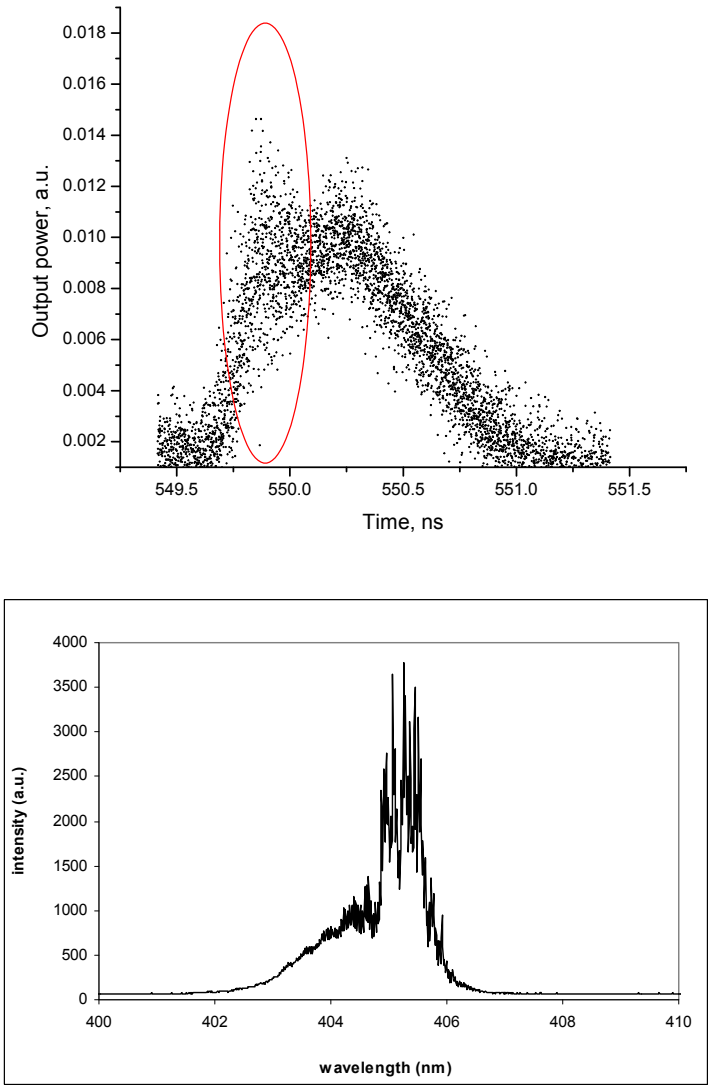

Fig. 6.41. Output pulse shape detected on sampling scope (top) and optical spectrum (bottom) under excitation by the current pulse of the width 0.8-1 ns, repetition period is 550 ns and amplitude 284 mA.

The linear extrapolation of the average power vs absorber reverse bias indicates that lasing will be quenched at absorber bias in the range 30-40 V. In this range, the SR emission can be observed. Unfortunately, this voltage exceeds the break down voltage of the absorber.

An attempt to operate at high reverse absorber biases has resulted in a failure of the absorber wire bonding, indicating a high current of the absorber. Simultaneously, a degradation of the structure has been observed resulted in increased threshold. However the generated optical pulse has now revealed new interesting features: the increase of the noise at the rising front of the optical pulse (jitter) and red shifted emission spectrum (Fig. 6.41). These features might be attributed to the onset of SR regime.

Further increase of the pump current resulted in disappearing of the pulse jitter and transition to the lasing in gain switching regime. (It was not possible to apply a negative bias at absorber after the wire bondfailure).

Several other devices has been tested in conditions that are expected to be suitable for SR regime. No other indications of SR emission have been observed in these devices. A rapid degradation of DUTs was observed under nanosecond current pulses and high reverse bias applied to absorber.

6.4.4 Conclusion

These results allow the following conclusions and summarising remarks to be made:

- Single transverse mode design of ridge waveguide (2 μm width) enables better control of the lasing characteristics with absorber bias. 3 μm width
- For SR regime, narrow QW structures with long absorber section will be preferable, while for mode-locking regime wider QW structures with longer absorber should be used.
- All devices shows Q-switching regime at sufficiently high current and absorber biased above the flat band conditions. Devices utilizing wider QWs (A2109 sample) show lower threshold and have a tendency to operate in Q-switching regime even in the range of absorber bias close to 0 Volt.
- The optical spectrum shows lasing mode clusters due to reflections of the gain- absorber section interface.
- The absorber recovery time in wide QW devices (A2109) is relatively long. The origin can also be related to the processing and not only to the difference in the QW structure. For SR regime, this can be compensated for by operating with nanosecond current pulses.
- Low output power has not allowed the autocorrelation measurements of the pulse width to be conducted.
- Wide QW devices (A2109) have revealed smaller pulse width of generated Q-switched pulses (~100 ps).
- Higher peak power of ~ 70 mW was achieved in narrower QW devices (A1902) using pre-biasing of the gain section.
- For the same length of absorber (10-12 %) , wider QW devices require higher absorber reverse bias voltage (~30-40V in A2109 vs 20-30 V in A1902) in order to operate in SR regime. The required bias is above the avalanche breakdown. To reduce the absorber bias, longer absorber section should be used.

- To avoid rapid degradation of devices under nanosecond current pulses a dc pre-bias of the gain section has to be used.
- Sensitivity of equipment used in time-resolved measurements has to be increased.

6.5 Self-pulsation and single-pulse generation

Self-pulsating operation is investigated in GaN-based multi-section laser diodes with different absorber lengths. To characterize the self-pulsation characteristics, they are pumped with 100 ns electric pulses at a repetition frequency of 10 kHz and the output is measured with a streak camera. The pulsation frequencies are determined from 10 ns-long traces each, while the pulse widths are measured at 20 Hz repetition rate in single-shot mode with a time window of 500 ps, which has a temporal resolution of 5 ps. Figure 6.42 shows the time evolution of the output of two multi-section laser diodes with 4.5nm wide QWs, 3 µm ridge width and 800 µm cavity length with a 50 µm absorber and a 100 µm absorber at different gain section currents. For the device with the short absorber, stable self-pulsation is observed in a bias range from 0V to -9V and up to twice the threshold current, whereas the device with 100 µm absorber exhibits a transition to cw emission at a current of about 190 mA, at 0 V bias. This transition shifts to higher current when the negative bias is increased. The initial pulse of each pulse trail is always considerably higher than the subsequent pulses and slightly red-shifted. This is a consequence of the switching of the absorber from empty state to partly saturated state. The emission spectrum in self-pulsating operation is about 2 nm brod, which is considerably broader than the typical emission of comparable single section devices.

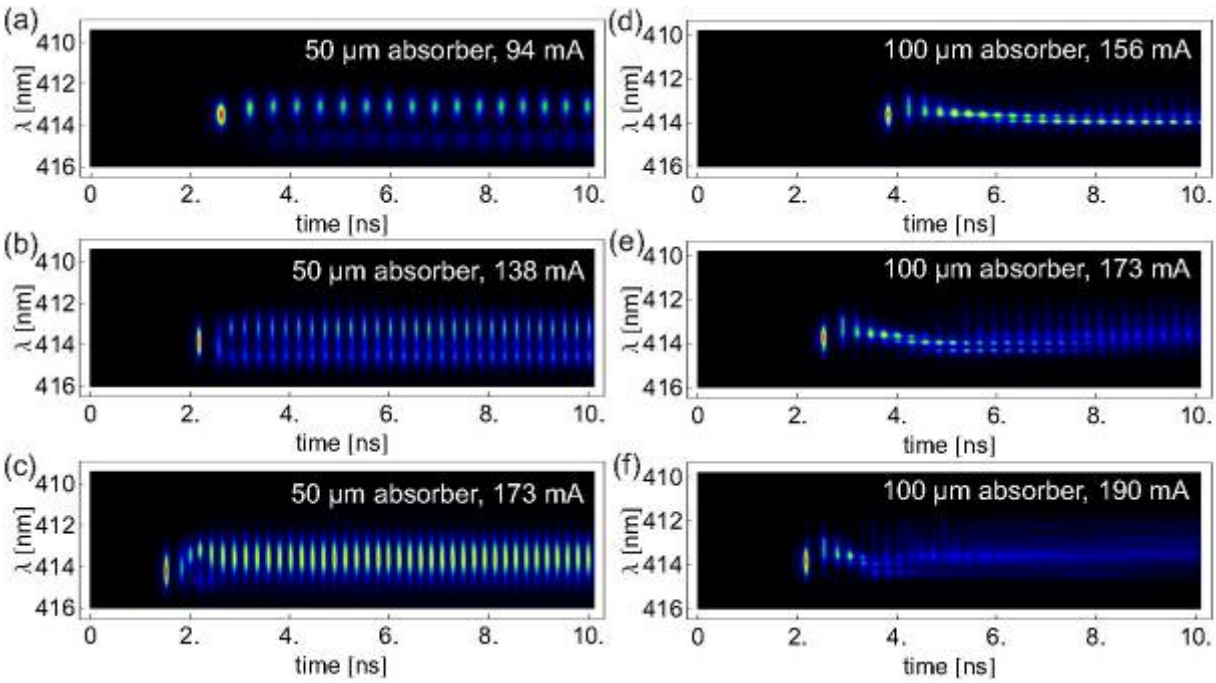

Fig. 6.42 *Example streak camera traces of self-pulsation at 0V absorber bias from a multi-section laser diode with 50 µm absorber at 94 mA (a), 138 mA (b), 173 mA (c) gain section current and from a sample with 100 µm absorber at 156 mA (d), 173 mA (e), 190 mA (f).*

Remarkably, the self-pulsating operation in both devices is stable over a wide range of gain currents and absorber bias voltages, in agreement with Fig 6.35. Although previous theoretical studies predict continuous-wave operation for the measured values of modal absorption and charge carrier lifetime [Mir99, Nak97].

As Fig. 6.43 shows, the oscillation frequency of both devices increases monotonically within a range of 1.5 to 5 GHz with increasing current. For the 50 µm absorber, a comparison of the dependency of the oscillation frequencies on pump current and absorber bias with the average output power reveals that the self-pulsation frequency goes as the square root of the output power, just like the frequency of relaxation oscillations. Therefore, the occurrence of self-pulsation can be attributed to a stabilization of relaxation oscillations by the saturable absorber. At low currents, the device with the 100 µm absorber behaves similarly, but a transition to cw operation with initial relaxation oscillations occurs at higher current, and the frequency of these relaxation oscillations depends rather linearly on the pump current. The dependency of the self-pulsation frequency on pump current observed in this work differs from the behaviour reported in Refs. [Miy09] and [Wat10], where an almost constant pulsation frequency around 1 GHz was obtained. However, it is known from other material systems that the pulsation frequency depends on the active region design, in particular on the magnitude of doping in the quantum wells and barriers [Tan98].

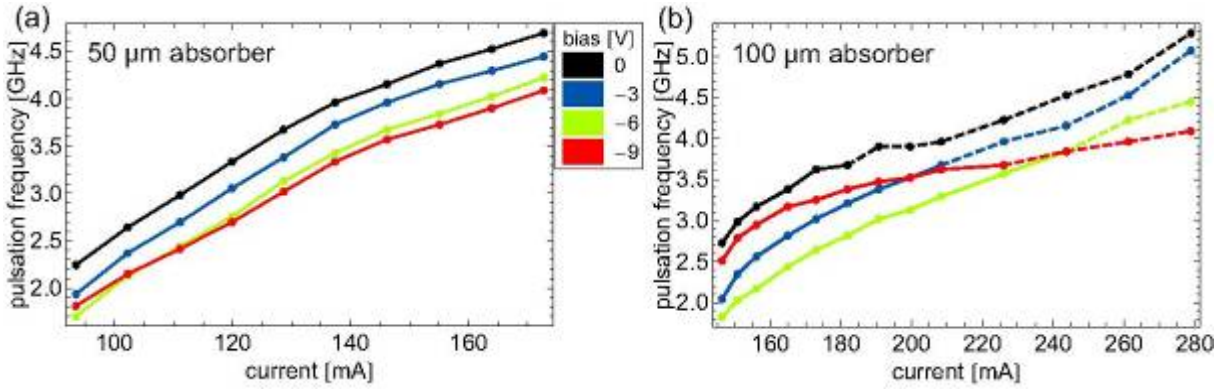

***Fig. 6.43**: Oscillation frequency as a function of pump current for different bias voltages for the multi-section LD with 50 µm absorber (a) and 100 µm absorber (b). The dashed lines in (b) indicate the current range where the oscillations become unstable.*

The width of the initial pulse decreases as a function of current, reaching a plateau of 18 ps at 173 mA and zero absorber bias for the 50 µm absorber and 21 ps at 283 mA for the 100 µm absorber (see Fig. 6.44). With increasing negative bias the pulses become longer, indicating that the pulse width depends in fact mainly on the value of the absorption coefficient in the absorber section. This finding is in qualitative agreement with the simulation results presented in section 3. Comparing the absorber lengths, one finds that the device with the longer absorber exhibits a longer pulse width even at much higher current.

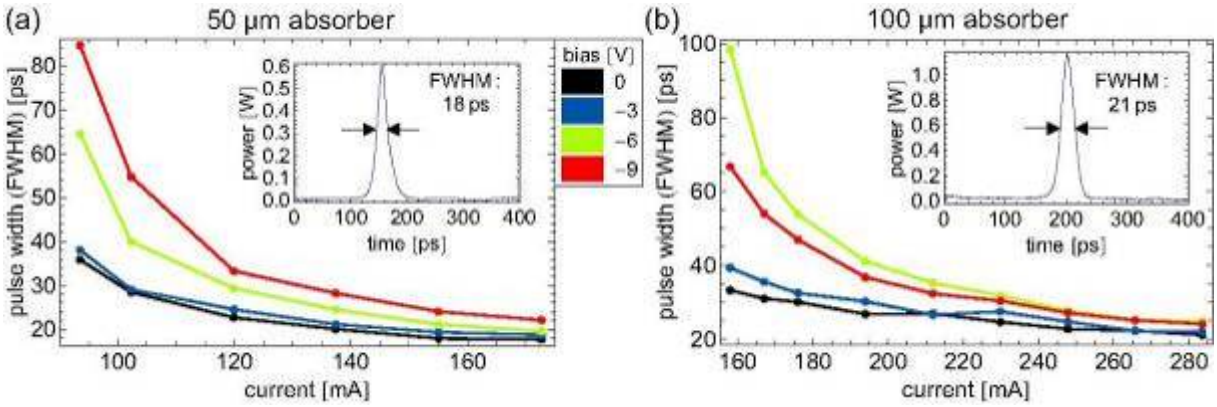

Fig. 6.44 *Width of initial pulse as a function of pump current for different bias voltages for the multi-section LD with 50 µm absorber (a) and 100 µm absorber (b). The insets show the pulse shape at 173 mA (a) and 283 mA (b), respectively, and 0 V bias voltage.*

Single pulses are generated without a loss of peak intensity simply by reducing the duration of the electric excitation pulse to a value between 0.5 to 2 ns, depending on the pump current. The peak power of the pulses is then determined by measuring the average output power and dividing by the product of the repetition frequency (10 kHz) and the pulse width (see Fig. 6.45). The maximum peak power is 0.60±0.05 W at 173 mA pump current for the 50 µm absorber and 1.1±0.1W at 283 mA pump current for the 50 µm absorber, both at 0V absorber bias voltage. The corresponding maximum pulse energies for both devices are 11±1 pJ and 23±2 pJ, for the 50 µm and 100 µm absorber, respectively. Even though the device with the longer absorber does not exhibit stable self-pulsation at high currents, it is suitable for single pulse generation, as the first spike has a proper shape (see inset of Fig. 6.44b). The maximum achieved peak power is almost twice the value measured for the device with short absorber, and the pulse width is only 3 ps longer. A longer absorber thus provides a higher peak power, at the cost of a slightly increased pulse width.

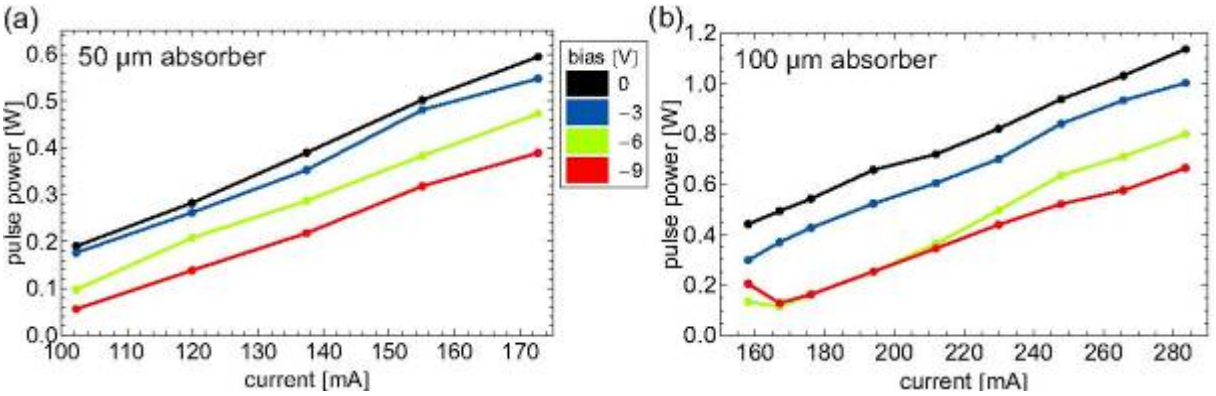

Fig. 6.45 *Peak power of single pulse as a function of pump current for different bias voltages for the multi-section LD with 50 µm absorber (a) and 100 µm absorber (b).*

6.6 Conclusion with respect to objectives of WP5 in phase 2

This section is a contribution to the objective of WP5 “Tests and evaluation of multisection laser structures”. The study of the performance of the preliminary set of multiple contact lasers fabricated by the Consortium has been carried out in active/passive mode locking and superradiant regimes.

We observe very-fast self-pulsations (see Sec.6.1 above), which can be attributed to passive mode locking regime. However the observed discrepancy in the pulse period and clustering of the mode spectrum in Q-switching mode-locking and Q-switchign regimes requires an additional experimental studies in new devices of Phase 3.

One sample with degraded absorber has revealed features that can be interpreted as signature of superradiance regime. However, these have not been reproduced so far in other samples of preliminary lasers.

All studies reported here have revealed that the lengths of the absorber sections of the fabricated devices proved to be too short. The controllable (by reverse bias) absorption was small for the generation of ultrashort pulses..

The next set of the devices which are under fabrication by the Consortium will have longer absorber sections (up to 40%). The investigation of the dynamic regimes of the new lasers will be continued in Phase 3.

The present experimental study has also shown that the fast degradation of the samples prevents c.w. measurements. This makes the task on achievement of the reliable and reproducible experimental results to be quite challenging. However we shall clarify that the device lifetime issue related to rather stabilization of a technology is considered at the moment as the minor task of the project, which is focused on research into physics and dynamics of InGaN/GaN multiple section lasers with the objective to reach expected devices performances.

7. Dissemination and exploitation (WP6)

Below we provide a list of the relevant publications and presentations from Femtoblue consortium, published during the first phase of the project:

JOURNALS

1. W. G. Scheibenzuber, U. T. Schwarz, T. Lermer, S. Lutgen, and U. Strauss, *Antiguiding Factor of GaN-based Laser Diodes from UV to Green*, Appl. Phys. Lett. **97**, 021102 (2010).

2. W. G. Scheibenzuber, U. T. Schwarz, L. Sulmoni, J.-F. Carlin, A. Castiglia, and N. Grandjean, *Bias-dependent absorption coefficient of the absorber section in GaN-based multisection laser diodes*, Appl. Phys. Lett. **97**, 181103 (2010).

3. W. G. Scheibenzuber, U. T. Schwarz, L. Sulmoni, J.-F. Carlin, A. Castiglia, and N. Grandjean, *Measurements of the Tunable Absorption in GaN-based Multi-Section Laser Diodes*, Physica Status Solidi (c), 8: n/a. doi: 10.1002/pssc.201000920.

4. W. G. Scheibenzuber, C. Hornuss and U. T. Schwarz, *Dynamics of GaN-based laser diodes from violet to green*, Proc. of SPIE 7953, 79530K (2011).

5. W. G. Scheibenzuber, U. T. Schwarz, L. Sulmoni, J. Dorsaz, J.-F. Carlin, and N. Grandjean, *Recombination coefficients of GaN-based laser diodes*, J. Appl. Phys. **109**, 093106 (2011).

6. D. L. Boiko, P. P. Vasil'ev, *Femtosecond superradiance in multiple-section InGaN/GaN quantum well laser structures*, arXiv:1103:5507.

7. I.V. Smetanin, P.P. Vasil'ev, and D.L. Boiko, *Theory of the ultrafast mode-locked GaN lasers in a large-signal regime*, arXiv: 1104.3336.

8. W. G. Scheibenzuber, C. Hornuss, U. T. Schwarz, L. Sulmoni, J. Dorsaz, J.-F. Carlin, and N. Grandjean, *Self-Pulsation at zero absorber bias in GaN-based multi-section laser diodes*, Appl. Phys. Express **4**, 062702 (2011).

9. J. Dorsaz, D. L. Boïko, L. Sulmoni, J.-F. Carlin, W. G. Scheibenzuber, U. T. Schwarz, and N. Grandjean, *Optical bistability in InGaN-based multi-section laser diodes*, Appl. Phys. Lett. **98**, 191115 (2011).

CONFERENCES

1. U.T. Schwarz, *(Al,In)GaN Laser Diodes*, invited paper at 19th Workshop on Heterostructure Technology (Crete, Grece, October 18-20, 2010), 4 pages.

2. D.L. Boiko, and P. P. Vasil'ev, *Dicke superradiance in GaN quantum wells*, submitted to 22d IEEE International Semiconductor Laser Conference (Kyoto, September 26-30, 2010), 2 pages.

3. W.G. Scheibenzuber, U.T. Schwarz, T. Lermer, S. Lutgen and U.Strauss, *Antiguiding Factor of Nitride Laser Diodes from UV to Green*, International Workshop on Nitride semiconductors IWN 2010 (Tampa, Florida, September 19-24, 2010), 1 page.

4. W.G. Scheibenzuber, U.T. Schwarz, L. Sulmoni and N. Grandjean, *Bias-dependent Absorption Coefficient of the Absorber Section in GaN-based Multi-Section*, International Workshop on Nitride semiconductors IWN 2010 (Tampa, Florida, September 19-24, 2010), 1 page.

5. L. Sulmoni, J. Dorsaz, A. Castiglia, J.-F. Carlin and N. Grandjean, *Effect of saturable absorber bias voltage on the output characteristics of multi-section GaN-based laser diodes*, International Workshop on Nitride semiconductors IWN 2010 (Tampa, Florida, September 19-24, 2010), 1 page.

6. I. V. Smetanin, P.P. Vasil'ev, D.L. Boiko, *Theory of Mode-Locked InGaN/GaN Lasers in Large Signal Regime*, International Workshop on Nitride semiconductors IWN 2010 (Tampa, Florida, September 19-24, 2010), 1 page.

7. D. L. Boiko and P.P. Vasil'ev, *Dicke Superradiance in a Multi-Section GaN Edge Emitting Cavity*, International Workshop on Nitride semiconductors IWN 2010 (Tampa, Florida, September 19-24, 2010), 1 page.

8. J. R. van Look, V. Hoffmann, S. Einfeldt, M. Weyers, P. Vogt and M. Kneissl, *Improved Transverse Mode Confinement for 450 nm InGaN MQW Lasers*, submitted to European Materials Research Society E-RMS 2010 fall meeting (Warsaw, September 13-17, 2010), 1 page.

9. W. G. Scheibenzuber, C. Hornuss, and U. T. Schwarz, *Dynamics of GaN-based laser diodes from violet to green*, Photonics West OPTO 2011 (San Francisco, California, January 21-26, 2011), 7 pages

10. Vojtech Olle, Peter Vasil'ev, Adrian Wonfor, Richard Penty, and Ian White, *High Power Short Pulse Generation at High Repetition Rate from InGaN Violet Laser Diodes*, CLEO 2011 (Baltimore, Maryland, May 1-6, 2011) JWA82, 2 pages.

11. L. Sulmoni, J. Dorsaz, J.-F. Carlin, and N. Grandjean, *Optical characteristics of multi-section GaN-based laser diodes*, 38th International Symposium on Compound Semiconductors - ISCS 2011 (Berlin, Germany, May 22-26, 2011), 2 pages.

12. J. Dorsaz, D. Boiko, L. Sulmoni, J.-F. Carlin, and N. Grandjean, *Optical bistability in multi-section InGaN-based laser diodes*, 9th International

Conference on Nitride Semiconductors - ICNS 2011 (Glasgow, Scotland, July 10-15, 2011), 1 pages.

13. L. Sulmoni, J. Dorsaz, J.-F. Carlin, and N. Grandjean, *Reverse bias voltage dependent optical characteristics of multi-section GaN-based laser diodes*, 9th International Conference on Nitride Semiconductors - ICNS 2011 (Glasgow, Scotland, July 10-15, 2011), 1 pages.

14. W. Scheibenzuber, U. Schwarz, L. Sulmoni, J. Dorsaz, J.-F. Carlin, and N. Grandjean, *Auger recombination in GaN-based laser diodes*, 9th International Conference on Nitride Semiconductors - ICNS 2011 (Glasgow, Scotland, July 10-15, 2011), 1 pages.

15. D. L. Boiko and P. P. Vasil'ev, *Theory of femtosecond superradiance in InGaN/GaN quantum well laser structures*, 9th International Conference on Nitride Semiconductors - ICNS 2011 (Glasgow, Scotland, July 10-15, 2011), 1 pages.

16. I. V. Smetanin, P. P. Vasil'ev, and D. L. Boiko, *Theory of the Ultrafast Mode-Locked InGaN/GaN Lasers in a Large-Signal Regime*, 9th International Conference on Nitride Semiconductors - ICNS 2011 (Glasgow, Scotland, July 10-15, 2011), 1 pages.

17. L. Sulmoni, J. Dorsaz, D. L. Boïko, J.-F. Carlin, and N. Grandjean, *Optical characteristics of multi-section InGaN-based laser diodes*, European Semiconductor Laser Workshop - ESLW 2011 (Lausanne, Switzerland, September 23-24, 2011), 1 page.

18. L. Sulmoni, D. L. Boïko, J. Dorsaz, J.-F. Carlin, W. G. Scheibenzuber, U. T. Schwarz and N. Grandjean, *Optical bistability in InGaN-based multi-section laser diodes: Theory and experiment*, European Semiconductor Laser Workshop - ESLW 2011 (Lausanne, Switzerland, September 23-24, 2011), 1 page.

19. D. L. Boiko, *Type-I and type-II superradiance in edge emitting laser cavities*, European Semiconductor Laser Workshop - ESLW 2011 (Lausanne, Switzerland, September 23-24, 2011), 1 page.

20. L. Sulmoni, J. Dorsaz, A. Castiglia, J.-F. Carlin, and N. Grandjean, *Impact of the reverse bias voltage on the optical characteristics of multi-section GaN-based laser diodes*, IV Workshop on Physics and Technology of Semiconductor Lasers (Kazimierz Dolny, Poland, October 23-26, 2011), 1 page.

THESES

1. W. G. Scheibenzuber, *GaN-based laser diodes: towards longer wavelengths and short pulses*, ISBN 978-3-642-24537-4, Hardcover, publication scheduled for February 16, 2012.

http://femtoblue.epfl.ch

Inline with that, sections concerning project highlights and related events are regularly updated.

As a result of dissemination activities at the conferences FEMTOBLUE has been contacted by the group of Prof. Hiroyuki Yokoyama from TOHOKU University leading the project with SONY on development of 405 nm picosecond semiconductor laser for application in a future 3D optical data storage disk system. Contacts to other projects focused on GaN devices (UNITRIDE), ultrafast lasers (FASTDOT) or SPAD detectors for TCSPC fluorescence lifetime imaging (MEGAFRAME) have been established.

Numerous contacts from the side of Industry reveal large interest to the project. However to be able to proceed with valorisation of the results of the project, the first step of which is the exploitation plan, the Consortium has to demonstrate more solid results confirming the expected performances in the Third period of the project.

8. Conclusion

Our evaluation of the project is that it has reached most of the objectives of the second period:

In the second phase of the project we have fabricated and tested preliminary samples of multi-section InGaN/GaN multiple quantum well laser structures following three approaches for ultrafast pulse production: superradiance, active and passive modelocking. In parallel, deep experimental and theoretical studies have been made on optimizing the quantum well heterostructure composition and cavity configuration with the objective to arrive to the final design by the beginning of the third phase of the project. This objective is reached, thanks to strong interaction between all activities in the project.

The consortium has continued with development of models which are designed to predict the performance of short pulse production in the 3 key areas of operation – active and passive mode-locking. The models are developed in order to optimise the design of the laser, using techniques appropriate to each regime of operation, with active mode-locking being investigated with a travelling wave based numerical model, passive mode-locking using a solution to Haus' master equation and superradiance with both numerical and analytical techniques. Both active and passive mode-locking simulations predict the need for a laser with a rather large absorber, of at least 20% of the total cavity length. Both passive, and in particular active mode-locking simulations highlight the benefits to be gained from a short carrier lifetime within the absorber section for stable, short pulses to be produced. In lasers exhibiting Dicke superradiance gain compression has been shown to be a key factor affecting pulse performance, and new cavity designs have been produced which mitigate this effect. In all short pulse regimes sub-picosecond pulses are predicted.

Numerical spatio-temporal model for superradiance regime established in the first period of the project is based on numerical solver of semi-classical Maxwell-Bloch equations. It requires substantial amount of computer time to accomplish the cavity optimization task. The triggering of superradiance is a stochastic process, for which the numerical model incorporates the Langevin noise terms. As such, predicted pulse parameters show large variations between individual realisations. In order to overcome these difficulties, a pure analytical model has been developed for spontaneous build-up of superradiance in semiconductors. It is based on the second-order phase transition equation of the form similar to the Ginzburg Landau equation for a phase transition into a super-conducting state, thus providing another reasoning for a picture of formation of a transient coupled electron-hole pair state intermediated by photons, much like the phonons in a BCS state. This master equation has been derived from semiclassical Maxwell-Bloch equations. Its analytical solution has enabled rapid evaluation of the superradiance pulse parameters. Two types of superradiance regimes have been predicted.

InGaN quantum well growth optimization aimed at reducing the photoluminescence linewidth to avoid gain dilution has been carried out during this second phase. Full-width at half-maximum below 40 meV has been obtained at low temperature and 80 meV at 300K. In parallel, we received a new MOVPE reactor in November 2010 and started its installation next December. The main recipes were developed during the Spring 2011 and eventually FEMTOBLUE laser diodes emitting from 400nm to 440nm with excellent performance were fabricated. These devices are working under cw operation with low lasing threshold current (<50 mA). In addition, we also implemented a new mask with longer absorption sections. Finally, laser epiwafers were grown with various well thicknesses but still keeping the same wavelength emission to look for the relevant parameters that control the differential gain.

InGaN multiple quantum well (MQW) laser diode heterostructures for emission in the spectral range from 425 nm to 450 nm have been optimized. The studies include the optimization of the thickness and the indium mole fractions of the InGaN quantum wells and InGaN barriers of the active region. Based on modal gain simulations an optimum quantum well width was found for emission at around 440 nm. Furthermore, the thickness and aluminium

content of the AlGaN cladding layers and AlGaN electron blocking layer was optimized for laser diode structures emitting in the blue wavelength range. Especially p-GaN and p-AlGaN overgrowth was adopted to lower growth temperatures as required by the high In containing quantum wells. Finally an injection laser structure was grown on bulk GaN substrate using the optimized device design and growth parameters.

Macroscopic photoluminescence measurements on violet–and blue-wavelength laser heterostructure wafers of the second generation were measured to provide feedback on the homogeneity of the epitaxial growth. A good uniformity across the measured half wafers was found, with a significantly increase number of sample points, when compared to scans of the wafers from the first period. The new wafer showed strongest PL emission for longer wavelengths.

Ultrafast laser operation at high peak power of output pulses assumes high pumping currents in the active region. In distinguishing from conventional III-V devices, a laser implemented in group-III nitride alloys is characterised by a high voltage drop across the structure. We have developed a mounting approach, which enables efficient thermal heat sinking and compatible with the high frequency operation requirements. Mounted multisection laser diodes with additional intracavity losses introduced by the absorber have shown stable lasing under the CW pumping conditions. Following this approach we have fabricated a set of samples of multisection laser diodes for dynamical tests in superradiance, active and passive modelocking regime.

In parallel, we go further in our processing technology and established an advance processing technique which is compatible with the unusual requirements to the final design of the cavity of ultrafast group III- nitride lasers.

Single and multi-section laser diodes from EPFL and TUBerlin were characterized by Hakki-Paoli gain spectroscopy under continuous pumping. Internal losses, injection efficiency and differential gain were measured for a large set of laser diodes. For multi-section laser diodes the absorption in the absorber section was determined as function of reverse bias. Using time-resolved electroluminescence, we measured carrier lifetime in the absorber section at reverse bias, which is an important quantity for short pulse operation. We also determined differential gain as function of carrier density and gain saturations, both through a in-depth evaluation of laser dynamics, in particular of relaxation oscillations.

The test setup was built for the evaluation of the lasers operating in three different dynamic regimes. It allows for the comprehensive measurements of main dynamic and static parameters of lasers. Both superradiant pulses and active/passive mode locked pulses can be detected. Experimental tests of the first set of mounted multi-section laser have been performed. Bistability, gain switching, and self Q-switching regimes have been obtained. Picosecond pulses as short as 3-5 ps at the repetition rates close to the cavity round trip time have been observed in some 2-section lasers under passive mode locking driving conditions. In one sample, features resembling superradiant emission have been detected.

Dissemination and migration of the project results into the scientific community and industry is well underway.